CENTRE SUISSE D'ELECTRONIQUE ET DE MICROTECHNIQUE S.A.
- Recherche et Développement -

UNIVERSITE DE NEUCHATEL
Institut de Microtechnique

Determination of Intermodal Dispersion in Integrated Optic Waveguides from Near-Field Intensity Measurements

Thèse
Présentée à la Faculté des Sciences
pour obtenir le grade de docteur ès sciences

par

Patrick Roth

Neuchâtel, mai 1994

IMPRIMATUR POUR LA THÈSE

Determination of the intermodal dispersion in integrated optic waveguides from nearfield intensity measurements

de Monsieur Patrick Roth

UNIVERSITÉ DE NEUCHÂTEL

FACULTÉ DES SCIENCES

La Faculté des sciences de l'Université de Neuchâtel
sur le rapport des membres du jury,

Messieurs R. Dändliker, J.-P. Amiet,
O. Parriaux, R. Ulrich (Hambourg) et
M. Papuchon (LCR Thomson, Orsay)

autorise l'impression de la présente thèse.

Neuchâtel, le 22 juin 1994

Le doyen:

H.-H. Nägeli

A Mélanie, à mes parents

Acknowledgements

I am very much indebted to Prof. Dr R. Dändliker, Institute of Microtechnology, University of Neuchâtel, who acted as Thesis Director of this work, and to Dr. O. Parriaux, Senior Scientist at CSEM S.A., who supervised this investigation. Their constant help and advice have made a key contribution to the success of this work.

I would like to address my special thanks to Prof. R. Ulrich, Technical University of Hamburg-Harburg, for his invaluable comments made on this report. Likewise, I would like to thank Prof. Amiet, Physics Institute, University of Neuchâtel, for his interest showed at various stages of this investigation.

My special thanks are also due to Dr. M. Papuchon, Optoelectronics Department of L.C.R. Thompson, Orsay, who has privileged me by accepting to be an examiner of this thesis.

To all my colleagues at CSEM S.A., who provided me with a singularly friendly and stimulating atmosphere throughout the course of this work, I extend my deepest appreciation. In particular, I would like to thank G. Voirin for helpful discussions concerning Integrated Optics, B. Scheja who prepared, with the greatest care, all samples used in this work, and L. Falco who expertly built the set-up used for the near-field intensity measurements.

Last but not least, I would like to express my very special thanks to Ms M. Pralong, for her enduring patience, constant support, and invaluable help in proof reading this manuscript. I also thank A. Yi-Yan, for his expert comments concerning the general organization of this thesis.

This thesis work was carried out at the Laboratory of Optics of the Swiss Center for Electronics and Microtechnology, CSEM S.A. I thank the Board of Directors for their financial support, and for permission to publish this work.

Summary

This work proposes a technique based on an Output Near-field Intensity Distribution Analysis (ONIDA) method, to determine the intermodal dispersion of lightly multimode optical waveguide structures. This technique has been tested on ion-exchanged waveguides supporting one mode in depth and a few number of modes in the lateral dimension.

The principle of the ONIDA technique is rather simple. The near-field output intensity distribution of a multimode waveguide results from interference between guided modes, and can be experimentally measured. This interference pattern is a function of the modal eigenfields and of the output mode coefficients. The latter depend on the excitation mode coefficients and on the cumulative phase of each mode due to propagation along the waveguide. The intermodal dispersion, i.e. the effective index differences between the guided modes, can be determined from a knowledge of these sets of parameters.

In this work, the first set of parameters is calculated from known excitation conditions, using a focused Gaussian beam to input light into the waveguide. The output mode coefficients are obtained from a comparison between the theoretical and measured near-field intensity distributions, using an algorithm which minimizes a sum of squared errors. For the sake of simplicity, the eigenfield computation is carried out using the scalar wave equation, the method of effective indices, and a step-index profile model in the lateral dimension. From the excitation and output mode coefficients, the cumulative phase of each mode is deduced, and the effective index differences between modes evaluated.

In this first investigation of the ONIDA method, we first evaluated the viability and effectiveness of this approach, using simulated output intensity distributions of some typical planar waveguiding structures. By the same way, the accuracy provided by this new technique has been estimated.

The experimental demonstration of the ONIDA technique has been carried out using three different types of waveguide structures, all being fabricated by ion-exchange in glass. The ONIDA method successfully predicted the modal dispersion in the first type of structure: a three-branch directional coupler, made up of three parallel single-mode waveguides with similar

widths. The results obtained for the second type of structure, a four-branch directional coupler consisting of four single-mode waveguides, were less accurate. The discrepancies found are attributed to the fact that the theoretical eigenfields were calculated using a step-index, rather than a graded-index profile, which closely resembles the actual index distribution of the ion exchanged waveguides used in these experiments. The results for the third type of structure, made up of a single wide section, four-mode waveguide, was not thoroughly conclusive. Difficulty in achieving good enough accuracy of the excitation conditions precluded a more comprehensive analysis of this type of structure.

The above results suggest that the ONIDA technique can be usefully applied to lightly multimode waveguide structures having a step index profile. Its implementation to waveguides with a larger number of modes could be achieved by exciting the guided modes through a single-mode waveguide attached to the multimode section. This will substantially reduce the difficulties related to the accuracy required in exciting the modes, directly into the multimode waveguide section. The implementation of the ONIDA technique can be generalized to waveguides with graded index profile, provided that the eigenfields are calculated with high enough precision. This can be readily achieved by using a multi-layer program, where the number of step-index sections approximating the actual profile can be varied to attain the required accuracy.

Résumé

Ce travail presente une méthode de mesure de la dispersion intermodal de structures en guide d'onde optique par l'analyse en champ proche de la distribution d'intensité en sortie de guide (méthode ONIDA: Output Near-field Intensity Distribution Analysis). Cette méthode est testée au moyen de guides optiques réalisés par échange ionique, et supportant un mode en profondeur et quelques modes latéralement.

Le principe de cette méthode est le suivant: la distribution d'intensité à la sortie d'un guide multimode résulte de l'interférence des modes guidés, et peut être mesurée expérimentalement. Elle dépend des champs propres et des coefficients modaux en sortie de guide, ces demiers étant donnés par les coefficients modaux d'excitation et par les phases optiques accumulées par chacun des modes lors de la propagation. La dispersion intermodale, c'est-à-dire les différences d'indices effectifs entre modes guidés, est déterminée à partir de ces paramètres.

Dans ce travail, les coefficients modaux d'excitation sont calculés à partir de conditions d'injection connues, données par un faisceau gaussien focalisé à l'entrée du guide. Les coefficients modaux en sortie de guide sont obtenus par comparaison entre les distributions d'intensité théorique et expérimentale, un algorithm d'optimisation donnant les coefficients minimisant une somme de carrés d'erreurs. Dans un but de simplification, l'équation d'onde scalaire est admise dans ce travail, et les champs propres sont obtenus par la méthode des indices effectifs et par une approximation du profil d'indice latéral par un saut d'indice. Avec les coefficients modaux d'excitation et en sortie de guide, on calcule les différences de phases accumulées entre modes lors de la propagation, puis les différences d'indice effectif entre modes guidés sont évaluées.

Dans cette première étude de la méthode ONIDA, la validité du principe utilisé est tout d'abord évaluée en introduisant dans l'algorithme des distributions d'intensité simulées, ceci pour quelques structures de guide d'onde planaires. Par ce moyen, la précision atteinte par cette méthode est également estimée.

La démonstration expérimentale de cette méthode d'analyse de la distribution d'intensité est faite grâce à trois types de structures, toutes

réalisées par échange ionique dans du verre. La méthode ONIDA prédit avec succès la dispersion intermodale d'un coupleur directionnel, composé de trois guides monomodes de largeur similaire. Dans le cas d'un coupleur directionnel à quatre guides monomodes, les résultats ne sont pas aussi positifs: ceci provient de l'hypothèse du profil latéral à saut d'indice, hypothèse à laquelle ce type de structure ne correspond pas avec suffisamment de précision. Enfin, le cas d'un guide unique supportant quatre modes montre que les conditions d'excitation ne sont pas suffisamment contrôlées pour mesurer ce type de structure.

Les résultats obtenus par la méthode ONIDA laisse penser que cette technique peut être appliquée avec succès à des guides à saut d'indice faiblement multimodes. Sa généralisation à des guides plus larges sera obtenue en excitant les modes guidés de la section large grâce à un guide monomode, arrivant à l'entrée du guide faiblement multimode. Ainsi, l'influence de l'alignement du faisceau d'entrée sera réduite. L'utilisation de la méthode ONIDA pourra être généralisée à des guides à gradient d'indice, dès lors que les champs propres seront calculés avec une précision suffisante. Ceci pourra être réalisé en utilisant une approximation du gradient d'indice par un profil à multi-couche.

Contents

Notation

Convention

Unless otherwise stated, the following notation is adopted for the mathematical expressions used throughout this thesis. Scalar numbers are written in lower case letters, complex numbers in capitals. An asterisk (*) denotes the complex conjugate of a complex number, i.e. A^*. Vectors and matrices are described by bold-faced letters. Vectors are column vectors.

The complex conjugate of a vector or a matrix is also depicted by an asterisk. Hence:

$$\mathbf{A}^* = \begin{pmatrix} A_0^* \\ A_1^* \\ \vdots \\ A_n^* \end{pmatrix} \qquad \mathbf{M}^* = \begin{pmatrix} M_{00}^* & M_{01}^* & \cdots & M_{0n}^* \\ M_{10}^* & M_{11}^* & & M_{1n}^* \\ \vdots & & \ddots & \vdots \\ M_{n0}^* & M_{n1}^* & \cdots & M_{nn}^* \end{pmatrix}$$

The transposed of a vector or a matrix is denoted by the superscript $\mathbf{M}^T$:

$$\mathbf{A}^T = \begin{pmatrix} A_0 & A_1 & \cdots & A_n \end{pmatrix}$$

The conjugate transpose of a vector or of a matrix is written as:

$$\mathbf{A}^\dagger = \mathbf{A}^{*T}$$

List of Symbols

Symbol	Description	Units
$\mathbf{E}$	electric field	V/m
$\mathbf{H}$	magnetic field	A/m
$\boldsymbol{E}$	modal electric field	V/m
$\boldsymbol{H}$	modal magnetic field	A/m
$\boldsymbol{E}_t$	transverse component of the modal electric field	V/m
$\boldsymbol{E}_z$	longitudinal component of the modal electric field	V/m
$\boldsymbol{H}_t$	transverse component of the modal magnetic field	A/m
$\boldsymbol{H}_z$	longitudinal component of the modal magnetic field	A/m
$\mathscr{E}_i$	electric eigenvector of order i	V/m
$\mathscr{H}_i$	magnetic eigenvector of order i	A/m
$\mathbf{S}$	Poynting vector	W/m^2
P	Optical power	W
ε	dielectric constant	As/Vm
ε_0	free-space dielectric constant	As/Vm
n_m	refractive index of medium m	
μ_0	free-space permeability	Vs/Am
ω	angular frequency	s^{-1}
k_0	propagation constant in free-space	m^{-1}
β_i	propagation constant of mode i	m^{-1}
n_i	effective index of mode i	
δ_{mi}	modal parameter of mode i in medium m	m^{-1}
N	highest mode order of a waveguiding structure	

CHAPTER I

INTRODUCTION

The earliest experiments involving the guiding of light along dielectric layers date from the beginning of the sixties [1]. At that time, the projected application was the interconnection of integrated-electronics devices, replacing the electrical circuitry. In 1969, S.E. Miller introduced the term of "Integrated Optics" for this new technology [2]. A few years later, the considerable development of optical fibre telecommunications became the major development factor for integrated optics. Since then, several new applications and technologies arose. A review of research in integrated optics on dielectric materials is given in [3]. We give now a short overview of the main technologies involved in integrated optics and some of their numerous applications, in order to give an idea of the present and future impact of this new technology.

The earliest experiments were carried out on glass substrates [1, 4]. Although this material gives rise to low propagation loss, it only allows the realization of passive components. Therefore, lithium niobate ($LiNbO_3$) quickly attracted much attention, thanks to its electrooptic properties: the demonstration of integrated optical modulators opened a wide field of research [5]. However, light sources and detectors cannot be achieved on this type of substrate. So, III-V and II-VI semiconductors were investigated as materials for integrated optics [6]: they allow the integration of light sources, waveguides, modulators, and detectors on the same substrate [7]. Quite early, the light confinement obtained in integrated optical waveguides was thought to be of great interest for the achievement of non linear optical devices. Therefore, materials with high non linear coefficients, including polymers, appeared among other suitable technologies in integrated optics [8].

The first forseen applications of integrated optics arose in telecommunication: passive components for light distribution [9], high speed modulators [10], light sources [11]. This domain still generates new

developments nowadays, e.g. in highly integrated devices [12]. However, other applications have appeared, for instance in data processing: integrated optical spectrum analysers [13], analog-to-digital converters [14] or compact disk (CD) reading head [15] have been demonstrated. Integrated optics have also been applied to sensor applications, with, among others, optical gyroscopes [16] or interferometers for displacement measurements [17].

In this bubbling domain of integrated optics, the need of characterization methods grows with the increasing number of technologies and applications: propagation loss measurement [18] or refractive index profiling [19] are some of them. The present work meets this general demand of analysing methods, with the characterization of modal propagation in integrated optic waveguides.

I.1. MOTIVATION OF THE PRESENT WORK

In 1975, R. Ulrich presented the first demonstration of manifold imaging in optical waveguiding structures [20]. This effect results from a specific phase relation between the eigenmodes of a multimode planar optical waveguide. Thus, an inverted image of the input light distribution is formed after a characteristic propagation length L_c, as depicted in Fig. 1.1, while n subimages appear at integer multiples of L_c/n.

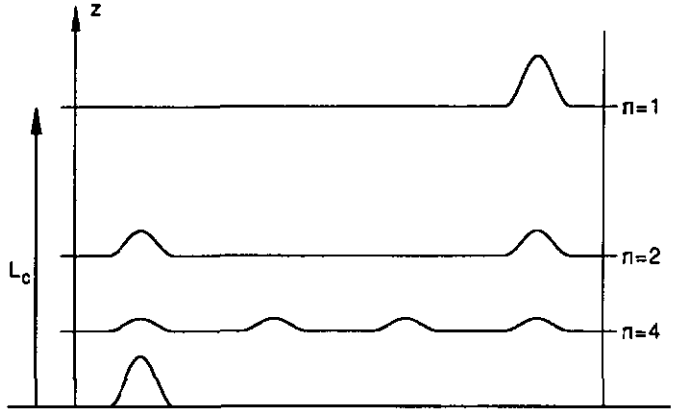

Fig. 1.1 Manifold image formation in a multimode interference (MMI) waveguide section, with n=1, 2 and 4.

A few years later, a device providing four quadrature outputs in an interferometer was demonstrated [21]. It used the fourfold image formation in a flat core fibre and made the interference of the reference and signal beams in a two-beam interferometer (see Fig. I.2).

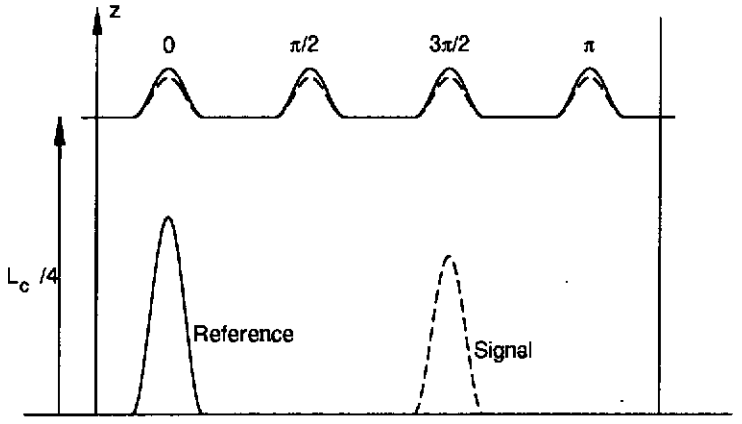

Fig. I.2 Principle of the phase demodulator providing quadrature intensity output signals

We implemented this interesting component in an ion-exchanged multimode interference (MMI) section in order to use it as a phase demodulator of an integrated optic interferometer [22]. In this device, when the optical phase of the signal beam is modulated with respect to the reference beam, the subimages of the signal beam interfere with the corresponding subimages of the reference. Theoretically, the interference signals of subimages 2, 3 and 4, i.e. their optical output powers, show a phase shift of $\pi/2$, $3\pi/2$ and π, with respect to the power signal of subimage 1. However, the phase shifts observed experimentally using an ion-exchanged single-section waveguide were π, $\pi/2$ and $3\pi/2$ for subimage 2, 3, and 4, respectively [21]. This discrepancy cannot be simply explained by the reversal of the optical phase of the signal beam.

Therefore, our initial motivation in the present work was to understand the unexpected behaviour observed in our experiments. To this aim, the propagation constant differences between guided modes are the relevant parameters to be analysed. Since the propagation constants, or equivalently the mode effective indices, are closely related to the transit time of a guided

mode through a propagating structure, studying the effective index differences is the same as measuring the intermodal dispersion of optical waveguides. So, we first examined some existing methods for measuring effective index differences in optical waveguides, and evaluated their possible application to integrated optic waveguide characterization. This analysis is summarized in Section I.2. It concludes that some of the examined methods are not adapted to our particular case, while two techniques are possible candidates.

During this preliminary study, it appeared that analysing the near-field intensity distribution measured at the waveguide output had the potential to provide the effective index differences between guided modes. So, we chose to investigate in this new method. Its principle is presented in Section I.3. The objectives of this work are pointed out in Section I.4.

I.2. COMPARISON OF THIS WORK WITH EXISTING TECHNIQUES

With the ion-exchange technology used at CSEM, the maximum index difference between waveguide core and substrate is about 10^{-2}. Therefore, we will consider effective indices lying in this range. Furthermore, the needed resolution for the measurement of effective index differences is approximately 10^{-5}, in order to properly characterize optical waveguides using the subimaging effect. The comparison of the methods presented below assumes these values.

Beat length measurement

The simplest method for measuring the effective index differences between two modes of a multimode waveguide section is to measure the beat length: in a two-branch directional coupler for instance, the light coupled into one guide of the coupler is transferred to the other branch and comes back after a propagation length called the beat length. With the desired resolution of the effective index difference between two modes, i.e. 10^{-5}, the beat length is approximately 100 mm. By using Fourier Transform analysis, the waveguide length requested for measuring the beat length could be reduced. A quarter of the beat length, namely approximately 25 mm, seems to be a minimum. Furthermore, measuring by a similar approach three- or four-branch couplers involves several beat frequencies, due to the interference of each guided mode with all the other ones. For more than three guided

modes, attributing the various beat lengths to each index difference quickly becomes difficult. The last characteristic of the beat length measurement is that the light scattered by local index inhomogeneities of the waveguide core has to be observed. The scattering efficiency may be not uniform all along the waveguide length, leading to unexpected beat length observations. In conclusion, the beat length measurement appears to be hardly applicable to the characterization of few mode waveguides.

Prism or grating coupling

It is well known that the effective indices can be measured by prism coupling or decoupling [23]. Considering the decoupling case, each guided mode comes out of the prism with a different angle. For example, an effective index difference of 10^{-5} between two guided modes leads to an out-coupling angle difference of typically $2 \cdot 10^{-5}$ radians. Each modal beam propagating in free space diverges, due to diffraction. In order to separate the different modal beams at the observation point, their divergence angle must not exceed the output angle difference. This condition can be achieved in ion-exchanged waveguides when the out-coupled beam size is larger than 20 mm. This is not practical to obtain experimentally.

Similarly to the prism, a grating decouples guided modes at specific output angles [24]. By choosing for instance a grating pitch equal to twice the free-space wavelength, a decoupling grating typically leads to a $8 \cdot 10^{-5}$ radians angle difference between two out-coupled modes showing an effective index difference of 10^{-5}. In this case, the divergence condition of the out-coupled beam leads to a minimum beam width of about 10 mm. Therefore, the grating efficiency must be weak enough for giving rise to a 10 mm wide beam, which is possible to obtain. A necessary condition is now to fabricate a grating with a very uniform pitch: a 10^{-5} µm uniformity over the 10 mm grating length is typically required. Holographic gratings can reach such a precision.

To conclude, coupling or decoupling guided modes with a grating provides a possible solution for measuring effective index differences as low as 10^{-5}. However, this method is limited to waveguiding structures for which the evanescent part of the eigenfield is accessible. Therefore, buried waveguides or few mode fibres for example could not be characterized. For this reason, we did not further consider the grating decoupling method.

Fabry-Perot resonator

In a Fabry-Perot resonator, a beam is transmitted when it satisfies a resonance condition, given, among others, by the refractive index of the cavity. Therefore, eigenmodes with distinct effective indices do not meet simultaneously this resonance condition. As a result, they can be selectively transmitted through the Fabry-Perot cavity. However, a proper operation of the Fabry-Perot filter implies a few conditions: we calculated that a cavity length of about 0.5 mm is requested, together with a finesse of about 100. Such a finesse was obtained in an approximately 10 cm long fibre [25], in which the propagation loss is of the order of $5 \cdot 10^{-4}$ dB. The situation of integrated optic waveguides is not so favorable: the propagation loss, even in a 0.5 mm long waveguide, is about $2 \cdot 10^{-3}$ dB. As a result, a finesse of 100 cannot be achieved in integrated optic waveguides made by ion-exchange. Therefore, this principle is not convenient for measuring effective index differences in ion-exchanged structures.

Beat frequency methods

Beat frequency methods use for instance the different propagation times of the guided modes: a mode excited at a time t_i arrives at the waveguide output at a time t_o, with $t_o > t_i$. A slower mode, reaching the waveguide end at the same time t_o, was excited at the time $t_i - \Delta t$. Now, if the excitation light frequency is different at t_i than it was at $t_i - \Delta t$, say the frequency difference is Δf, then both modes interfere in the output plane with a beat frequency Δf. This effect can be achieved by modulating the light source frequency, for example with a saw-tooth shape, and the beat signals can be observed with a spectrum analyser. In the case of a saw-tooth optical frequency modulation, and with a spectrum analyser resolution of about 30 Hz, an optical frequency change of 120 GHz must be achieved in 0.4 ms. This can be obtained with semiconductor laser, by modulating the driving current by 10 mA at a frequency of 2.5 MHz.

The main difficulty of such methods is that the number of beat frequencies increases with the squared number of guided modes. Indeed, each mode interferes with all other guided modes. Therefore, a waveguide propagating M modes generates M(M-1)/2 beat frequencies. Each of them must be then related with the effective index difference between two modes. This is a difficult task if the mode number becomes

greater than 3. This was shown recently in a paper of R. Eckhardt and R. Ulrich [26]. In the proposed method, the modes are coupled to each other at a given coordinate of the propagation axis. The beat signal is observed as a function of the position of the coupling effect, namely the Faraday effect. In this experiment, carried out with a 3 m long fibre, several spatial beat frequencies have appeared, as it is the case with saw-tooth frequency modulation. Therefore, a careful interpretation of the results is required. Nevertheless, the authors expect that this method can be applied successfully to integrated optic waveguides.

Conclusion

Several methods for measuring the effective index difference between guided modes have been examined. Some of them are hardly applicable, because the associated experimental conditions cannot be achieved or are unpractical for our particular waveguide structures. This is the case of the beat length measurement, of the prism coupling or decoupling, and of the Fabry-Perot resonator. However, we identified two methods which could lead to the intermodal dispersion measurement in integrated optic waveguides. On the one hand, the grating coupling or decoupling is a potential candidate. However, this method cannot analyse embedded waveguides, because the grating is far from the waveguide core in this particular case. As a result, the guided wave is not diffracted by the corrugation. On the other hand, a beat frequency method, involving the saw-tooth optical frequency modulation of a semiconductor laser beam, also provides the possibility to measure intermodal dispersion in integrated optic waveguides. In this method, a difficulty arises with the numerous beat frequencies appearing when the guided mode number is greater than two. Each beat signal has to be attributed to a pair of modes, requiring a great deal of interpretation.

The method we propose in this work, based on the analysis of the output near-field intensity distribution of a waveguide structure, has not been investigated yet. It can be potentially applied to embedded waveguides and to waveguiding structures carrying a few modes. The principle of this method is described in the following section.

I.3. PRINCIPLE OF THE PROPOSED METHOD

Propagation in an optical waveguide can be described in the following way. A light distribution, located at the waveguide input, excites the guided modes, leading to a complex excitation coefficient for each guided mode. Then, propagation in the waveguide adds an optical phase to each mode coefficient, according to the mode effective index, the propagation length and the wavelength. Furthermore, the propagation loss attenuates the mode amplitudes, i.e. it decreases the mode coefficient moduli. The output field results from the interference of the eigenmodes. Mathematically, it is given by the linear combination of the eigenfields, weighted by their corresponding complex mode coefficients. Finally, the intensity distribution, which can be experimentally measured at the waveguide output, is given by the square of the output field amplitude.

Measuring the output intensity distribution can be performed by a simple set-up: no special light sources are required: even a multimode laser, such as a HeNe or semiconductor laser, is convenient. In addition, scanning the output intensity distribution can be carried out with a 0.1 μm resolution, by using micropositioning devices. Furthermore, in spite of the intensity distribution sampling, optical power levels of a few microwatts reach the detector and are measured without difficulty by a conventional lock-in amplifier. Finally, the waveguide samples do not require special preparation: the input and output end-faces are polished like for any other application. For these reasons, it would be very convenient to measure the output intensity distribution, and, from this measurement, to calculate the effective index differences, i.e. the intermodal dispersion.

Since the output intensity distribution contains all the information regarding propagation in the waveguide struture, it is certainly possible to deduce the optical inter-mode phase differences accumulated by propagation. To this aim, we first have to calculate the waveguide eigenfields from the supposedly known refractive index profile and the excitation mode coefficients from supposedly known input light conditions. Next we determine the complex mode coefficients from the measured output intensity distribution; for this purpose, we will propose a dedicated algorithm. Then, the optical phases due to propagation in the waveguide are calculated, taking the excitation mode coefficients into account. From this, the effective index differences between eigenmodes can be deduced.

1.4. OBJECTIVES OF THIS THESIS

The main purpose of the present work is to demonstrate the possibility to calculate the effective index differences between eigenmodes from the measured output intensity distribution. To this aim, we will proceed in two steps. First, we will show the validity of our approach by using some simulated intensity distributions of three planar waveguide structures: a three-branch coupler and a four-branch, both made up of single-mode parallel waveguides, and a four-mode single section waveguide. These simulated intensity distributions will also allow an estimation of the accuracies required from the computed eigenfields and other experimental conditions. Next, we will test the proposed method for characterizing the intermodal dispersion of the three types of waveguide structures. For this purpose, we will also choose a three- and a four-branch coupler, and a single section waveguide, all made by ion-exchange in glass. Therefore, the effective index range to be measured is typically 10^{-2}. Regarding the resolution, we expect the proposed method to reach 10^{-5}, which is typically necessary for designing integrated optic devices making use of the self-imaging effect in waveguides.

In this first investigation of the Output Near-field Intensity Distribution Analysis (ONIDA), we will as far as possible keep simple mathematical models, in particular for the propagation in integrated optic waveguides. Therefore, we will use the scalar wave equation and the Effective Index Method for calculating the eigenfields [33]. We will also discard the propagation loss of integrated optic waveguides, which leads to complex propagation constants; we thus only considered purely real effective indices.

From this study of the ONIDA method, we expect to (i) determine the effectiveness of the proposed method; (ii) point out the difficulties raised by this technique; (iii) determine most appropriate experimental conditions for a proper operation of this method. In short, we want to evaluate the potential of the ONIDA method for measuring the intermodal dispersion in few mode waveguide structures.

Organization of this thesis

In Chapter II, we define the symbols involved in this work and present the assumptions leading to the eigenfield calculation. Then, Chapter III briefly describes the technique used for fabricating waveguide samples: the ion-exchange technology in glass. We also point out the main properties of these waveguides. In Chapter IV, we choose injection conditions leading to known mode coefficients at the waveguide intput. Next, a method for calculating the mode coefficients from the output intensity distribution is presented. Chapter V shows the effectiveness of the proposed method from simulated output intensity distributions, as well a some difficulties raised by this method. Then, three actual waveguiding structures are analysed experimentaly. The limitations and difficulties are discussed. Finally, we conclude in Chapter VI by a few suggestions for a more efficient use of the proposed method.

CHAPTER II

WAVEGUIDE MODELLING

In this chapter, the mathematical model assumed for the eigenfield calculation is presented. We chose to assume the scalar wave equation, although an accurate description of the self-imaging effect in ion-exchanged multimode waveguides should take the full vector wave equation into account. This choice is dictated by one of our goal: using simple mathematical desciption of waveguide propagation. Nevertheless, the approximations used for the eigenfield calculation are relevant with our eyxperimental conditions and can be justified in relation with the integrated optic waveguides used in the experiments.

The mathematical description used in this work is based on the theory given by Kogelnik [28]. Therefore, the mathematical developments are not detailed: the reader is referred to this reference. However, the approximations leading to the scalar wave equation are justified in more details. Then, the general expression of propagating fields is given, from which we deduce the intensity distribution. Lastly, the model assumed for the calculation of eigenfields in integrated optic waveguides is presented.

II.1. THE SCALAR WAVE EQUATION AND ITS SOLUTIONS

The waveguiding structure studied throughout this work is shown schematically in Fig. II.1, together with the coordinates. It is made of glass, a nonconductive dielectric material. The wave propagation is directed along the z axis.

Due to the properties of these structures, in particular of the ion-exchanged waveguides in glass used in the experiments, several approximations can be used. They are described hereafter.

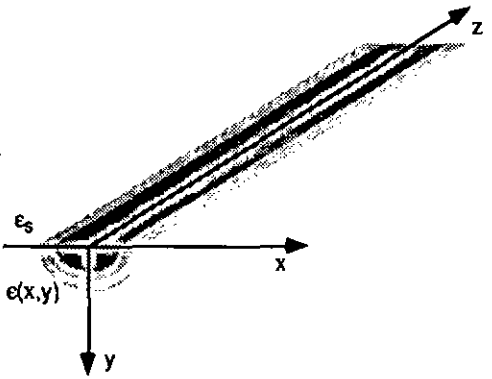

Fig. II.1 Scheme of a general guiding structure

The scalar wave equation

The mathematical description of optical wave propagation starts with the Maxwell equations (see [27]) which can be simplified by two properties of dielectric materials: no space charge and no electrical conductance exist in the glass (ρ=0 and σ=0, respectively). A further simplification is caused by the isotropy of the media: the dielectric constant ε and magnetic permeability μ are scalar values. In addition, the magnetic permeability is constant and equal to the one of free-space ($\mu=\mu_0$). Finally, it is assumed that the electromagnetic fields vary periodically with time. This dependence is taken into account by the expression:

$$\mathbf{E}(x, y, z, t) = \mathbf{E}(x, y, z)e^{j\omega t} + \mathbf{E}^*(x, y, z)e^{-j\omega t} \qquad \text{(II.1)}$$

where $\omega=2\pi\nu$ is the angular frequency

From these statements and the Maxwell equations, it is possible to derive a vector wave equation, involving terms of the form: $\nabla \ln \varepsilon$ ([28], p. 61). These terms can be neglected if it is assumed that refractive index gradients are small. This is the weak guidance hypothesis, which is closely met in the case of waveguides made by ion-exchange. Furthermore, the dielectric constant $\varepsilon(x,y)$ does not depend on the z propagation axis. Therefore, the solutions of the vector wave equation are separable with a term: $e^{-j\beta z}$. For instance, the electric field is given by:

$$\mathbf{E}(x, y, z) = \boldsymbol{E}(x, y)e^{-j\beta z} \qquad \text{(II.2)}$$

where $\boldsymbol{E}(x,y)$ is the modal field and
β is the propagation constant (with $\mathrm{Re}\{\beta\}>0$ for forward propagating modes).

The usual separation of the modal fields $\boldsymbol{E}=(E_x\ E_y\ E_z)$ and $\boldsymbol{H}=(H_x\ H_y\ H_z)$ into their tranverse and longitudinal components is applied in our study, namely:

$$\boldsymbol{E}_t=(E_x\ E_y\ 0) \text{ and} \tag{II.3a}$$

$$\boldsymbol{H}_t=(H_x\ H_y\ 0) \tag{II.3b}$$

for the transverse fields and:

$$\boldsymbol{E}_z=(0\ 0\ E_z) \text{ and} \tag{II.4a}$$

$$\boldsymbol{H}_z=(0\ 0\ H_z) \tag{II.4b}$$

for the longitudinal ones.

With the weak guidance assumption, the modal description and equations (II.3) and (II.4), two scalar wave equations can be derived (see for example Kogelnik [28]), one for the electric field, the other for the magnetic one:

$$\nabla^2\boldsymbol{E}_t(x,y) + (\omega^2\varepsilon\mu_0 - \beta^2)\boldsymbol{E}_t(x,y) = 0 \tag{II.5a}$$

$$\nabla^2\boldsymbol{H}_t(x,y) + (\omega^2\varepsilon\mu_0 - \beta^2)\boldsymbol{H}_t(x,y) = 0 \tag{II.5b}$$

where $\boldsymbol{E}_t(x,y)$ is the transverse electric field
$\boldsymbol{H}_t(x,y)$ the transverse magnetic field
μ_0 the free-space permeability
$\varepsilon=\varepsilon_0\, n^2(x,y)$ the dielectric constant of the medium
β the propagation constant

In fact, solving only one of the scalar wave equations (II.5a) or (II.5b) completely determines the fields. Indeed, the longitudinal components can be expressed as a function of the transverse ones by:

$$j\beta\boldsymbol{E}_z = \nabla\cdot\boldsymbol{E}_t \text{ and} \tag{II.6a}$$

$$j\beta\boldsymbol{H}_z = \nabla\cdot\boldsymbol{H}_t \tag{II.6b}$$

For example, calculating the vector $\boldsymbol{E}_t$ from (II.5a) leads to the longitudinal component $\boldsymbol{E}_z$ from (II.6a). Then, the magnetic field $\boldsymbol{H}$ can be calculated from the Maxwell equations.

Eigensolutions

The scalar wave equations (II.5a) and (II.5b) have two distinct sets of solutions. The first one has a continuous distribution of eigenvalues β. It corresponds to radiation modes. Their power close to or in the waveguide usually decays with propagation [29]. For the sake of simplicity, we assume that these modes have little influence when measuring the output intensity distribution. For that reason, they are ignored throughout this work.

The other set is the one of guided modes, with a discrete and finite distribution of eigenvalues β. In order to distinguish the various eigenvalues, one label for each direction x and y should be added to the propagation constant and the corresponding eigenfield. In fact, the waveguiding structures involved in this study are single-mode along the y-coordinate. Therefore, the corresponding mode label is not introduced in our description. With this convention, the effective index is defined by:

$$\beta_i = n_{ei} k_0 \qquad i=0,..,N \tag{II.7}$$

where k_0 is the propagation constant in free-space
n_{ei} is the effective index of mode i
N is the highest mode order along the x-axis

To each eigenvalue β_i corresponds a transverse electric eigenfield $\mathscr{E}_i(x,y)$ and a transverse magnetic eigenfield $\mathscr{H}_i(x,y)$, where the subscript t is omitted for the sake of clarity.

Orthogonality and normalization

It can be shown from the Maxwell equations that the eigenfields are orthogonal in the sense that:

$$\int_{\mathscr{A}} \mathscr{E}_i(x,y) \times \mathscr{H}_k^*(x,y) d\mathscr{A} = 0 \qquad \beta_i \neq \beta_k \tag{II.8}$$

where $\mathscr{A}$ is the transverse section of the waveguide, extending to infinity

Furthermore, the modal fields are normalized in such a way that the cross

power $\bar{P}$ is equal to unity:

$$\bar{P} = 2\int_{\mathcal{A}} \mathcal{E}_i(x,y) \times \mathcal{H}_k^*(x,y)\,d\mathcal{A} = \delta_{ik} \qquad \text{(II.9)}$$

where δ_{ik} is the Kronecker symbol

TE and TM modes

Because we have neglected $\nabla \ln\varepsilon$ terms in the vector wave equation, it is possible to distinguish two polarization modes, the Transverse Electric (TE) and Transverse Magnetic (TM) modes. They are defined by a zero longitudinal component:

$$\mathcal{E}_{zi}^{TE} = 0 \text{ and } \mathcal{H}_{zi}^{TM} = 0 \qquad \text{(II.10a) and (II.10b)}$$

for TE and TM modes respectively.

For TE modes, the Maxwell equations impose:

$$\mathcal{E}_i^{TE} = (\mathcal{E}_{xi}, 0, 0),\ \mathcal{H}_i^{TE} = (0, \mathcal{H}_{yi}, \mathcal{H}_{zi}) \qquad \text{(II.11a) (II.11b)}$$

and

$$\beta_i \mathcal{E}_{xi} = -\omega\mu\,\mathcal{H}_{yi} \qquad \text{(II.12)}$$

On the other hand, one gets from equation (II.6a):

$$\partial\mathcal{E}_{xi}/\partial y = -j\omega\mu\,\mathcal{H}_{zi} \qquad \text{(II.13)}$$

For TM modes, relations (II.11) to (II.13) become:

$$\mathcal{E}_i^{TM} = (0, \mathcal{E}_{yi}, \mathcal{E}_{zi}),\ \mathcal{H}_i^{TM} = (\mathcal{H}_{xi}, 0, 0) \qquad \text{(II.14)}$$

$$\beta_i \mathcal{H}_{xi} = -\omega\varepsilon\,\mathcal{E}_{yi} \text{ and} \qquad \text{(II.15)}$$

$$\partial\mathcal{H}_{xi}/\partial y = -j\omega\varepsilon\,\mathcal{E}_{zi} \qquad \text{(II.16)}$$

With step-index profiles, the wave equation is the same for both polarizations:

$$\frac{\partial^2\psi}{\partial y^2} = (\beta^2 - n^2k^2)\,\psi \qquad \text{(II.17)}$$

where ψ stands for $\mathcal{E}_{xi}$ for TE modes and $\mathcal{H}_{xi}$ for TM ones, and n=n(y)

Now, we can describe a guided field with the help of the eigensolutions.

II.2. GENERAL EXPRESSIONS OF GUIDED FIELDS

A general field can be expressed by a linear combination of the eigenfields, propagating either in the positive or in the negative direction of the z axis. These are the forward and the backward propagating waves, respectively. Only forward propagating waves are considered in this study. They are given by:

$$E_t(x,y) = \sum_{i=0}^{N} A_i \mathscr{E}_{ti}(x,y) \tag{II.17}$$

where A_i is the complex coefficient of mode i, given by:

$$A_i = a_i e^{j\varphi_i} = a_i e^{-j\beta_i z} \tag{II.19}$$

with a_i the amplitude of mode i
φ_i its phase

Equation (II.18) yields for TE modes:

$$E_x(x,y) = \sum_{i=0}^{N} A_i \mathscr{E}_{xi}(x,y) \tag{II.20}$$

where $\mathscr{E}_{xi}$ are the eigenfields

With the help of equation (II.12), one gets:

$$H_y(x,y) = \frac{-1}{\omega\mu} \sum_{i=0}^{N} A_i \beta_i \mathscr{E}_{xi}(x,y) \tag{II.21}$$

It is possible now to calculate the intensity distribution given by these fields. This is expressed by the Poynting vector.

Poynting vector

With the time dependence expressed by equation (II.1), the time-averaged Poynting vector is given by:

$$S(x,y) = E \times H^* + E^* \times H \tag{II.22}$$

For TE modes, the components S_x and S_y are equal to zero, while S_z is given by:

$$S_z = -E_x H_y^* - E_x^* H_y \tag{II.23}$$

With (II.20) and (II.21), this relation can be expressed in a matrix form:

$$S_z(x, y) = \frac{2}{\omega\mu} \mathbf{A}^* \mathbf{M} \mathbf{A} \tag{II.24}$$

where $\mathbf{M} = \begin{pmatrix} \beta_0 \mathscr{E}_0^* \mathscr{E}_0 & \frac{\beta_0+\beta_1}{2} \mathscr{E}_0^* \mathscr{E}_1 & \cdots & \frac{\beta_0+\beta_N}{2} \mathscr{E}_0^* \mathscr{E}_N \\ \frac{\beta_1+\beta_0}{2} \mathscr{E}_1^* \mathscr{E}_0 & \beta_1 \mathscr{E}_1^* \mathscr{E}_1 & \cdots & \frac{\beta_1+\beta_N}{2} \mathscr{E}_1^* \mathscr{E}_N \\ \vdots & \vdots & \ddots & \vdots \\ \frac{\beta_N+\beta_0}{2} \mathscr{E}_N^* \mathscr{E}_0 & \frac{\beta_N+\beta_1}{2} \mathscr{E}_N^* \mathscr{E}_1 & \cdots & \beta_N \mathscr{E}_N^* \mathscr{E}_N \end{pmatrix}$

$$\mathbf{A} = \begin{pmatrix} A_0 \\ A_1 \\ \vdots \\ A_N \end{pmatrix}$$

Written in this form, the matrix **M** is a Hermitian matrix, i.e.:

$$M_{ik} = M_{ki}^*$$

As shown by Snyder and Love [27, Section 30-4], the tranverse components of the eigenfields can be chosen real. Then, the matrix **M**, made of the tranverse electric eigenfield $\mathscr{E}_i$, is symmetric.

Guided power

Now the total power guided by the structure is given by the integral of the Poynting vector over the entire tranverse section. For TE modes:

$$P_0 = \int_{\mathscr{A}} S_z(x, y) \mathrm{d}\mathscr{A} \tag{II.25}$$

By decomposing (II.25) with (II.24), and making use of the orthogonality relation (II.8), we obtain:

$$P_0 = \int_{\mathscr{A}} S_z(x, y) \mathrm{d}\mathscr{A} = \sum_{i=0}^{N} A_i^* A_i \tag{II.26}$$

This formula will be specially important in Chapter IV for normalization purposes.

II.3. CALCULATION OF EIGENVALUES AND EIGENFIELDS

Several methods have been proposed for the calculation of eigenvalues and eigenfields, both in planar and confined waveguides (see [28] for a review). In principle, any of these methods can be applied for output the intensity distribution analysis.

In this work, the Transfer Matrix Method was chosen for calculating the eigenfields and eigenvalues of planar waveguides. For laterally confined waveguides, the Effective Index Method is applied. Both methods offer a surprisingly good accuracy and, at the same time, do not need long computing time. Therefore they are ideal for a laboratory set-up, such the one described in this work.

II.3.1. Planar waveguides

Only a few index profiles lead to analytical solution of the wave equation. In particular, the case of ion-exchanged waveguides (see chapter III) cannot be calculated analytically. Therefore, we apply an approximate numerical method, described hereafter.

The Transfer Matrix Method

A convenient way to solve the scalar waveguide equation in the case of gradient index waveguide is to choose a step-like approximation of the gradient profile. This leads to an equivalent multilayer waveguide, as shown in Fig. II.2.

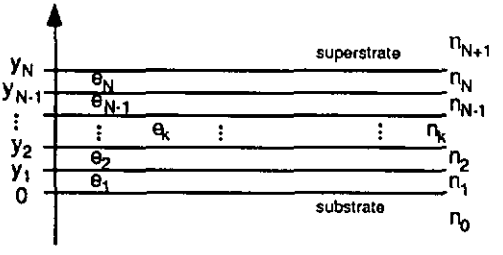

Fig. II.2 Multilayer waveguiding structure

In order to solve the wave equation in such structures, a method deriving from the multilayer stack theory was used. This method has been published recently by B. Jonsson and S.T. Eng [30] for solving the

Schrödinger equation, where it is called the Transfer Matrix Method. The mathematical developments are reminded here for electromagnetic fields.

In the structure shown in Fig. II.2, made of several layers of different widths and indices, the electric field $\mathcal{E}_{xk}$ of a TE mode in layer k is expressed by:

$$\mathcal{E}_{xk} = \mathcal{E}_k^+ \exp\{\delta_k y\} + \mathcal{E}_k^- \exp\{-\delta_k y\} \qquad \text{(II.27)}$$

where $\delta_k = \sqrt{\beta^2 - n_k^2 k_0^2}$

The indices for mode order i are omitted for the sake of clarity.

With equation (II.12), one gets for $\mathcal{H}_{zk}$ in layer k:

$$\mathcal{H}_{zk} = \frac{1}{-j\omega\mu}(\delta_k \mathcal{E}_k^+ \exp\{\delta_k y\} - \delta_k \mathcal{E}_k^- \exp\{-\delta_k y\}) \qquad \text{(II.28)}$$

Obviously δ_k takes a real value when the propagation constant β is greater than $n_k k_0$ and an imaginary value in the opposite case. The latter case leads to a field with a sinusoidal shape, characteristic of a guiding layer.

The Maxwell equations implicitly impose continuity conditions at an interface: on the one hand, of the electric field component tangent to the interface, on the other hand, of the longitudinal magnetic field. For TE modes, this yields:

$$\mathcal{E}_{xk}(y_k) = \mathcal{E}_{x(k+1)}(y_k) \qquad \text{(II.29)}$$

$$\mathcal{H}_{zk}(x_k) = \mathcal{H}_{z(k+1)}(x_k) \qquad \text{(II.30)}$$

With (II.27) and (II.28), one can rewrite (II.29) and (II.30) in a vectorial form:

$$\begin{pmatrix} \mathcal{E}_{k+1}^+ \\ \mathcal{E}_{k+1}^- \end{pmatrix} = \begin{pmatrix} \frac{1}{2}\left(1 + \frac{\delta_k}{\delta_{k+1}}\right)e^{\delta_k c_k} & \frac{1}{2}\left(1 - \frac{\delta_k}{\delta_{k+1}}\right)e^{-\delta_k c_k} \\ \frac{1}{2}\left(1 - \frac{\delta_k}{\delta_{k+1}}\right)e^{\delta_k c_k} & \frac{1}{2}\left(1 + \frac{\delta_k}{\delta_{k+1}}\right)e^{-\delta_k c_k} \end{pmatrix} \begin{pmatrix} \mathcal{E}_k^+ \\ \mathcal{E}_k^- \end{pmatrix} \qquad \text{(II.31)}$$

Once $\mathcal{E}_0^+$ and $\mathcal{E}_0^-$ are known, all coefficients $\mathcal{E}_k^+$ and $\mathcal{E}_k^-$ can be calculated from (II.31). Denoting the matrix of (II.31) by the symbol L_k, one can derive $\mathcal{E}_{N+1}^+$ and $\mathcal{E}_{N+1}^-$, namely:

$$\begin{pmatrix} \mathcal{E}_{N+1}^+ \\ \mathcal{E}_{N+1}^- \end{pmatrix} = L \begin{pmatrix} \mathcal{E}_0^+ \\ \mathcal{E}_0^- \end{pmatrix} = L_N L_{N-1} \cdots L_k \cdots L_1 L_0 \begin{pmatrix} \mathcal{E}_0^+ \\ \mathcal{E}_0^- \end{pmatrix} \qquad \text{(II.32)}$$

The coefficient $\mathcal{E}_0^-$ is given by a physical consideration. In order to keep a finite power, its value has to be zero. Otherwise, the field tends to infinity far from the waveguide. The value of $\mathcal{E}_0^+$ is given by the normalization condition: the power carried by the eigenmode must by unity (see Section II.1). For the reason which imposed $\mathcal{E}_0^- = 0$, we also need $\mathcal{E}_{N+1}^+ = 0$. This is the case when β corresponds to an eigenvalue β_i. Thus we have:

$$\mathcal{E}_{N+1}^+(\beta_i) = 0 \qquad \text{(II.33)}$$

and the roots of equation (II.33) lead to the eigenmode propagation constants. An algorithm has been developped for computing all propagation constants β_i. It will not be detailed here.

II.3.2. Laterally confined waveguides

The calculation of laterally confined structures are much more complicated than planar waveguides, even when the approximation of the scalar wave equation is used. Several methods have been presented for that purpose. This goes from the variable separation of Marcatili [30], simple but inaccurate, up to numerical methods applied to the full vectorial wave equation [32], accurate but requiring high computing power.

The method first presented by Knox and Toulios [33] is quite simple, though surprisingly accurate, and it does not require long computing time. These reasons explain the wide use of this method, which calculates the three-dimensional waveguide by two successive calculation of equivalent planar structures, one for each coordinate axis.

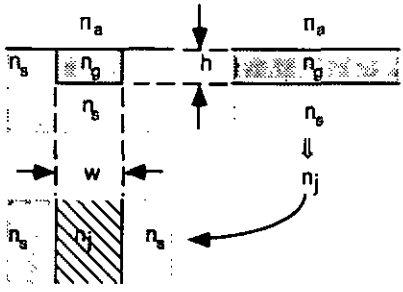

Fig. II.3 Equivalent structures for the Effective Index Method

First, the effective indices n_j of an infinitely wide layer, with the same depth h and index n_g as the waveguide (see Fig. II.3), are calculated as a planar structure. In the second step, a planar structure is again computed, using the same width w as the waveguide, but with the effective indices n_j as the refractive index of the core. This leads to the effective indices n_{ij} of the full structure. This method, in spite of its simplicity, gives fairly good results, as shown by Hocker and Burns [34].

If necessary, the eigenfields can be approximated along the x and y coordinates by:

$$\mathcal{E}_{ij}(x, y) = \mathcal{E}_i(x, n_{ij})\mathcal{E}_j(y, n_j) \qquad \text{(II.34)}$$

But in usual, most structures of interest are single-mode in depth, i.e. j=0. In particular, this is the case of the structures studied in our experiments. Thus, their behaviour along the y axis is not considered and the index j=0 is omitted. This convention is adopted in the present work.

CHAPTER III

FABRICATION OF ION-EXCHANGED WAVEGUIDES IN BK7 GLASS

This chapter briefly describes the optical waveguide technology applied to optical waveguide fabrication at CSEM. Thorough descriptions can be found in textbooks [35]. However, the choice of technological parameters is presented in more details.

III.1. GENERAL DESCRIPTION

The glass used at CSEM is mainly made of an amorphous matrix of silicon dioxide, which contains small amounts of sodium and potassium oxides. For changing the refractive index, the glass composition is locally modified by immersing the glass wafer into an molten salt bath. A diffusion process creates a migration of the dopant ions from the bath into the glass. In order to maintain the equilibrium of electric charges, the sodium ions migrate from the glass into the bath. This technique is called an ion exchange process.

This process is well known to reinforce the mechanical properties of glass, where it induces a compressive stress at the surface. It is called in this case chemical strengthening. However, this technique was used only recently in the fabrication of optical waveguides. The first papers in this field were published in 1972 [36]. Since then, several ions have been studied, for instance: potassium, silver, caesium, rubidium [37] or thallium [36]. Metallic layers have been used as ion sources for a few years [38]. In this case, the ion diffusion is induced by an electric field. This technique created new index profiles, in particular embedded or step-index profiles.

Optical waveguides are fabricated for this thesis at CSEM, by a purely thermal ion-exchange process: the glass wafers are immersed into a high temperature potassium nitrate bath for several hours. The substrate is the

Schott BK7 glass. The main features of the waveguides made by this process are:

- the index difference close to that one of optical fibres: 10^{-2}
- the weak propagation loss, of 0.1 dB/cm approximately
- the strong birefringence: about 50 rad/cm

This BK7 glass is well known for the ion-exchange technology [39]. It leads to complementary error fonction (Erfc(x)) refractive index profiles, according to the diffusion theory from an infinite ion source. This profile is depicted below (Fig. III.1) for a waveguide diffused for 50h at 380°C in a pure potassium nitrate molten salt.

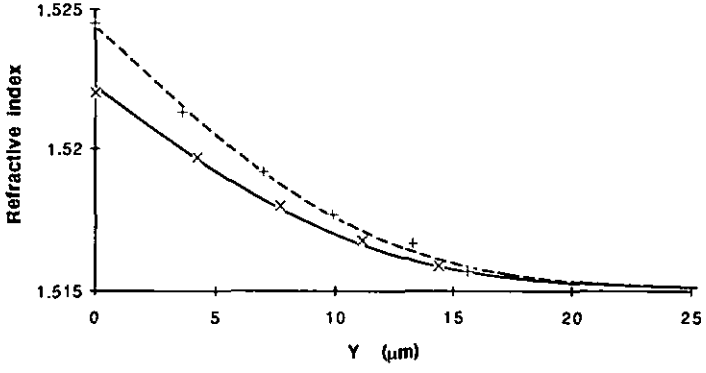

Fig.III.1 Diffusion profile for K^+-exchanged BK7 glass, together with a fitted complementary error fonction
Solid line: fitted Erfc for TE modes; dashed line: fined Erfc for TM modes; crosses: measured refractive index profiles
Ion-exchange: 50h, 380°C

Note also that the waveguides made by potassium exchange do not result from the polarizability of potassium ions, but by the compressive stress, induced by replacing ions with small ionic radius (sodium) by larger ions (potassium). This feature implies two important properties of such waveguides. The first one is the anomalous birefringence shown by potassium exchanged waveguides: the effective indices of TM modes are higher than the ones of TE modes. Therefore, the refractive index profile is different for TE than for TM modes. These particular birefringence

properties have been thoroughly studied [40]. The second consequence is that the polarization eigenaxes, i.e. the axes for which no coupling occurs between both eigenpolarizations, are not constant over the cross-section of the waveguide. This situation is sketched in Fig. III.2.

Fig. III.2 Eigenaxes of the polarization, typical of a potassium exchanged waveguide

This birefringence property has been studied in the PhD thesis of C. Visconti [41]. Consequently, the refractive index of such waveguides should be described by a tensor, not by a scalar value. Coupling between TE and TM modes can result from this particular feature. This is in contradiction with the assumption retained in Chapter II, namely the use of the scalar wave equation. However, this position dependent birefringence is weak, as is the coupling efficiency between TE and TM modes: in a 58 µm wide and 8 mm long waveguide, the coupling efficiency has been measured to be about -15dB. Because this effect is weak, we expect that the assumptions still correctly describe the propagation in ion-exchanged waveguide. Therefore, the variation of polarization eigenaxes over the cross section of the waveguide will be neglected in our study.

III.2. FABRICATION PROCESS

The fabrication of channel waveguides by the ion-exchange technology requires several operations. The main ones are briefly described hereafter:

- metallic layer deposition, used as ionic barrier (aluminium layer)

- photoresist deposition

- photolithographic mask transfer by UV illumination, followed by the photoresist development

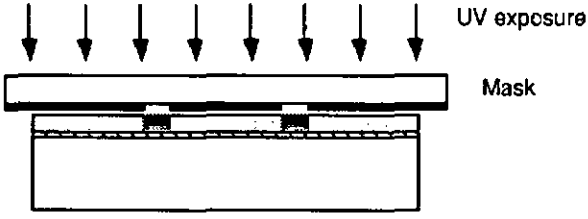

- etching of the metallic layer

- ion exchange in molten potassium nitrate

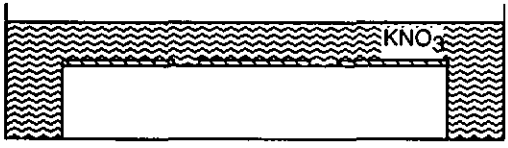

After these planar operations, the glass wafers are sawed according to the waveguide structures, and the end-faces are polished. Then samples are ready for use.

III.3. DESIGN AND PROPERTIES OF FABRICATED WAVEGUIDES

The main goal of this work is the analysis of waveguiding structures used for realizing an optical phase demodulator [22]. Therefore, the process parameters have been optimized for this purpose. To do so, we first had to observe the light propagation in the waveguide: this is described in paragraph III.3.1. We deduced in paragraph III.3.2 the optimized parameters from these observations.

III.3.1. Guided field observation

Two phenomena enable the observation of guided fields. The first one is called the Rayleigh scattering. Inside a waveguide or a glass structure, light

is scattered by the fluctuations of density and refractive index of the glass matrix. For a theoretical or perfect glass structure, the Rayleigh scattering is proportional to the guided intensity. As a consequence, observation of the guided mode is possible. The second phenomenon was first proposed as a method for measuring propagation loss in optical waveguides [42]. A solution of laser dye is spread on top of the waveguide, in the evanescent part of the guided field. The atoms of the dye get into an excited state by absorbing the evanescent part of the guided wave. Then, they come back to their ground state by emitting incoherent light at a longer wavelength. The emitted power is proportional to the absorbed power, therefore to the square of the evanescent field amplitude.

For experiments with HeNe laser, we used Nile blue laser dye, dissolved in ethylenglycol. The fluorescence wavelength is 656 nm. A drop of the solution is deposited on the glass substrate and covered by a microscope slide. Then, light emitted by the laser dye is observed with a microscope, using the set-up sketched in Fig. III.3. The presence of ethylenglycol changes the propagation constants of the waveguide, as well as the intermodal dispersion and propagation loss. This effect must be taken into account for the design of integrated optic devices operating with air as a superstrate.

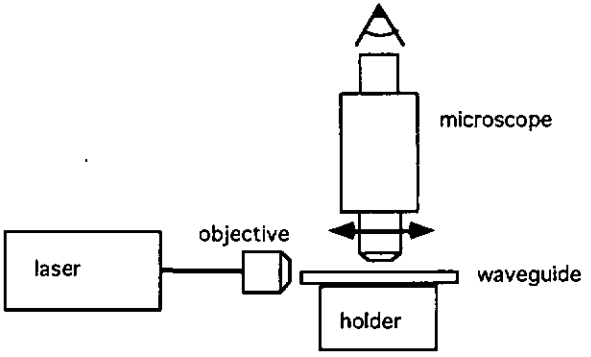

Fig. III.3 Set-up for observing light propagating in an integrated optic waveguide

The microscope is mounted onto a translation table, allowing the scanning of the waveguide. So, the characteristic length for the formation of a fourfold image in the waveguide can be measured.

III.3.2. Influence of process parameters

Preliminary experiments showed the process parameters required for single-mode operation of channel waveguides. So, we determined the mask opening width and the diffusion time and temperature necessary for obtaining single-mode waveguides [43].

Using these parameters, Multimode Interference (MMI) waveguides, with three different mask opening widths, were ion-exchanged. The resulting waveguide widths were 26 μm, 50 μm and 58 μm. Next, with the help of the observation set-up described in Fig. III.3, the guided light has been observed, in particular the formation of fourfold images. The best image resolution was achieved for the TE modes propagating in the largest waveguides. The fourfold image formation is shown in Fig. III.4 [44]. Regarding the TM modes, the image formation had a poorer resolution than TE modes, for any diffusion conditions. This effect is probably due to the refractive index profile for TM modes, which is different from the profile for TE modes. Therefore, the optical phase demodulator is polarization sensitive.

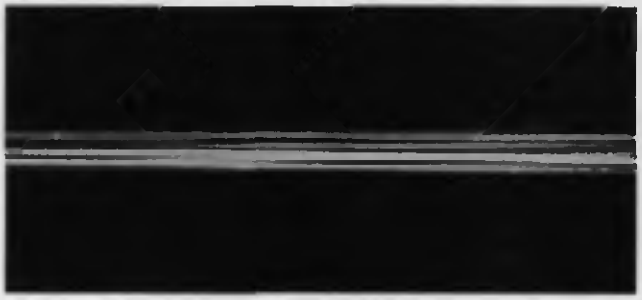

Fig. III.3 Fourfold image formation in an integrated optic waveguide, with TE modes; waveguide width: 58 μm

The perturbation induced by the ethylenglycol solution was clearly observed by analysing the necessary waveguide length to obtain the optimal fourfold image. For a wavelength of 633 nm and TE polarization, the variation of this length is significant: 7.76 mm with the covering solution on top of the guide, and 7.43 mm without it. The difference is also important between TE and TM modes. TM modes require a 10.1 mm propagation length for the fourfold image formation with ethylenglycol.

In summary, all waveguide samples used in our experiments were made by ion-exchange in BK7 glass, using pure potassium nitrate molten salt. The index profiles of single-mode waveguide are extrapolated from the complementary error profiles obtained for longer diffusion time: the maximum index reaches $8 \cdot 10^{-3}$, and the characteristic diffusion depth is about 1.5 μm. The realized structures include three- and four-branch directional couplers, both consisting of parallel single-mode waveguides, as well as single section multimode waveguides, with widths ranging from 10 μm to 100 μm.

CHAPTER IV

METHOD FOR THE ANALYSIS OF THE OUTPUT INTENSITY DISTRIBUTION

In the Introduction, it was stated that the effective index differences can be determined, using: the excitation mode coefficients, the output intensity distribution and the eigenfields of the waveguide. Chapter II already presented the calculation of the eigenfields. In the present Chapter, we first describe the injection conditions leading to known excitation mode coefficients. In Section IV.3, the conditions for properly measuring the output intensity distribution are exposed.

From these prerequisites, the output mode coefficients can be calculated by the algorithm described in Section IV.4. Then, Section IV.5 discusses the calculation of the optical phase differences introduced between the guided modes by propagation. The effective index differences can be finally deduced.

IV.1. INPUT COUPLING USING A FOCUSED GAUSSIAN BEAM

A focused Gaussian beam is an easy and efficient way for injecting light in a waveguide. In this Section, we briefly analyse the characteristics of this type of excitation. Our purpose is to determine the coupling efficiency for each guided mode, in terms of modulus and phase. Some error sources are presented and their effect briefly discussed. In this work, we consider a focused Gaussian beam, launched with a incident angle into the waveguide input (see Fig. IV.1).

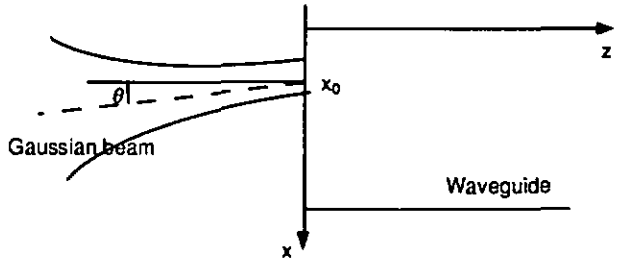

Fig. IV.1 Focused Gaussian beam, incident at the waveguide input

In the Effective Index Method assumed in this work, only the x coordinate is considered. Therefore, the electric field of the Gaussian beam with a small incidence angle θ is approximated at the beam waist by the equation:

$$E_G(x) = \frac{E_0}{r_0} \cdot \sqrt{\frac{2}{\pi}} \exp\left\{-\frac{(x-x_0)^2}{r_0^2}\right\} e^{j\varphi(x)} \qquad \text{(IV.1)}$$

with E_0 the amplitude
r_0 the beam radius
x_0 the position of the beam centre and
$\varphi(x)$ is a phase term given by

$$\varphi(x) = k_0(x - x_0)\mathrm{tg}\vartheta \qquad \text{(IV.2)}$$

where θ is the incidence angle at the waveguide input

This beam is normalized with the help of:

$$|\psi|^2 = \int_{-\infty}^{\infty} \psi\psi^* dx = 1 \qquad \text{(IV.3)}$$

where ψ holds for the Gaussian field $E_G(x)$. This leads to: E_0=1.

Using the Gaussian beam $E_G(x)$ as an input light source, the excitation mode coefficient A_i^c of the ith mode is given by the overlap integral:

$$A_i^c = \int_{-\infty}^{\infty} E_G(x)\mathcal{E}_i(x)dx \qquad \text{(IV.4)}$$

where the real eigenfield $\mathcal{E}_i(x)$ has been normalized with the help of equation (IV.3). The amplitude of mode i, i.e. the modulus of A_i^c, is

represented in Fig. IV.2 versus the Gaussian beam position, for a 30 μm wide waveguide and a 3 μm wide Gaussian beam.

When its radius r_0 tends to zero, the Gaussian beam becomes a Dirac field distribution $E_D\delta(x - x_0)$, where x_0 is the position of the Dirac distribution. Here, the normalization with (IV.3) yields E_D=1. Then, the excitation mode coefficient of mode i is given by the simple relation:

$$A_i^e = \mathcal{E}_i^e(x_0) \qquad \text{(IV.5)}$$

The excitation mode coefficient of order 3 is shown in Fig. IV.2, assuming a normal incidence Gaussian beam, i.e. θ=0, and a Dirac distribution of the field. The waveguide is 30 μm wide, the Gaussian beam radius r_0= 3 μm.

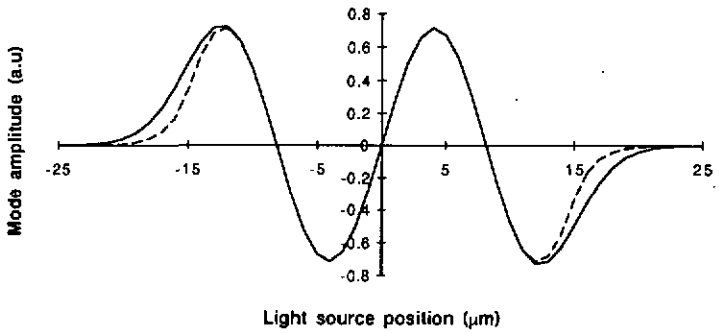

Fig. IV.2 Modulus of the excitation mode coefficient of mode 3, calculated with a Gaussian beam excitation (dashed line) and with a Dirac distribution (solid line), as a function of the light source position x_0.
Gaussian beam: r_0= 3 μm; Waveguide: w_g=30 μm, n_g=1.5163, n_s=1.5151

One sees in Fig. IV.2 that the excitation amplitudes with a Dirac distribution are close to the ones calculated with Gaussian beam, except when the light source is located in the evanescent part of the eigenmode (x_0≈-15 μm or x_0≈15 μm). This discrepancy can be reduced by using a narrower Gaussian beam. Plotting similarly the excitation mode amplitudes as a function of the incidence angle θ would show only little influence. However, we show now that the phases of the excitation mode coefficients

are more sensitive to the incidence angle than the amplitudes of the excitation mode coefficients.

In Fig. IV.3, the phase of the excitation mode coefficient A_3^e is shown for three incidence angles of a focused Gaussian beam with a r_0=2 μm radius. In the case of a Dirac distribution, the phase of the excitation coefficient is calculated from equation (IV.5): it is thus always real, since the eigenfields are expressed by real values. Therefore, the excitation mode coefficients A_i^e have a phase equal to either 0 or π.

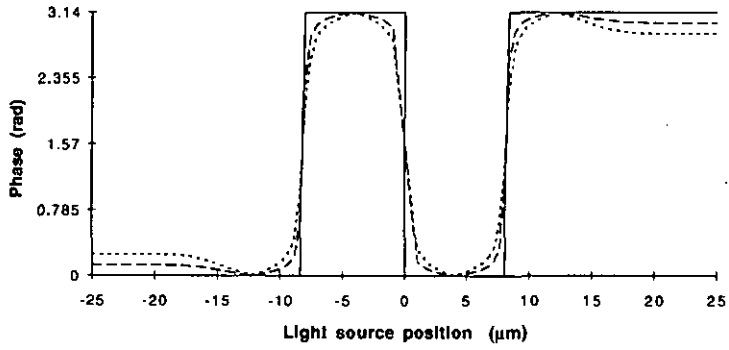

Fig. IV.3 Absolute optical phase of the excitation mode coefficient A_3^e, versus the light source position x_0, for a Gaussian beam with radius r_0=2 μm; solid line: incidence angle θ=0; dashed line: θ=0.5°; dotted line: θ=1°.
Waveguide: w_g=30 μm, n_g=1.5163, n_s=1.5151 (similar to Fig. IV.2)

It is clearly seen that the phase of A_i^e is close to 0 or π when the incident angle is equal to zero, meaning that the Dirac distribution can be used as an approximation of the Gaussian beam. However, when the incidence angle is not normal, a difference appears between both descriptions of the input light source. This leads to a conclusion holding for the experimental conditions: the incidence angle of the focused Gaussian beam must be maintained within ±0.5°, so that the phase of the excitation mode coefficients are close to either 0 or π.

A similar conclusion can be derived concerning the radius of the Gaussian beam, which also influences the phase of the excitation mode coefficients.

This is shown in Fig. IV.4 for a Gaussian beam with an incidence angle equal to 0.5°.

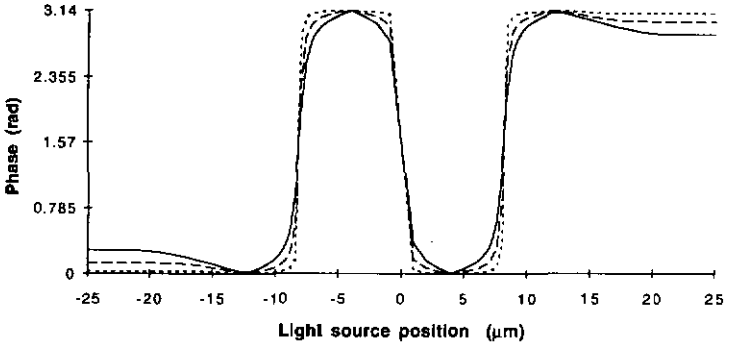

Fig. IV.4 Absolute optical phase of the excitation coefficient of mode 3, versus the light source position x_0, for a θ=0.5° incident Gaussian beam;
Solid line: beam radius r_0=3 µm; dashed line: r_0=2 µm; dotted line: r_0=1 µm
Waveguide: w_g=30 µm, n_g=1.5163, n_s=1.5151 (similar to Fig. IV.2)

As shown in Fig. IV.4, the narrowest Gaussian beam leads to an excitation mode coefficient A_i^e closer to 0 or π: the maximum difference is then 0.3 radians when the incident angle is equal to 0.5°.

Conclusion

A Dirac distribution of the excitation field can be considered as a good approximation of a Gaussian beam for calculating the amplitudes of the excitation mode coefficients. This remark applies even with a Gaussian beam radius as large as 3 µm, or with an incidence angle different from zero. However, regarding the phases of the excitation mode coefficients, a Gaussian beam must fulfil two conditions in order to be correctly approximated by a Dirac distribution of the input light source. First, the Gaussian beam radius should be smaller than 1 µm. This is typically achieved when the beam is focused to the diffraction limit. Second, the incidence angle into the waveguide input should be maintained smaller than 0.5°. To this aim, an alignment procedure is described in paragraph V.2.1.

IV.2. MEASUREMENT OF THE INTENSITY DISTRIBUTION

The output intensity distribution of a waveguiding structure is measured with the help of a magnifying objective, which images the waveguide output onto a light detector. This set-up is sketched in Fig. IV.5. In order to form an image free from aberrations, the numerical aperture of the microscope objective must be higher than the numerical aperture of the waveguide.

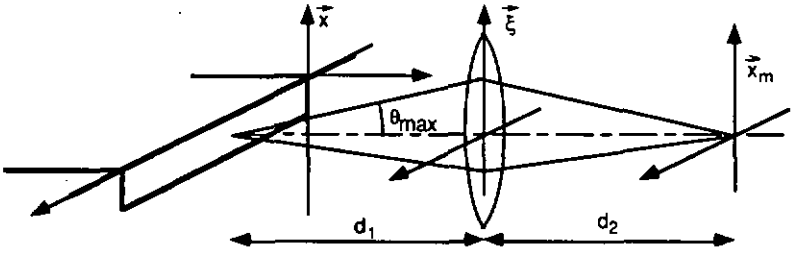

Fig. IV.5 Output intensity distribution measurement set-up, using a magnifying microscope objective and a detector located in the image plan $\vec{x}_m$

The resolution of the measuring system is also influenced by the size of the detector. The smallest resolved spot diameter in the object plane is related to the detector diameter in the image plane by the equation:

$$d = \frac{D}{M}$$

with d the resolved spot diameter
D the diameter of the detector and
M the magnification of the imaging system

For an optimum operation of the measurement system, the detector diameter must be lower or equal to the smallest resolved spot diameter given by the magnifying lens.

The numerical aperture and detector spot diameter conditions ensure the optimal operation of the magnifying system. Therefore, it will be checked in Chapter V that the experimental set-up fulfils both conditions.

IV.3. CALCULATION OF OUTPUT MODE COEFFICIENTS

IV.3.1 Introduction

Up to now, we have shown how the prerequisites can be obtained: the eigenfields $\mathcal{E}_i(x)$ were calculated in Section II.3, the excitation mode coefficients $\mathbf{A}_i^e$ in Section IV.2 and the measurement of the output intensity distribution was described in Section IV.3. We present now the algorithm used for retrieving the mode coefficients from the parameters mentioned above.

In this problem, we must find the complex vector $\mathbf{A}^T = (A_0 \;\; A_1 \;\; \cdots \;\; A_N)$, such that:

$$S_{out}(x) = S(x, \mathbf{A}) \tag{IV.6}$$

where $S_{out}(x)$ is the measured output intensity distribution and
$S(x,A)$ the intensity calculated from the eigenfields and the vector A

S(x,A) is given by (II.22):

$$S(x, \mathbf{A}) = \mathbf{A}^{\dagger}\mathbf{M}(x)\mathbf{A} \tag{IV.7}$$

It is interesting to note that this matrix **M** is highly singular, i.e. most of the eigenvalues are equal to zero. To show this, we observe that the matrix can be rewritten in the form:

$$\mathbf{M}(x) = \mathcal{E}^{\dagger}(x)\beta\mathcal{E}(x) \tag{IV.8}$$

where

$$\beta = \begin{pmatrix} \beta_0 & \frac{\beta_0+\beta_1}{2} & \cdots & \frac{\beta_0+\beta_N}{2} \\ \frac{\beta_1+\beta_0}{2} & \beta_1 & \cdots & \frac{\beta_1+\beta_N}{2} \\ \vdots & \vdots & \ddots & \vdots \\ \frac{\beta_N+\beta_0}{2} & \frac{\beta_N+\beta_1}{2} & \cdots & \beta_N \end{pmatrix} \text{ and} \tag{IV.9}$$

$$\mathcal{E}(x) = \begin{pmatrix} \mathcal{E}_0(x) & & & \mathbf{0} \\ & \mathcal{E}_1(x) & & \\ & & \ddots & \\ \mathbf{0} & & & \mathcal{E}_N(x) \end{pmatrix} \tag{IV.10}$$

The eigenvalues of matrix β are given by:

$$\lambda_0 = \tfrac{1}{2}\sum_{i=0}^{N}\beta_i + \tfrac{1}{2}R \qquad \text{(IV.11a)}$$

$$\lambda_1 = \tfrac{1}{2}\sum_{i=0}^{N}\beta_i - \tfrac{1}{2}R \qquad \text{(IV.11b)}$$

$$\lambda_i = 0 \qquad i = 2, 3, \ldots N \qquad \text{(IV.11c)}$$

with

$$R^2 = \left(\sum_{i=0}^{N}\beta_i\right)^2 + \tfrac{1}{2}\sum_{i,j=0}^{N}(\beta_i - \beta_j)^2 \qquad \text{(IV.12)}$$

Here, $\sum_{i,j=0}^{N}$ stands for a double summation for i and j.

The first two eigenvalues can be approximated by:

$$\lambda_0 \cong \sum_{i=0}^{N}\beta_i \qquad \text{(IV.13)}$$

$$\lambda_1 = \frac{\sum_{i,j=0}^{N}(\beta_i - \beta_j)^2}{8\lambda_0} \qquad \text{(IV.14)}$$

At first sight, this result seems to be interesting, because equation (IV.7) can be expressed in the eigenbase of the matrix β with the help of a diagonal matrix. We get:

$$S(x) = \mathbf{B}^{\dagger}(x)\,\Lambda\,\mathbf{B}(x) \qquad \text{(IV.15)}$$

where

$$\Lambda = \left(\begin{array}{cc:c} \lambda_0 & 0 & \\ 0 & \lambda_1 & 0 \\ \hdashline & 0 & 0 \end{array}\right) \qquad \text{(IV.16)}$$

and the vector $\mathbf{B}$ is given by:

$$\mathbf{B}(x) = \mathbf{Q}\,\mathscr{E}(x)\mathbf{A} \qquad \text{(IV.17)}$$

with $\mathbf{Q}$ the base matrix, made of the normalized eigenvectors.

Note that the base matrix $\mathbf{Q}$ is constant for a given waveguide.

With (IV.13) and (IV.14), equation (IV.17) reduces to:

$$S(x) = \lambda_0 B_0^*(x) B_0(x) + \lambda_1 B_1^*(x) B_1(x) \qquad \text{(IV.18)}$$

The complex values $B_0(x)$ and $B_1(x)$ cannot be deduced from the measurement of $S(x)$. Hence, this result does not yield a possible solution of the inverse problem.

Choice of a method

In the experiments, the intensity distribution measured at the waveguide output includes guided and radiation modes, whereas we choose to consider only the set of guided modes. In addition, the assumptions used for computing the eigenfields result in that the calculated eigenfields do not exactly match the ones of the actual waveguiding structure. Furthermore, measurement of the output intensity distribution is subjected to noise. Therefore, in the most general case, no vector $\mathbf{A}$ can satisfy the equation $S_{out}(x) = S(x, \mathbf{A})$ for every point x. Thus rigorous analytical methods are not convenient for calculating the mode coefficient vector $\mathbf{A}$ from the above equation.

However, the above conditions are closely met: the radiation modes are attenuated in the vicinity of the waveguide when they propagate; the calculated eigenfields are close to the actual ones; and the intensity measurement errors are small. Then, the following approximation is valid:

$$S_{out}(x) \cong S(x, \mathbf{A}) \qquad \text{(IV.19)}$$

In such a case, the most interesting method is to seek a best least square solution to the following system of equations:

$$r_k(\mathbf{A}) = S_{out}(x_k) - S(x_k, \mathbf{A}) \cong 0 \qquad \text{(IV.20)}$$

where $\mathbf{A}$ is the unknown mode coefficient vector
$S_{out}(x_k)$ is the intensity observed at point x_k
$S(x_k,\mathbf{A})$ is the intensity calculated from (IV.7)

r_k are called the residuals of $S(x_k,\mathbf{A})$.

The best probable solution is obtained by minimizing the squared error sum given by:

$$f(\mathbf{A}) = \sum_{k=1}^{M} \left\{ S_{out}(x_k) - S(x_k, \mathbf{A}) \right\}^2 \qquad \text{(IV.21)}$$

where M is the number of sampling points

Because of the periodicity of the mode coefficients (see equation IV.25), an unconstrained optimization algorithm can be used for the minimization of the squared error sum f(**A**). The algorithm for retrieving the mode coefficients from the intensity distribution is presented in paragraph IV.3.4. We first examine some conditions for a proper usage of this method.

Number of solutions

As it will be shown in this paragraph, equation (IV.7) have several solutions, linked by phase relations. Only one of them leads to the propagation characteristics in which we are interested. So we now examine this question, together with some conditions enabling to distinguish the right solution. For this purpose, we consider throughout this section that $\mathbf{A}_s = (A_{s0}, A_{s1}, \ldots, A_{sN})$ is the solution of (IV.7) that we are looking for.

With this assumption, $\mathbf{A}_s e^{j\varphi}$ is a solution of (IV.7), for any value of φ. We have:

$$\begin{aligned} S(x, \mathbf{A}_s e^{j\varphi}) &= \mathbf{A}_s^{\dagger} e^{-j\varphi} \mathbf{M} \mathbf{A}_s e^{j\varphi} = e^{-j\varphi} e^{j\varphi} \mathbf{A}_s^{\dagger} \mathbf{M} \mathbf{A}_s = \\ &= \mathbf{A}_s^{\dagger} \mathbf{M} \mathbf{A}_s = S(x, \mathbf{A}_s) \end{aligned} \qquad \text{(IV.22)}$$

In fact, this shows that the absolute phase cannot be retrieved by the simple measurement of the output intensity distribution, unless an external reference beam is used. As a result, only phase differences can be derived, thus only effective index differences. However, the operation principle of most integrated optic devices uses the effective index differences between modes, not on their absolute phases. Therefore, the analysing method proposed in this work remains of great interest. As a consequence of (IV.22), an arbitrary absolute phase can be chosen. This can be done by setting a condition for the fundamental mode:

$$\varphi_0 = 0 \qquad \text{(IV.23)}$$

Because of equation (IV.23), it must be noted that the phase difference between mode i and mode 0 coincides with the absolute phase of mode i: $\Delta\varphi_i = \varphi_i - \varphi_0 = \varphi_i$. Therefore, for the sake of a simpler notation, we will use phases φ_i instead of $\Delta\varphi_i$ hereafter. However, the effective index differences are calculated from the phase differences, although the assumption (IV.23) allows to use the phases instead (see Section IV.5).

Now we return to the search of other solutions of equation (IV.7) and show that the complex conjugate $\mathbf{A}_S^*$ of the vector $\mathbf{A}_s$, is also a solution of equation (IV.7):

$$\begin{aligned} S(x, \mathbf{A}_s^*) &= \mathbf{A}_s^{*\dagger}\mathbf{M}\mathbf{A}_s^* = (\mathbf{A}_s^{\dagger}\mathbf{M}^*\mathbf{A}_s)^* = \\ &= (\mathbf{A}_s^{\dagger}\mathbf{M}\mathbf{A}_s)^* = S(x, \mathbf{A}_s)^* = S(x, \mathbf{A}_s) \end{aligned} \qquad \text{(IV.24)}$$

This result is obtained because the matrix $\mathbf{M}$ is real, hence $\mathbf{M} = \mathbf{M}^*$, and S is real, yielding $S = S^*$.

Finally, if the mode coefficient vector $\mathbf{A}_s$ is a solution of (IV.7), then the vector $\mathbf{A}_s^p = (A_{s0}, A_{s1}e^{-j2m_1\pi}, \ldots, A_{sN}e^{-j2m_N\pi})$, m_i being integers, is also a solution. This comes from the periodicity of complex values, resulting in, for any integer m_i:

$$A_i = A_i\, e^{-j2m_i\pi} \qquad \text{(IV.25)}$$

The choice between $\mathbf{A}_s$ and its complex conjugate $\mathbf{A}_s^*$ on one hand, and of the integers m_i on the other hand, is treated in detail in Section IV.5. In the minimizing algorithm, complex numbers are expressed in Cartesian coordinates. Therefore, the following condition is always fulfilled:

$$0 \le \varphi_i < 2\pi \ . \qquad \text{(IV.26)}$$

All the above solutions result from phase relations, leaving unchanged the coefficient moduli $|A_i|$. However, the existence of solutions with different coefficient moduli cannot be excluded. This point is examined in Chapter V with the help of simulated intensity distributions. This problem is related to the presence of other local minima of the squared error sum $f(\mathbf{A})$.

IV.3.2 Implementation of the least square method

Choice of sampling points

In this problem, we have N+1 propagating modes, thus N+1 complex unknowns A_i. Because a complex number have an amplitude and phase, the number of real unknowns is 2(N+1). Now, as was stated in Section IV.3, the fundamental mode coefficient must be real positive, which reduces the number of unknowns. Finally, we have to determine 2N+1 parameters.

In order to solve a system with 2N+1 unknowns, we need at least 2N+1 independent equations for calculating the mode coefficient vector $\mathbf{A}_s$ unambiguously. This can be expressed by the condition:

$$M \geq 2N + 1 \qquad \text{(IV.27)}$$

where M is the number of sampling points, as used in (IV.21)

Now we determine some rules for a proper choice of sampling points. Our purpose is mainly to avoid ill-conditioned systems, for which solutions are very sensitive to small errors. We can illustrate this by a simple example: let us take a waveguide propagating only two guided modes. Then, the intensity distribution can be expressed by:

$$S(x) = a_0^2\mathcal{E}_0^2(x) + a_1^2\mathcal{E}_1^2(x) + 2a_0a_1\mathcal{E}_0(x)\mathcal{E}_1(x)\cos(\varphi_1 - \varphi_0) \qquad \text{(IV.28)}$$

where a_i is the amplitude of mode i

We further assume that the phase difference φ_1-φ_0 is equal to $\pi/2$. Then, a_0 and a_1 can be calculated with two equations, i.e. with two measurements of S(x), at point x_1 and x_2. This results in the system of equations:

$$\begin{aligned} S(x_1) &= a_0^2\mathcal{E}_0^2(x_1) + a_1^2\mathcal{E}_1^2(x_1) \\ S(x_2) &= a_0^2\mathcal{E}_0^2(x_2) + a_1^2\mathcal{E}_1^2(x_2) \end{aligned} \qquad \text{(IV.29)}$$

Solving for instance for a_0^2 gives:

$$a_0^2 = \frac{\mathcal{E}_1^2(x_1)S(x_2) - \mathcal{E}_1^2(x_2)S(x_1)}{\mathcal{E}_1^2(x_1)\mathcal{E}_0^2(x_2) - \mathcal{E}_1^2(x_2)\mathcal{E}_0^2(x_1)} \qquad \text{(IV.30)}$$

If we have $\mathcal{E}_i(x_1) \rightarrow \mathcal{E}_i(x_2)$, (i=0, 1), then the denominator of (IV.30) becomes very small. In such a case, slight changes of $S(x_1)$ or $S(x_2)$, due to

noise for instance, result in great variations of the amplitude a_0. The system is said to be ill-conditioned. A similar situation occurs with more than two modes, and for any phase differences between guided modes. So, more generally, once a sampling point x_l is chosen, we should not select a sampling point x_m for which:

$$\boldsymbol{e}(x_m) \approx k\boldsymbol{e}(x_l) \tag{IV.31}$$

where $\boldsymbol{e}(x) = \left(\mathcal{E}_0(x) \cdots \mathcal{E}_i(x) \cdots \mathcal{E}_N(x)\right)$ is a row vector, called the eigenfield vector at point x, and k is a real proportionality factor.

It can be observed that the row vectors $\boldsymbol{e}(x_l)$ and $\boldsymbol{e}(x_m)$ are collinear if the equality strictly holds in (IV.31). Collinearity can be studied with the help of the dot product of two vectors. So, let us define the function:

$$q(x_m, x_l) = \frac{\boldsymbol{e}(x_m)\boldsymbol{e}^T(x_l)}{\left|\boldsymbol{e}(x_m)\right| \cdot \left|\boldsymbol{e}(x_l)\right|} \tag{IV.32}$$

Obviously, $q(x_m,x_l)$ is equal to 1 or -1 when the eigenfield vectors $\boldsymbol{e}(x_l)$ and $\boldsymbol{e}(x_m)$ are collinear. It is zero when they are orthogonal. This function is illustrated in Fig. IV.6 for the case of a 24 μm wide waveguide, carrying four modes.

In Fig. IV.6, we choose a sampling point x_l=2.4 μm, depicted by a bold line. Then, one observes three sampling points x_m for which the eigenfield vector $\boldsymbol{e}(x_m)$ is orthogonal to $\boldsymbol{e}(x_l)$, i.e. for which $q(x_m,x_l)=0$. These points, pointed out by circles in Fig. IV.6, are x_m=-8.2 μm, -3.0 μm and 7.9 μm. How many locations leading to mutually orthogonal eigenfield vectors $\boldsymbol{e}(x)$ can be chosen? To calculate this, we build a matrix with the row vectors $\boldsymbol{e}(x_k)$ taken at several points x_k:

$$\begin{pmatrix} \boldsymbol{e}(x_1) \\ \vdots \\ \boldsymbol{e}(x_k) \\ \vdots \\ \boldsymbol{e}(x_M) \end{pmatrix} = \begin{pmatrix} \mathcal{E}_0(x_1) & \cdots & \mathcal{E}_i(x_1) & \cdots & \mathcal{E}_N(x_1) \\ \vdots & \ddots & \vdots & \ddots & \vdots \\ \mathcal{E}_0(x_k) & \cdots & \mathcal{E}_i(x_k) & \cdots & \mathcal{E}_N(x_k) \\ \vdots & \ddots & \vdots & \ddots & \vdots \\ \mathcal{E}_0(x_M) & \cdots & \mathcal{E}_i(x_M) & \cdots & \mathcal{E}_N(x_M) \end{pmatrix} \tag{IV.33}$$

with M>N

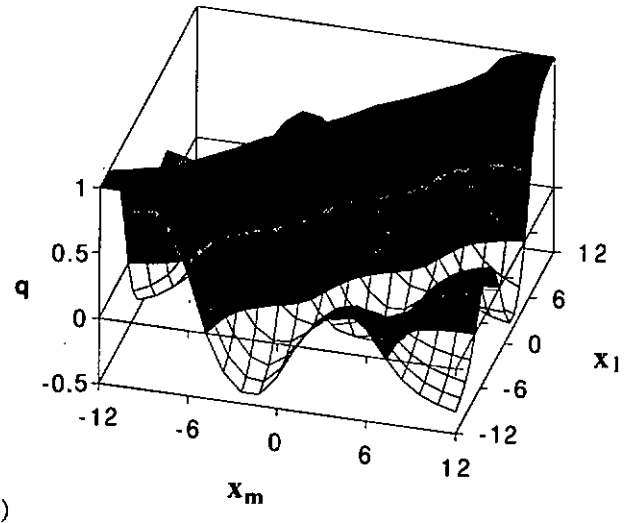

a)

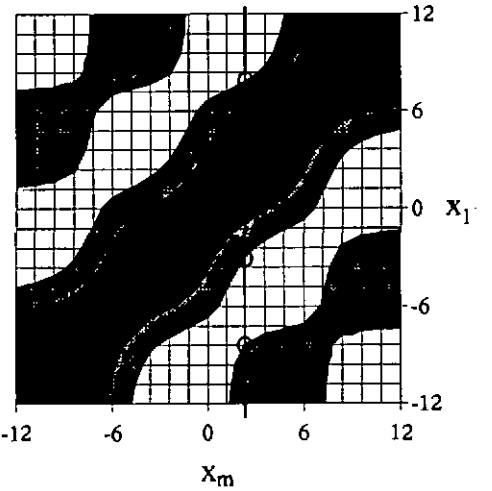

b)

Fig. IV.6 Normalized dot product q of the eigenfield vectors $\mathcal{E}(x_l)$ and $\mathcal{E}(x_m)$ versus the locations x_l and x_m. The function q is shown in a) 3D plot and b) contour plot
Waveguide parameters: width: 24 μm; guide index: 1.5163, substrate index: 1.5151;

Now, assume that the x_k are equally distributed between x_0 and x_M:

$$x_k = x_0 + k\,\frac{x_M - x_0}{M} \tag{IV.34}$$

Multiplying the dot product of column u and column v by $\frac{2\beta_1}{\omega\mu}$ leads to the cross power:

$$\overline{P} = \frac{2\beta_1}{\omega\mu} \sum_{k=0}^{M} \mathcal{E}_u(x_k)\mathcal{E}_v(x_k) \tag{IV.35}$$

If M tends to infinity, the summation must be replaced by an integral. Equation (IV.35) becomes:

$$\overline{P} = \frac{2\beta_1}{\omega\mu} \int_{x_0}^{x_M} \mathcal{E}_u(x)\mathcal{E}_v(x)dx \tag{IV.36}$$

When $x_0 \to -\infty$ and $x_M \to \infty$, we get from the orthogonality of the eigenmodes:

$$\overline{P} = \frac{2\beta_1}{\omega\mu} \int_{-\infty}^{\infty} \mathcal{E}_u(x)\mathcal{E}_v(x)dx = \delta_{uv} \tag{IV.37}$$

We deduce that the matrix (IV.37) has a rank equal to (N+1), in other words, it describes a (N+1)-dimensional space. So, the infinite set of eigenfield vectors $\mathcal{E}(x)$, $-\infty < x < \infty$, forms a finite (N+1)-dimensional space. Then, because rank($\mathbf{M}$)=rank($\mathbf{M}^T$) for any real matrix $\mathbf{M}$ (see for example Section 4.1.10 of [45]), we can find N+1 vectors $\mathcal{E}(x)$ mutually orthogonal.

This can be illustrated by the special case of weakly interacting directional couplers. Let us choose a three-branch coupler with three similar waveguides, as sketched in Fig. IV.7. It is well known that the eigenfields of such structures are approximately given by [46]:

$$\mathcal{E}_0(x) = \tfrac{1}{2}\,\mathcal{E}(x - x_1) + \tfrac{1}{\sqrt{2}}\,\mathcal{E}(x) + \tfrac{1}{2}\,\mathcal{E}(x - x_2) \tag{IV.38a}$$

$$\mathcal{E}_1(x) = \tfrac{1}{\sqrt{2}}\,\mathcal{E}(x - x_1) - \tfrac{1}{\sqrt{2}}\,\mathcal{E}(x - x_2) \tag{IV.38b}$$

$$\mathcal{E}_2(x) = \tfrac{1}{2}\,\mathcal{E}(x - x_1) - \tfrac{1}{\sqrt{2}}\,\mathcal{E}(x) + \tfrac{1}{2}\,\mathcal{E}(x - x_2) \tag{IV.38c}$$

where $\mathcal{E}(x)$ is the eigenfield of a waveguide alone.

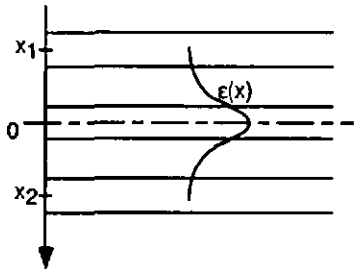

Fig. IV.7 Three branch directional coupler, with similar waveguides

We evaluate $\mathcal{E}_0(x)$, $\mathcal{E}_1(x)$ and $\mathcal{E}_2(x)$ at the points x_1, x=0 and x_2. Reminding that $\mathcal{E}(x_1) \cong \mathcal{E}(x_2) \cong 0$ for weakly coupled waveguides, we find three orthogonal eigenfield vectors $\boldsymbol{e}(x_1)$, $\boldsymbol{e}(x=0)$ and $\boldsymbol{e}(x_2)$, forming the matrix (IV.33):

$$\boldsymbol{e}(x_1) = \left(\tfrac{1}{2}\,\mathcal{E}(0) \quad \tfrac{1}{\sqrt{2}}\,\mathcal{E}(0) \quad \tfrac{1}{2}\,\mathcal{E}(0)\right) \tag{IV.39a}$$

$$\boldsymbol{e}(0) = \left(\tfrac{1}{\sqrt{2}}\,\mathcal{E}(0) \quad 0 \quad -\tfrac{1}{\sqrt{2}}\,\mathcal{E}(0)\right) \tag{IV.39b}$$

$$\boldsymbol{e}(x_2) = \left(\tfrac{1}{2}\,\mathcal{E}(0) \quad -\tfrac{1}{\sqrt{2}}\,\mathcal{E}(0) \quad \tfrac{1}{2}\,\mathcal{E}(0)\right) \tag{IV.39c}$$

This example also shows that other sampling points lead to eigenfield vectors close to one of the vectors (IV.39). As an example, let us take x_3 in the vicinity of x=0: $x_3=\delta x$, for which δx still satisfies the conditions $\mathcal{E}(x_1 + \delta x) \cong \mathcal{E}(x_2 + \delta x) \cong 0$. Then, $\boldsymbol{e}(x_3)$ is given by:

$$\boldsymbol{e}(x_3) = \left(\tfrac{1}{2}\,\mathcal{E}(\delta x) \quad \tfrac{1}{\sqrt{2}}\,\mathcal{E}(\delta x) \quad \tfrac{1}{2}\,\mathcal{E}(\delta x)\right) \tag{IV.40}$$

Obviously, $\boldsymbol{e}(x_1)$ and $\boldsymbol{e}(x_3)$ are collinear. Thus a matrix formed with the row vectors $\boldsymbol{e}(x_0)$, $\boldsymbol{e}(x_1)$, $\boldsymbol{e}(x_2)$ and $\boldsymbol{e}(x_3)$ is ill-conditioned. In this case, the normalized dot product $q(0,x)$ is approximately equal to unity for any point x located in the centre branch of the coupler. So, other sampling points should be chosen in the regions lying between the waveguides, where the function $q(x_m,x_1)$, given by equation (IV.32), is different from 1, -1 or zero.

From this short analysis, we can deduce a rule ensuring a best conditioning of the system of equations (IV.20). Indeed, the output intensity distribution should be sampled with sampling points uniformly distributed from one side of the waveguide structure to the other. In this manner, the full eigenfield vector space is covered, and all sampled eigenfield vectors are not collinear.

Errors

In the present study, we assumed that the eigenfields and the output intensity distribution are known, so that the mode coefficients A_i at the waveguide output can be calculated. The purpose of error analysis in our case should be to determine the effect of various error sources on the computed mode coefficients, i.e. components of the mode coefficient vector **A**. By contrast, numerical mathematics are mostly concemed with vector magnitudes. Therefore, a thorough error analysis of the norm of **A** would bring only little information. So, we limit ourselves to describing the error source appearing in the proposed method. Some numerical indications will be given on this subject in Chapter V, with the help of simulated intensity distributions.

The Output Near-field Intensity Distribution Analysis (ONIDA) presents several sources of errors: the intensity error δS, the eigenfield error $\delta \mathcal{E}_i^0$ and the alignment error δx. Each of them are briefly described hereafter.

The intensity error δS is due to fluctuations of the experimental conditions, including the light source, the in-coupling conditions, the photodetector and the electronic amplifier. We show now that the norm of the mode coefficient vector **A** is independent of the intensity error δS if δS has a normal distribution, i.e. it has a probability function following a Gaussian curve.

From equation (II.25), the guided power, the intensity distribution and the eigenfield coefficients are related by the equation:

$$P = \int_{-\infty}^{\infty} S dx = |\mathbf{A}|^2 \qquad \text{(IV.41)}$$

Then, the intensity distribution is subject to experimental measurement error expressed by δS, yielding a measured intensity $S+\delta S$. This results in a variation δP of the output power and in a variation $\delta|\mathbf{A}|$ of the vector norm. Neglecting second order terms, we derive from (IV.41):

$$\delta P = \int_{-\infty}^{\infty} \delta S dx = 2|\mathbf{A}|\delta|\mathbf{A}| \qquad \text{(IV.42)}$$

Now, the above equation shows that an error δS leads to a variation $\delta|\mathbf{A}|$ of the vector norm if the integral of (IV.42) is different from zero.

However, assuming the error $\delta S$of the intensity distribution follows a normal law, then the integral of (IV.42) vanishes if a least square method is used for calculating the mode coefficient vector **A** (see for example §9.1.22 of [47]). Thus, the norm $|\mathbf{A}|$ is not influenced by errors of the intensity distribution when we use a least square method.

Equation (IV.42) describes the effect of δS on the vector norm. However, this calculation does not allow any conclusion about the change of the elements $\mathbf{A}_i$ of **A**. Though, this effect may be non negligible, as can be illustrated by the following example. Assume that δS is proportional to the eigenfield $\mathscr{E}_1(x)$. In this case, it is easy to see that the integral of equation (IV.42) is equal to zero, hence that the norm of **A** is not affected by δS. However, it is also evident that some elements of **A** will be influenced, in particular $\mathbf{A}_1$. Thus, δS showing a non zero correlation with the eigenfields have a non negligible effect on $\delta \mathbf{A}$.

The effect of intensity measurement errors on the computed coefficient vector **A** will be shown in Chapter V with the help of simulated intensity distributions. The error magnitude are presented for a few typical waveguiding structures.

The eigenfield errors $\delta \mathscr{E}_i$ are caused by errors due to the calculation hypotheses (scalar wave equation, weak guidance hypothesis, effective index method), to errors of the geometrical parameters of the waveguide (width, depth) and to errors of the optical parameters (refractive index values, index distribution). In this case, the errors $\delta \mathscr{E}_i$ are correlated to the eigenfields. Although the effect of these parameters on the retrieved mode coefficient vector **A** could be calculated analytically, it appeared more efficient to give an order of magnitude, using simulated intensity distributions. This numerical analysis is carried out in Section V.2

An alignment error δx appears between the reference system used for the calculations and the one of the measurement. This results from the absence of mechanical reference in the ion-exchanged waveguide. So, the x-axis reference is chosen arbitrarily. This situation is sketched in Fig. IV.8.

In order to align both reference systems, we define and compare two alignment procedures in Section V.2. Both methods make use of the measured output intensity distribution. Nevertheless, the alignment accuracy is necessarily limited. Thus, the effect of this alignment error δx

on the calculation of **A** will be estimated numerically in paragraph V.1.4 for a few typical cases.

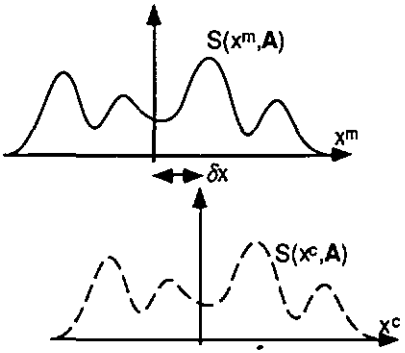

Fig. IV.8 Calculated intensity distribution $S(x^c,\mathbf{A})$ and measured intensity distribution $S(x^m)$ with their reference systems x^c of the calculation and x^m of the experiment

IV.3.3 Algorithm retrieving mode coefficients from an intensity distribution

Overview

As was shown in Section IV.1, the amplitudes of the excitation mode coefficients $\mathbf{A}^e$ can be easily calculated from the light injection conditions. Propagation in the waveguide modifies these amplitudes, due to propagation loss and mode coupling. Nevertheless, both effects are usually small, so that we will consider that the excitation amplitudes $|A_i^e|$ form a good approximation of the output mode coefficient amplitudes $|A_i|$.

Based on this remark, the search strategy of the Mode Coefficient Retrieving (MCR) algorithm consists first in optimizing only the phases of the components A_i, keeping the amplitudes constant. In the second step, the amplitudes only are tuned, leaving the mode coefficient phases unchanged. Finally, both amplitudes and phases are optimized, until stop conditions are fulfilled. According to this, the MCR algorithm is given by the flow chart depicted in Fig. IV.9.

The optimization is performed by the algorithm proposed by Broyden, Fletcher, Goldfarb and Shanno, and known as the BFGS algorithm with line search [48]. To determine the direction of search, this algorithm

requires the calculation of the first derivatives of the function to be optimized, the squared error sum f(**A**) in our case, and of an approximation of its Hessian. At each step of the iteration, the Hessian is updated. These conditions explain the effectiveness of this method.

As the amplitudes and phases are optimized separately, the standard BFGS algorithm was slightly modified. Furthermore, two distinct stop conditions, for amplitudes and phases respectively, are introduced. Thus, some mathematical developments are given in the following paragraph.

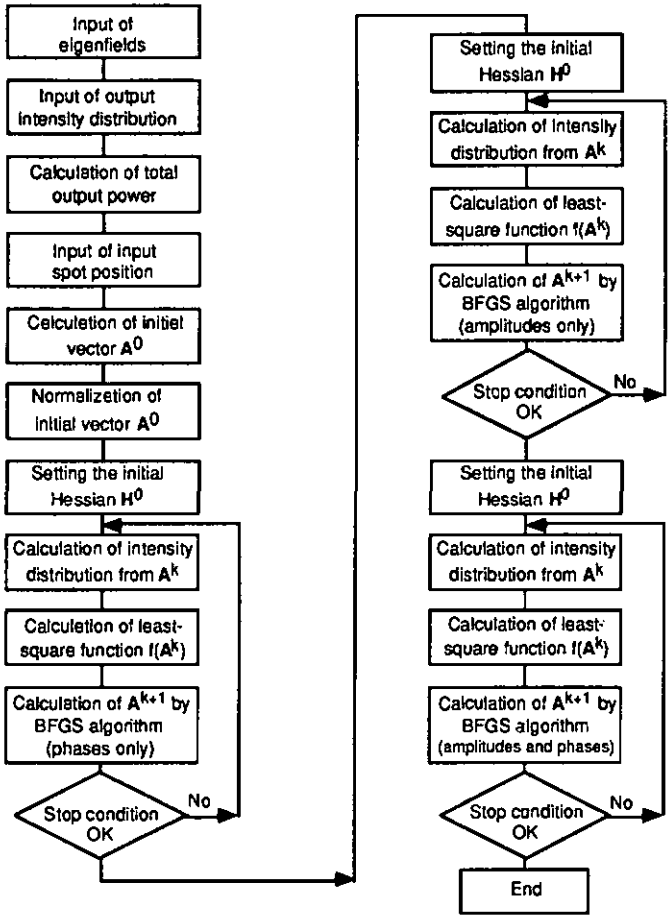

Fig. IV.9 General flow chart of the Mode Coefficient Retrieving (MCR) algorithm

The BFGS algorithm

For optimizing the phases and amplitudes separately, the squared error sum f(**A**) given by (IV.21) is rewritten in the form of a function of the real amplitudes a_i and phases φ_i:

$$f(\mathbf{A}) = f(A(\varphi_i, a_i)) = f(\Phi) \qquad i=0, 1, N \tag{IV.43}$$

where $\Phi^T = (\varphi_1 \cdots \varphi_N \,|\, a_0 \cdots a_N)$ is the parameter vector
φ_i is the phase of the ith eigenmode and
a_i its amplitude

A polynomial approximation of f(Φ), truncated to the quadratic term, is given by:

$$f(\Phi^{(k)} + \delta) \approx f(\Phi^{(k)}) + \mathbf{g}(\Phi^{(k)})^T \delta + \tfrac{1}{2} \delta^T \mathbf{G}(\Phi^{(k)}) \delta \tag{IV.44}$$

where $\mathbf{g}^T = (\partial f/\partial\varphi_1, \cdots, \partial f/\partial\varphi_N, | \partial f/\partial a_0, \cdots, \partial f/\partial a_N)$ is the gradient of f(Φ) at point $f(\Phi^{(k)})$ and $\mathbf{G}(\Phi^{(k)})$ its Hessian. The notation is simplified in the following way:

$$\mathbf{g}(\Phi^{(k)}) = \mathbf{g}^{(k)} \quad \text{and} \quad \mathbf{G}(\Phi^{(k)}) = \mathbf{G}^{(k)} \tag{IV.45}$$

With this, the Hessian is given by:

$$\mathbf{G}^{(k)} = \left(\begin{array}{c|c} \mathbf{G}_{\varphi\varphi}^{(k)} & \mathbf{G}_{\varphi a}^{(k)} \\ \hline \mathbf{G}_{a\varphi}^{(k)} & \mathbf{G}_{aa}^{(k)} \end{array}\right) \tag{IV.46}$$

where the submatrices $\mathbf{G}_{\varphi\varphi}$, $\mathbf{G}_{\varphi a}$, $\mathbf{G}_{a\varphi}$ and $\mathbf{G}_{aa}$ are expressed at point $\Phi^{(k)}$ by:

$$\mathbf{G}_{\varphi\varphi} = \begin{pmatrix} \frac{\partial^2 f}{\partial \varphi_1^2} & \cdots & \frac{\partial^2 f}{\partial \varphi_1 \partial \varphi_N} \\ \vdots & \ddots & \vdots \\ \frac{\partial^2 f}{\partial \varphi_N \partial \varphi_1} & \cdots & \frac{\partial^2 f}{\partial \varphi_N^2} \end{pmatrix} \tag{IV.47a}$$

$$\mathbf{G}_{aa} = \begin{pmatrix} \frac{\partial^2 f}{\partial a_0^2} & \cdots & \frac{\partial^2 f}{\partial a_0 \partial a_N} \\ \vdots & \ddots & \vdots \\ \frac{\partial^2 f}{\partial a_N \partial a_0} & \cdots & \frac{\partial^2 f}{\partial a_N^2} \end{pmatrix} \tag{IV.47b}$$

$$\mathbf{G}_{\varphi a} = (\mathbf{G}_{a\varphi})^T \approx \begin{pmatrix} \frac{\partial^2 f}{\partial \varphi_1 \partial a_0} & \cdots & \frac{\partial^2 f}{\partial \varphi_1 \partial a_N} \\ \vdots & \ddots & \vdots \\ \frac{\partial^2 f}{\partial \varphi_N \partial a_0} & \cdots & \frac{\partial^2 f}{\partial \varphi_N \partial a_N} \end{pmatrix} \qquad \text{(IV.47c)}$$

Note that the parameter vector Φ and the gradient $\mathbf{g}$ have the dimension (2N+1), and the Hessian $\mathbf{G}$ the dimension (2N+1)x(2N+1).

At a minimum Φ_s, all components of the squared error sum $f(\Phi_s)$ gradient $\mathbf{g}(\Phi_s)$ are equal to zero. Furthermore, the Hessian $\mathbf{G}(\Phi_s)$ is positive definite. Thus we look for a point $\Phi_s=\Phi^{(k)}+\mathbf{s}$ for which the gradient is equal to zero:

$$\mathbf{g}(\Phi^{(k)} + \mathbf{s}) \approx \mathbf{g}^{(k)} + \mathbf{G}^{(k)}\mathbf{s} = 0 \qquad \text{(IV.48)}$$

This suggests that the minimum Φ_s has to be found in the direction given by:

$$\mathbf{s}^{(k)} = -\mathbf{G}^{(k)^{-1}}\mathbf{g}^{(k)} \approx -\mathbf{H}^{(k)}\mathbf{g}^{(k)} \qquad \text{(IV.49)}$$

where $\mathbf{H}^{(k)} \approx \mathbf{G}^{(k)^{-1}}$ is an approximation of the inverse of $\mathbf{G}^{(k)}$.

Thus the algorithm follows the sequence given below for the kth step:

a) set $\mathbf{s}^{(k)} = -\mathbf{H}^{(k)}\mathbf{g}^{(k)}$

b) search a minimum along $\mathbf{s}^{(k)}$ giving $\Phi^{(k+1)} = \Phi^{(k)} + \alpha^{(k)}\mathbf{s}^{(k)}$

c) evaluate $\mathbf{H}^{(k+1)}$ from $\mathbf{H}^{(k)}$

It must be noted that this algorithm requires the calculation of the gradient $\mathbf{g}^{(k)}$ at each iteration step. The detailed calculation of $\mathbf{g}^{(k)}$ is given in Appendix A1. The Hessian is updated at each step so that the update $\mathbf{H}^{(k)}$ satisfies:

$$\mathbf{H}^{(k+1)}\gamma^{(k)} = \delta^{(k)} \qquad \text{(IV.50)}$$

This is usually called the quasi-Newton condition.

Several formulas have been proposed for updating $\mathbf{H}^{(k+1)}$. The BFGS algorithm sets [48]:

$$\mathbf{H}^{(k+1)} = \mathbf{H} + \left(1 + \frac{\gamma^T\mathbf{H}\gamma}{\delta^T\gamma}\right)\frac{\delta\delta^T}{\delta^T\gamma} - \left(\frac{\delta\gamma^T\mathbf{H} + \mathbf{H}\gamma\delta^T}{\delta^T\gamma}\right) \qquad \text{(IV.51)}$$

where

$$\delta^{(k)} = \Phi^{(k+1)} - \Phi^{(k)} = \alpha^{(k)}\mathbf{s}^{(k)} \text{ and} \qquad \text{(IV.52)}$$

$$\gamma^{(k)} = \mathbf{g}^{(k+1)} - \mathbf{g}^{(k)} \qquad \text{(IV.53)}$$

Note that the superscript (k) is omitted in the right side of (IV.51).

An important property of (IV.51) is that it preserves positive definite matrices $\mathbf{H}^{(k)}$. This ensures the descent property of the algorithm, which was shown to work well in practice [48]. For this BFGS algorithm, the global convergence has been proved for strictly convex functions, even in the case of inexact line search. Thus this method is theoretically safer than other quasi-Newton algorithms, for which this demonstration is not yet given.

In paragraph IV.3.3., we stated that the optimization has to be performed first with the phases, keeping the amplitudes constant. This can be merely achieved by a proper choice of the initial matrix $\mathbf{H}^{(0)}$. Assume the component Φ_m of the parameter vector Φ must be kept constant. Then, the mth row of the initial matrix $\mathbf{H}^{(0)}$ must be made of zeros: $H^{(0)}_{mi} = 0 \ \forall i = 0, 1, \ldots, 2N$. Then, it can be shown (see Appendix A2) that $\Phi_m^{(k)}$ is kept constant at each iteration k, i.e. $\Phi_m^{(k+1)} = \Phi_m^{(k)} \ \forall k$.

So, writing $\mathbf{H}^{(k)}$ in the partitioned form:

$$\mathbf{H}^{(k)} = \left(\begin{array}{c|c} \mathbf{H}^{(k)}_{\varphi\varphi} & \mathbf{H}^{(k)}_{\varphi a} \\ \hline \mathbf{H}^{(k)}_{a\varphi} & \mathbf{H}^{(k)}_{aa} \end{array}\right) \qquad \text{(IV.54)}$$

the optimization of the phases only is obtained by choosing the initial matrix $\mathbf{H}^{(0)}$:

$$\mathbf{H}^{(0)}_{\varphi\varphi} = \mathbf{I} \text{ and} \qquad \text{(IV.55a)}$$

$$\mathbf{H}^{(0)}_{\varphi a} = \mathbf{H}^{(0)}_{a\varphi} = \mathbf{H}^{(0)}_{aa} = \mathbf{0} \qquad \text{(IV.55b)}$$

where $\mathbf{I}$ is the unity matrix: $\mathbf{I} = \begin{pmatrix} 1 & & \mathbf{0} \\ & \ddots & \\ \mathbf{0} & & 1 \end{pmatrix}$

In the second part of the MCR algorithm, with optimization of the amplitudes only, the initial matrix $\mathbf{H}^{(0)}$ is set to:

$$\mathbf{H}_{aa}^{(0)} = \mathbf{I} \text{ and} \tag{IV.56a}$$

$$\mathbf{H}_{\varphi\varphi}^{(0)} = \mathbf{H}_{\varphi a}^{(0)} = \mathbf{H}_{a\varphi}^{(0)} = \mathbf{0} \tag{IV.56b}$$

Finally, the last part of the MCR algorithm optimizes both phases and amplitudes. This is obtained with the matrix $\mathbf{H}^{(0)}$ initialized to:

$$\mathbf{H}_{\varphi\varphi}^{(0)} = \mathbf{H}_{aa}^{(0)} = \mathbf{I} \tag{IV.57a}$$

$$\mathbf{H}_{\varphi a}^{(0)} = \mathbf{H}_{a\varphi}^{(0)} = \mathbf{0} \tag{IV.57b}$$

Note that the choice of an initial matrix equal to unity results in the search along the steepest decay of the function f(**A**).

Line search

The algorithm chosen for the line search is given in [48]. The condition used to exclude the right-hand extreme is:

$$f^{(k)} - f^{(k+1)} \geq -\sigma \mathbf{g}^{(k)^T} \delta^{(k)} \tag{IV.58}$$

The condition to exclude the left-hand side was chosen to be:

$$\left| \mathbf{g}^{(k+1)^T} \mathbf{s}^{(k)} \right| \leq -\sigma \mathbf{g}^{(k)^T} \mathbf{s}^{(k)} \tag{IV.59}$$

In both conditions, the parameter σ designates the search accuracy along the line $\mathbf{s}^{(k)}$. For instance, σ=0.9 is a very weak line search, whereas σ=0.1 leads to a fairly accurate minimum.

Since convergence of the BFGS update formula has been proved in the case of inexact line search, a value of 0.1 was chosen for σ. This insures a good accuracy and a reasonable computing effort at the same time [48].

Convergence test

The choice of a proper convergence test is of importance. If not appropriate, the algorithm may stop far from the solution, or run for many steps without significant increase of the accuracy.

The convergence tests based on

$$\left| \Phi_i^{(k)} - \Phi_i^{(k+1)} \right| \leq \varepsilon \tag{IV.60}$$

or

$$f^{(k)} - f^{(k+1)} \leq \varepsilon \tag{IV.61}$$

apply well for algorithms with a high convergence rate [48]. However, in our case, the convergence rate is slow. Therefore we chose the test recommended by Fletscher [48], but we applied it to the phases and to the amplitudes separately, i.e.:

$$\left\| g_{\varphi}^{(k)} \right\| \leq \varepsilon_{\varphi} \quad \text{and} \quad \left\| g_{a}^{(k)} \right\| \leq \varepsilon_{a} \qquad \text{(IV.62a)(IV.62b)}$$

The question is now to find ε_{φ} and ε_{a} in such a way that these tests are invariant with the power carried by the waveguide. For this, we replace $\mathbf{A}$ by $\tau\mathbf{A}$ in equation (II.25), leading to:

$$P_o(\tau\mathbf{A}) = \sum_{i=0}^{N} \tau A_i (\tau A_i)^* = \tau^2 P_o(\mathbf{A}) \qquad \text{(IV.63)}$$

with P_o is the total output power and
τ is a real constant

We substitute now $\tau\mathbf{A}$ for $\mathbf{A}$ in the derivative given by equation (A1.2) of Appendix A1 and we get for the gradient vector $\mathbf{g}_{\varphi}(\tau\mathbf{A})$:

$$\mathbf{g}_{\varphi}(\tau\mathbf{A}) = \tau^4 \mathbf{g}_{\varphi}(\mathbf{A}) \qquad \text{(IV.64)}$$

Therefore, we must choose for ε_{φ}:

$$\varepsilon_{\varphi} = \sigma_{\varphi} P_o^2(\tau\mathbf{A}) = \sigma_{\varphi} \tau^4 P_o^2(\mathbf{A}) \qquad \text{(IV.65)}$$

where σ_{φ} is an arbitrarily small value

With (IV.64) and (IV.65), equation (IV.62a) becomes:

$$\frac{\left\| \mathbf{g}_{\varphi}(\tau\mathbf{A}) \right\|}{P_{tot}^2(\tau\mathbf{A})} = \frac{\left\| \mathbf{g}_{\varphi}(\mathbf{A}) \right\|}{P_{tot}^2(\mathbf{A})} \leq \sigma_{\varphi} \qquad \text{(IV.66)}$$

Similarly, we have for the amplitudes:

$$\mathbf{g}_a(\tau\mathbf{A}) = \tau^3 \mathbf{g}_a(\mathbf{A}) \qquad \text{(IV.67)}$$

In this case, we will choose for ε_a:

$$\varepsilon_a = \sigma_a P_o^{3/2}(\tau\mathbf{A}) = \sigma_a \tau^3 P_o^{3/2}(\mathbf{A}) \qquad \text{(IV.68)}$$

and we obtain:

$$\frac{\|g_a(\tau A)\|}{P_{tot}^{3/2}(\tau A)} = \frac{\|g_a(A)\|}{P_{tot}^{3/2}(A)} \leq \sigma_a \qquad \text{(IV.69)}$$

The tests (IV.66) and (IV.69) are applied in the MCR algorithm.

Normalization of the initial vector

Before the algorithm begins the search of a minimum, the amplitudes $a_i^0 = |A_i^0|$ of the initial vector are normalized to the total output power P_o, using equation (II.25):

$$P_o = \sum_{i=0}^{N} (a_i^0)^2 \equiv \sum_{k=0}^{M} S(x_k) \qquad \text{(IV.70)}$$

where N is the number of guided modes and
M the number of sampling points

This normalization is applied in any case, independently of the choice of the initial vector $\mathbf{A}^0$.

IV.4. CALCULATION OF INTER-MODE EFFECTIVE INDEX DIFFERENCES

For calculating the effective index differences, one has to determine the optical phase differences introduced by propagation in the waveguide structure. When this is done, the effective index differences are given by the simple relation:

$$\Delta\varphi_i' = \varphi_i' - \varphi_0' = k_0 \Delta n_i L \qquad \text{(IV.71)}$$

where $\Delta n_i = n_0 - n_i$ are the effective index differences and
φ_i' are the optical phases brought by propagation

However, the optical phase differences are not directly given by the mode coefficient vector retrieved by the MCR algorithm. Indeed, assuming $\mathbf{A}_s = (A_{s0}, A_{s1}, \ldots, A_{sN})$ leads to the intensity distribution $S(x,\mathbf{A}_s)$, paragraph IV.3.1 pointed out that

a) $\mathbf{A}_s e^{j\varphi}$

b) the complex conjugate $\mathbf{A}_s^*$ and

c) $\mathbf{A}_s^p = (A_{s0}, A_{s1}e^{-j2m_1\pi}, \ldots, A_{sN}e^{-j2m_N\pi})$

yield the same intensity distribution. Solutions given by a) can be fixed by setting the optical phase of the fundamental mode to 0, with the consequence that only effective index differences can be calculated. Nevertheless, we still have to choose one of the solutions given by b) or c). Furthermore, a 0 or π phase due to the excitation mode coefficient is also included in the mode coefficient retrieved by the MCR algorithm. Therefore, deriving the optical phase differences from the retrieved mode coefficients also requires a correction for the excitation conditions.

In this Section, we present some criteria leading to the choice of the appropriate mode coefficients, regarding the possible solutions b) and c), as well the correction for the excitation mode coefficients. This is carried out in relation with the experimental conditions. Therefore, we give next some hints for setting experimental parameters facilitating the choice of a solution.

IV.4.1 Retrieving optical phase differences

Correction for periodicity

The optical phase differences brought by propagation in the waveguide structure are given by relation (IV.71). Obviously, the $\Delta\varphi_i^c$ can be greater than 2π for a sufficiently long waveguide. This situation is experimentally very common. However, the mode coefficient phases φ_i^r retrieved by the MCR algorithm lie in the range $0 \leq \varphi_i^r < 2\pi$, because of the periodicity of complex values.

This ambiguity can be removed by the following observation. The effective index differences increase for increasing mode order. Thus the phase differences meet the relation:

$$\Delta\varphi_i > \Delta\varphi_{i-1} \qquad \text{(IV.72)}$$

Thus we have to find an integer m_i satisfying:

$$\Delta\varphi_i^{\wedge} = \Delta\varphi_i^r + 2m_i\pi > \Delta\varphi_{i-1}^{\wedge} \qquad \text{(IV.73)}$$

with $\Delta\varphi_i^{\wedge}$ the optical phase difference of mode i due to propagation

$\Delta\varphi_i^r$ the optical phase difference retrieved by the MCR algorithm

In addition, the choice of an integer m_i is facilitated by comparing the propagation phase differences $\{\Delta\varphi_i^{\wedge}\}$ with the phase differences $\{\Delta\varphi_i^{c}\}$ calculated from equation (IV.71) and the theoretical effective indices (see later in this paragraph).

Correction for complex conjugation

A criterion for choosing the retrieved mode coefficient vector or its complex conjugate is given by an observation concerning the phase difference between two successive modes. It is based on the fact that the refractive index difference between consecutive guided modes increases with mode order. In a large multimode waveguide, for instance, the effective indices are approximately given by [20]:

$$n_i \cong n_0 - \Delta n(i^2 - 2i) \qquad \text{(IV.74)}$$

where Δn is a constant given by the waveguide structure

With this relation, we can deduce the phase difference between two consecutive modes:

$$\varphi_{i+1} - \varphi_i = k_0 L \Delta n(2i + 3) \qquad \text{(IV.75)}$$

where φ_i are the phases of the mode coefficients A_i

Therefore, it follows that the phase difference increases with increasing mode order. We show now that the opposite happens for the complex conjugate.

The phases φ_i^{cc} of the complex conjugate coefficients are given by: $\varphi_i^{cc} = -\varphi_i$. We now apply the periodicity correction so that the phases φ_i^{cc} are positive and form an increasing series. This is achieved by setting:

$$\varphi_i^{cc} = 2\pi(n + i) - \varphi_i \qquad \text{(IV.76)}$$

where n is a integer constant such that all phases φ_i^{cc} are positive. With that, the phase difference between successive modes is given by:

$$\varphi_{i+1}^{cc} - \varphi_i^{cc} = 2\pi - (\varphi_{i+1} - \varphi_i) \qquad \text{(IV.77)}$$

We remind that the phase difference φ_{i+1}-φ_i increases with increasing mode order. Therefore, we deduce from (IV.77) that the phase

difference $\varphi_{i+1}^{cc} - \varphi_i^{cc}$ decreases with the mode order in the case of complex conjugate coefficient vector.

So, after applying the periodicity corrections to the retrieved coefficient vector $\mathbf{A}^r$, one calculates the phase difference between successive modes. If these differences form an increasing serie, then the retrieved coefficient vector must be chosen, otherwise, its complex conjugate $(\mathbf{A}^r)^*$ must be retained. However, this condition holds if the effective index differences increase with mode order, which is not the case of all waveguiding structures. In particular, three-branch directional couplers with unequal waveguide widths do not present this property in all conditions. In such a case, the comparison with the theoretical phases should lead to the correct choice of the retrieved mode coefficient vector or of its complex conjugate (see later in this paragraph).

Correction for injection conditions

It was pointed out in Section IV.2 that the injection conditions have a 0 or π contribution to the phases of the retrieved mode coefficients, namely:

$$A_i^r = A_i^e \, e^{j\Delta\varphi_i^A} \qquad \text{(IV.78)}$$

with A_i^e the excitation mode coefficient
$\Delta\varphi_i^A$ the phase differences brought by propagation

This contribution of the excitation mode coefficient can be easily calculated from the position x_0 of the input light source. Thus, this ambiguity should be removed without difficulty.

However, the situation is not so clear in experimental conditions. In this case, the position x_0 is known with a limited accuracy. Therefore it is not always easy to distinguish if the actual light source position leads to a positive or negative eigenfield value, thus to a 0 or π phase contribution. Nevertheless, this ambiguity appears when the light source is located near a zero crossing of the eigenfield, i.e. when the amplitude of the mode coefficient is close to zero. In such a condition, the choice of a 0 or π value can be performed by comparing the mode coefficient phase with its theoretical value, as shown below.

Comparison with theoretical phases

Since the refractive index profile is known, the theoretical effective indices n_i can be computed. Then, the phase differences due to propagation

are given by (IV.71):

$$\Delta\varphi_i^{\nwarrow} = \varphi_i^{\nwarrow} - \varphi_0^{\nwarrow} = k_0 \Delta n_i L \qquad \text{(IV.79)}$$

where $\Delta n_i = n_0 - n_i$ are the effective index differences and
$\varphi_i^{\nwarrow}$ are the optical phases brought by propagation

Comparing the retrieved phase differences to their theoretical counterparts helps the choice of a correct mode coefficient vector. However, this method relates the mode coefficient vector to theoretical conditions. Therefore, it can lead to the choice a coefficient vector inconsistent with the experimental conditions. Thus, it should be used as a confirmation, when the other criteria have already been applied.

IV.4.2 Influence of propagation length on determination of modal phases

In fact, most of the experimental conditions are given and cannot be influenced. This is in particular the case of the fabrication technology, which gives the refractive indices and profiles. Furthermore, the function requested from a device implies a given type of structure and a given operating wavelength. The most convenient free parameter of an integrated optic device is its length. We give now some hints conceming the choice of a waveguide length, in particular its influence on the operation of the MCR algorithm.

The best operation of the MCR algorithm is obtained when the device length satisfies the condition:

$$\Delta\varphi_i = k_0(\beta_0 - \beta_i)L < 2\pi \qquad \forall i = 0, 1, \ldots N \qquad \text{(IV.80)}$$

where $\Delta\varphi_i$ is the phase of mode i relatively to mode 0 and
L the length of the device.

With this, the correction for periodicity is useless and the correction for complex conjugation is unambiguous. Unfortunately, this condition is not always realistic from an experimental point of view. Indeed, the propagation length needed for fulfilling this condition is sometimes too short to be achieved experimentally.

A less restrictive condition is then given by:

$$\Delta\varphi_1 = k_0(\beta_0 - \beta_1)L < \pi \qquad \text{(IV.81)}$$

In this case, no ambiguity for the complex conjugation correction is possible: if $\Delta\varphi_1$ fulfils (IV.81), then the phase $\Delta\varphi_1^{cc} = 2\pi - \Delta\varphi_1$ of the complex conjugate is greater than π and so does not meet condition (IV.81) anymore. Nevertheless, the periodicity of the other phases must be now taken into account.

However, it is not always possible to satisfy condition (IV.81). For that reason, we give an even more tolerant condition:

$$\Delta\varphi_1 = k_0(\beta_0 - \beta_1)L < 2\pi \qquad \text{(IV.82)}$$

In such a case, the complex conjugate of the retrieved mode coefficient vector also fulfils condition (IV.82), by contrast to the previous cases. Thus, this situation may be cumbersome to retrieve the phase differences introduced by propagation. Nevertheless, the criteria presented in the preceeding paragraph give useful hints for determining the effective index differences.

Conclusion

As it can be seen from the preceeding paragraphs, retrieving the optical phase differences brought by propagation involves a certain knowledge of the studied structures. This also requires some experience from the researcher, together with proper experimental conditions.

However, these procedures can be applied effectively, and the choice of the right solution can be made with some confidence. This will be illustrated in the next chapter for the case of a few structures, first from simulated data (Section V.1), second from experimental situations (Section V.2).

CHAPTER V

DEMONSTRATION OF THE ONIDA METHOD

In this chapter, the effectiveness of the Output Near-field Intensity Distribution Analysis (ONIDA) is first demonstrated with simulated data. For this purpose, an intensity distribution is computed from a known complex coefficient vector $\mathbf{A}^g$. Then, these simulated data are introduced into the Mode Coefficient Retrieving (MCR) algorithm, which retrieves a mode coefficient vector $\mathbf{A}^r$. This solution can be compared to the known vector $\mathbf{A}^g$. By this procedure, we next estimate the accuracy of the ONIDA method in the presence of various error sources. We also examine the possible existence of local minima or other solutions. Finally, the algorithm robustness is evaluated for different initial vectors used at the first iteration of the algorithm. Then the method is tested with experimental intensity distributions, measured in the case of typical waveguide structures, made up of slightly multimode sections realized by the ion-exchange technology in glass.

V.1. DEMONSTRATION WITH SIMULATED DATA

V.1.1. Working examples of practical structures

In the examples presented below, we choose a given waveguide structure, for which the eigenfields and the propagation constants are calculated. Then we compute a complex coefficient vector defined by:

$$\mathbf{A}^g = (a_0^g \quad a_1^g e^{\varphi_1^g} \quad \cdots \quad a_N^g e^{\varphi_N^g})^T \tag{V.1}$$

The moduli a_i^g of its components are calculated by the overlap integral of equation (IV.5), assuming a Dirac distribution of the field at the waveguide input. The corresponding phases φ_i^g due to propagation through the waveguide are derived from:

$$\varphi_i^g = k_0 n_i L \tag{V.2}$$

where the effective indices n_i are computed from the given structure and L is the assumed propagation distance. Therefore, the given coefficient vector $\mathbf{A}^g$ takes into account the injection as well as the propagation conditions.

From the given coefficient vector $\mathbf{A}^g$ and the eigenfields of the structure, the simulated output intensity distribution can be calculated, then introduced into the MRC algorithm, which retrieves a mode coefficient vector $\mathbf{A}^r$. If the algorithm works well, we should obtain: $\mathbf{A}^r=\mathbf{A}^g$. This process is sketched in the flow chart of Fig. V.1.

As mentioned in Chapter IV, the MRC algorithm requires an initial coefficient vector for the first iteration: the initial vector $\mathbf{A}^0$. This vector is chosen in the following way: the coefficient amplitudes a_i^0 are calculated from the excitation conditions at the input of the waveguide by the overlap integral of equation (IV.5). Hence we have:

$$a_i^0 = a_i^g \qquad \forall i = 0, 1, \cdots, N \tag{V.3}$$

Furthermore, all phase differences φ_i^0 are set to zero, except that of mode 1, which is equal to the value given by the excitation conditions and the propagation (equation V.2), namely:

$$\varphi_1^0 = \varphi_1^g \tag{V.4}$$

This testing process with simulated intensity distribution is summarized in Fig. V.1. in the form of a flow chart.

In order to compare the squared error sum for intensity distributions of differing powers, we further define the normalized squared error sum $f^n(\mathbf{A})$ by:

$$f^n(\mathbf{A}) = \frac{f(\mathbf{A})}{P_0^2} \tag{V.5}$$

where $f(\mathbf{A})$ is the squared error sum given by (IV.21) and
P_0 is the total output power given by (II.25).

We study now three structures commonly used for integrated optic components.

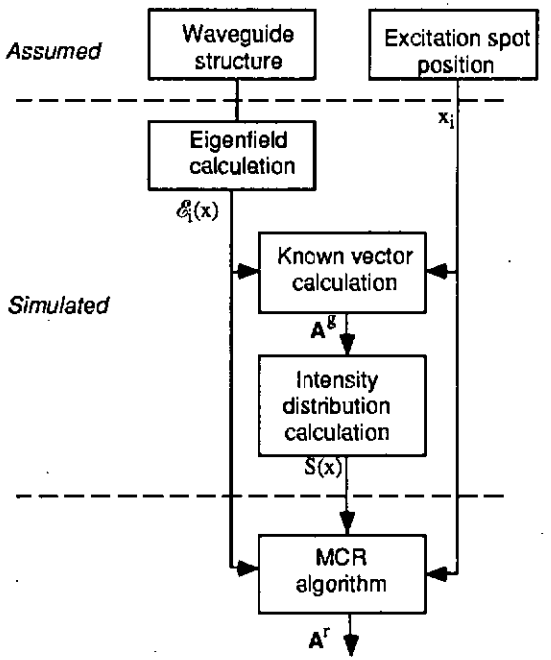

Fig. V.1 Flow chart of the process used for testing the Mode Coefficient Retrieving (MCR) algorithm with simulated output intensity distributions

Three-branch directional coupler

The optogeometrical parameters of the three-branch directional coupler are shown in Fig. V.2. They are close to the parameters used in the experiments with similar structures.

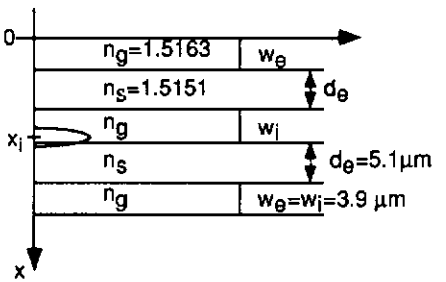

Fig. V.2 Three-branch directional coupler used for the simulations

The given coefficient vector $\mathbf{A}^g$ is calculated from the input spot positions x_i and the propagation length L=4 mm. Table V.1 below shows the given and retrieved mode coefficients.

Pos. x_i	Given coefficients $A_i^g = a_i^g e^{\varphi_i^g}$				Retrieved coefficients $A_i^r = a_i^r e^{\varphi_i^r}$				Propag. phases
1.95	a_0^g	0.240			a_0^r	0.240			
	a_1^g	0.345	φ_1^g	105.0	a_1^r	0.345	φ_1^r	105.0	105.0
	a_2^g	0.251	φ_2^g	234.4	a_2^r	0.251	φ_2^r	234.4	234.4
10.95	a_0^g	0.340			a_0^r	0.340			
	a_1^g	0.000	φ_1^g	105.0	a_1^r	0.0	φ_1^r	0.0	
	a_2^g	-0.355	φ_2^g	234.4	a_2^r	0.355	φ_2^r	54.4	234.4[1)]

Table V.1 Given and retrieved coefficients in the case of the three-branch coupler sketched in Fig. V.1. Propagation length: 4 mm;
Note 1: with correction for the injection conditions (paragraph IV.4.1)

The number of iterations necessary to retrieve the coefficient vector $\mathbf{A}^r$ was smaller than 50. In Table V.1, the phases brought by propagation are obtained after correction due to the negative sign of the eigenfield (paragraph IV.4.1) when the input spot is located in the central waveguide (x_i=10.95 µm). As can be seen, the MCR algorithm recovers the original amplitudes and phases, with a fairly good accuracy in this simple case.

Four-branch directional coupler

Now, we apply the MRC algorithm in a slightly more complicated case: a four-branch directional coupler. The structure and its optogeometrical parameters are sketched in Fig. V.3.

Similarly to the previous case, the amplitudes of the given coefficient vector $\mathbf{A}^g$ are calculated from the input spot positions x_i, and its phases are computed from the effective indices and the propagation length of the chosen structure. Table V.2 summarizes the given and retrieved mode coefficients for four positions x_i of the input light source.

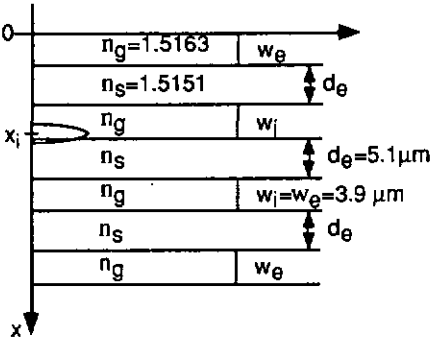

Fig. V.3 Four-branch directional coupler; propagation length: L=4 mm

Here again, the MCR algorithm retrieves the given amplitudes and phases. After correction for negative sign of the eigenfield (paragraph IV.4.1), the phases accumulated by propagation were also retrieved. The given and retrieved intensity distributions are depicted in Fig. V.4 for the x_i=10.95 µm position of the excitation light spot, i.e. in an inner branch of the coupler. Since the MRC algorithm recovered the given vector $\mathbf{A}^g$, the given and retrieved intensity distributions perfectly match in this case. This is confirmed by the normalized squared error sum $f^n(\mathbf{A})$, lower than 10^{-7} in this case.

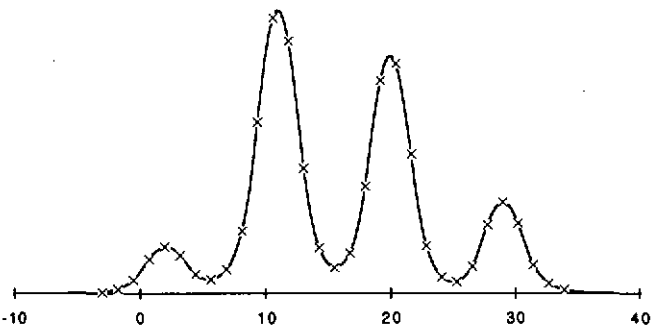

Fig. V.4 Given (crosses) and retrieved (solid line) intensity distributions in the four-branch coupler shown in Fig. V.3, for the position x_i=10.95 µm, i.e. in one of the inner branch

Pos. x_i	Given coefficients $A_i^g = a_i^g e^{\varphi_i^g}$				Retrieved coefficients $A_i^r = a_i^r e^{\varphi_i^r}$				Propag. phases
1.95	a_0^g	0.178			a_0^r	0.178			
	a_1^g	0.291	φ_1^g	70.4	a_1^r	0.291	φ_1^r	70.4	70.4
	a_2^g	0.297	φ_2^g	171.4	a_2^r	0.297	φ_2^r	171.4	171.4
	a_3^g	0.188	φ_3^g	269.7	a_3^r	0.188	φ_3^r	269.7	269.7
10.95	a_0^g	0.288			a_0^r	0.288			
	a_1^g	0.180	φ_1^g	70.4	a_1^r	0.180	φ_1^r	70.5	70.5
	a_2^g	-0.183	φ_2^g	171.4	a_2^r	0.183	φ_2^r	351.4	171.4[1)]
	a_3^g	-0.304	φ_3^g	269.7	a_3^r	0.304	φ_3^r	89.7	269.7[1)]
19.95	a_0^g	0.288			a_0	0.288			
	a_1^g	-0.180	φ_1^g	70.4	a_1	0.180	φ_1^r	250.5	70.5[1)]
	a_2^g	-0.183	φ_2^g	171.4	a_2	0.183	φ_2^r	351.4	171.4[1)]
	a_3^g	0.304	φ_3^g	269.7	a_3	0.304	φ_3^r	269.7	269.7
28.95	a_0^g	0.178			a_0	0.178			
	a_1^g	-0.291	φ_1^g	70.4	a_1	0.291	φ_1^r	250.4	70.5[1)]
	a_2^g	0.297	φ_2^g	171.4	a_2	0.297	φ_2^r	171.4	171.4
	a_3^g	-0.188	φ_3^g	269.7	a_3	0.188	φ_3^r	89.7	269.7[1)]

Table V.2 Given and retrieved coefficients in the case of the four-branch coupler sketched in Fig. V.3. Propagation length: 4 mm;
Note 1: with correction for the injection conditions

Multimode waveguide

The last example is a multimode waveguide, sketched in Fig. V.5 with its optogeometrical parameters. This structure carries four guided modes. Here again, the MCR algorithm retrieves the given amplitudes and phases. After correction for negative sign of the eigenfield (paragraph IV.4.1), the propagation phases were also retrieved. The given and retrieved coefficients are presented in Table V.3. for several input spot positions x_i.

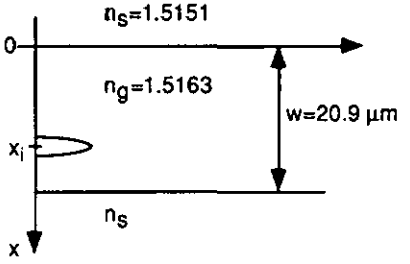

Fig. V.5 Multimode waveguide carrying four modes; propagation length: L=1.5 mm

In this case, the phases accumulated by propagation in the waveguide are greater than 2π. Therefore, we also have to apply the periodicity correction (paragraph IV.4.1) to the phases retrieved by the algorithm, in order to recover the phases due to propagation.

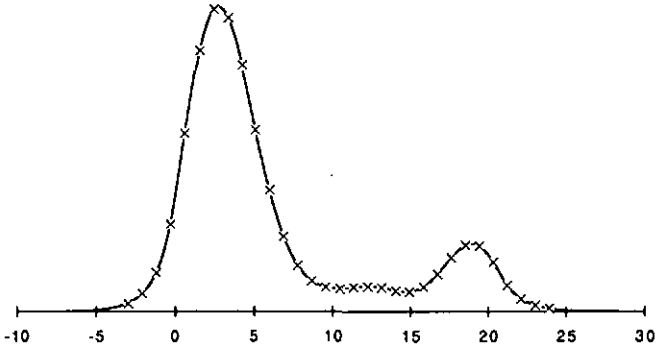

Fig. V.6 Given (crosses) and retrieved (solid line) intensity distributions in the multimode waveguide of Fig. V.5, for input light spot position x_4=15.45 µm

With this multimode waveguide, the MRC algorithm finds a local minimum for some input spot locations, e.g. x_i=5.45 µm and x_i=15.45 µm. Yet, for this latter light source position, the given and calculated intensity distributions are in close agreement, as shown in Fig. V.6. Therefore, comparing the retrieved intensity distribution does not enable the

distinction between the solution and a local minimum. This example proves the existence of a local minima, or even of a second solution to equation (IV.7). This question is examined in more detail in the next Section.

Pos. x_i	Given coefficients $A_i^g = a_i^g e^{\varphi_i^g}$				Retrieved coefficients $A_i^r = a_i^r e^{\varphi_i^r}$				Propag. phases
3.0	a_0^g	0.173			a_0^r	0.173			
	a_1^g	0.275	φ_1^g	142.2	a_1^r	0.275	φ_1^r	142.2	142.2
	a_2^g	0.285	φ_2^g	373.8	a_2^r	0.285	φ_2^r	13.8	373.8[2)]
	a_3^g	0.161	φ_3^g	680.9	a_3^r	0.161	φ_3^r	320.9	680.9[2)]
5.45	a_0^g	0.244			a_0^r	0.216			
	a_1^g	0.281	φ_1^g	142.2	a_1^r	0.312	φ_1^r	148.2	148.2
	a_2^g	0.097	φ_2^g	373.8	a_2^r	0.068	φ_2^r	18.0	378.0[2)]
	a_3^g	-0.165	φ_3^g	680.9	a_3^r	0.165	φ_3^r	166.1	706.1[1)2)]
7.5	a_0^g	0.282			a_0^r	0.282			
	a_1^g	0.202	φ_1^g	142.2	a_1^r	0.202	φ_1^r	142.2	142.2
	a_2^g	0.126	φ_2^g	373.8	a_2^r	0.126	φ_2^r	193.7	373.7[2)]
	a_3^g	-0.275	φ_3^g	680.9	a_3^r	0.275	φ_3^r	140.9	680.9[1)2)]
15.45	a_0^g	0.243			a_0^r	0.214			
	a_1^g	-0.282	φ_1^g	142.2	a_1^r	0.315	φ_1^r	327.3	147.3[1)]
	a_2^g	0.102	φ_2^g	373.8	a_2^r	0.070	φ_2^r	13.5	373.5[2)]
	a_3^g	0.159	φ_3^g	680.9	a_3^r	0.159	φ_3^r	344.1	704.1[2)]

Table V.3 Given and retrieved coefficients in the case of the multimode waveguide sketched in Fig. V.5; propagation length: 1.5 mm
Note 1: with correction for the injection conditions
Note 2: with periodicity correction

V.1.2. Determination of local minima in the squared error sum

The existence of local minima is a major problem of the presented method. Indeed, the optimization algorithm may converge to local minima, not to the desired solution, making the proposed method ineffective. Therefore, we study now these local minima in order to determine their number and some of their characteristics. We expect to find a mean to distinguish them from the desired solution or to set conditions avoiding the convergence of the algorithm to these false solutions.

In this study, we still simulate an intensity distribution from a given coefficient vector $\mathbf{A}^g$. However, the standard MRC algorithm is slightly modified: the initial vector $\mathbf{A}^0$ is now built from random coefficients. In such conditions, the algorithm converges to any local minimum. By repeating this procedure several times, each one with a different initial vector, we expect that all local minima are identified.

The initial mode coefficient vector $\mathbf{A}^0$ was calculated, first, by attributing a random value, uniformly distributed in the range of -0.5 to 0.5, to both real and imaginary parts $Re\{A_i^0\}$ and $Im\{A_i^0\}$. As usual, coefficient A_0^0 satisfies conditions (IV.3), i.e. it is real. Then, this initial vector $\mathbf{A}^0$ is introduced in the algorithm, where it is first normalized to the power carried by the intensity distribution (see paragraph IV.3.3). This process was repeated 50 times, each one with a different initial vector, for three- and four-branch directional couplers and for a multimode waveguide.

Directional couplers

In the case of the three-branch coupler sketched in Fig. V.1, the MRC algorithm with random initial vectors found one local minimum, in addition to the given coefficient vector $\mathbf{A}^g$. The normalized squared error sum of the local minimum is greater than zero, enabling an unambiguous distinction. Furthermore we observed that the amplitudes of the local minimum are different from the amplitudes of the given coefficients. This explains the robustness of the algorithm, where the phases only are optimized first.

The local minima of the four-branch coupler depicted in Fig. V.2 have been analysed. In this case, the MRC algorithm retrieved four minima or their complex conjugates. One of these minima is the given coefficient vector $\mathbf{A}^g$. All four vectors found by the algorithm are reported in Table V.4, each one with its occurence and the value of the normalized function f($\mathbf{A}$).

Here, we note that the solution appears with a normalized squared error sum $f^n(\mathbf{A})$ lower than 10^{-7}. On the contrary, the last three solutions found by the algorithm are local minima, as shown by their normalized squared error sum $f^n(\mathbf{A})$, which do not tend to zero. This could be a criterium for the distinguishing the solution from the local minima. However, in in experimental conditions, the normalized squared error sum $f^n(\mathbf{A})$ takes values higher than $300 \cdot 10^{-7}$. Therefore, this criterium is difficult to apply.

We can also observe that the amplitudes of the solution are different from the amplitudes of the local minima, similarly to the three-branch coupler case. This property also explains the robustness of the MRC algorithm for directional couplers.

Multimode waveguide

For studying multimode waveguides, we took again the structure depicted in Fig. V.3, carrying four guided modes. The input spot position is set to x_i=5.45 μm. Then, the MRC algorithm is run with a random initial mode coefficient vector $\mathbf{A}^0$. As for the four-branch coupler case, the mode coefficients reported in Table V.5 are corrected for the complex conjugation when necessary.

It can be seen in Table V.5 that the MRC algorithm retrieved three local minima, in addition to the solution. One of them is close to the solution, in term of phases: the amplitudes, specially of mode 1 and mode 2, can be distinguished. Regarding the other local minima, their amplitudes and phases of the other local minima are clearly different from the ones of the solution.

Retrieved coefficients A_i^r					Occurence	$f^n(\mathbf{A}^r)*10^7$
Given vector	a_0	0.1778			33	0
	a_1	0.2909	φ_1	70.4		
	a_2	0.2968	φ_2	171.4		
	a_3	0.1882	φ_3	269.7		
1st local minima	a_0	0.2592			9	40
	a_1	0.2534	φ_1	55.2		
	a_2	0.2087	φ_2	215.3		
	a_3	0.2539	φ_3	299.8		
2nd local minima	a_0	0.3102			4	88
	a_1	0.168	φ_1	104.7		
	a_2	0.2052	φ_2	113.0		
	a_3	0.2696	φ_3	233.3		
3rd local minima	a_0	0.3668			4	143
	a_1	0.0297	φ_1	130.7		
	a_2	0.0626	φ_2	56.6		
	a_3	0.3156	φ_3	278.4		

Table V.4 Retrieved coefficients with random initial conditions, for the four-branch coupler

Running the MRC algorithm with random initial vectors was repeated for an input light source position x_i=10.45 μm at the input of the multimode waveguide of Fig. V.4. In this case, the algorithm found only two minima, including the solution, i.e. the given coefficient vector $\mathbf{A}^g$.

Finally, we identified the minima of a multimode waveguide carrying 5 modes. The structure was similar to the one described in Fig. V.3, except for the waveguide width, increased up to 24 μm. The algorithm identified 6 to 8 local minima, depending on the input light spot location. Therefore, the number of local minima increases with increasing guided mode number. This observation may limit the applicability of the MCR algorithm if one cannot select the solution among the local minima of the normalized squared error sum $f^n(\mathbf{A})$. We propose now some ways for treating this problem of local minima.

Retrieved coefficients A_i^r					Occurence	$f^n(A)*10^7$
Given vector	a_0	0.2425			2	0
	a_1	0.2819	φ_1	142.2		
	a_2	0.1019	φ_2	13.8		
	a_3	0.1592	φ_3	140.9		
1st local min.	a_0	0.2138			17	0
	a_1	0.3149	φ_1	147.2		
	a_2	0.0705	φ_2	13.5		
	a_3	0.159	φ_3	164.1		
2nd local min.	a_0	0.1351			14	52
	a_1	0.3064	φ_1	69.3		
	a_2	0.1928	φ_2	231.1		
	a_3	0.1606	φ_3	121.6		
3rd local min.	a_0	0.1615			17	89
	a_1	0.1554	φ_1	176.9		
	a_2	0.3077	φ_2	12.7		
	a_3	0.1633	φ_3	270.9		

Table V.5 Retrieved coefficients with random initial vectors, for the multimode waveguide; input light source position: x_i=5.45 μm

Convergence to the solution

The problem of the local minima can be treated in two different ways. First, it is possible to promote the convergence of the algorithm to the desired solution. This approach have been chosen and is described in the present Section. Second, it is possible to set a criterion for selecting the solution among several retrieved minima. This is discussed later in this paragraph.

Promoting the convergence of the algorithm to the solution can be achieved in two ways: first, by the proper choice of the initial vector, second by the choice of the algorithm itself. In the former case, it can be understood that, if the initial vector is close to this solution, then the algorithm have a good probability to converge to the solution. In order to calculate an initial vector close to the solution, we assume that the input spot position x_i is known with a good accuracy. From that, we compute the

amplitudes a_i^0 of the initial vector coefficients, as it was carried out in paragraph V.1.1, using equation (V.3). In order to avoid the convergence to the complex conjugate of the solution, we set for the phase φ_1 of the mode 1 coefficient equal to the value calculated theoretically (equation V.4), while the other phases are set to zero. As a result, the amplitudes of the initial coefficient vector $\mathbf{A}^0$ are close to the solution, but not the phases. This choice of initial mode coefficient is the first possibility for promoting the convergence of the algorithm to the solution. We give now a second way: the choice of the algorithm.

When the appropriate initial coefficient vector is chosen, the MCR algorithm starts the iteration by first optimizing only the phases φ_i. Therefore, the phases of the retrieved coefficient vector $\mathbf{A}^r$ get closer to the ones of the solution. Then, the coefficient vector $\mathbf{A}^r$ cannot anymore converge to a local minimum when both amplitudes and phases are optimized. Hence, the MRC algorithm brings the retrieved coefficient vector $\mathbf{A}^r$ to the desired solution.

Thanks to the appropriate choice of the initial vector and of the algorithm, we observed that the MRC method always converges to the solution when it is applied to directional couplers. This is true even when we calculated the initial vector amplitudes by using a shifted input spot position $x_i \pm 1.5$ µm, instead of x_i. Namely, inexact initial amplitudes a_i^0 are used in the first part of the algorithm. The proposed method is therefore well adapted for studying directional couplers.

In the 20.9 µm wide multimode waveguide, we observed that the MRC algorithm converges, either to the solution, or to a local minimum close to it, depending on the input spot location. For example, the solution was conveniently retrieved when the input spot location is set to x_i=3.0 µm. On the contrary, the algorithm recovered the local minimum when x_i=5.45 µm was chosen. In this latter case, setting the initial vector to $\mathbf{A}^0 = 1.01 \cdot \mathbf{A}^g$ still led to the local minimum, as well as reducing from 1.5 mm down to 1.25 mm the propagation length assumed in the simulation. Therefore, the convergence of the MRC algorithm to the solution is mostly affected by the choice of appropriate input spot positions, rather than to other parameters.

A theoretical analysis of the normalized squared error sum could certainly determine the input spot locations for which the algorithm converges more

surely to the solution rather than to the local minimum. However, this could not garantee the convergence to the solution. Therefore, the possible retrieving of a local minimum must be assumed. Consequently, we need a criterion for distinguishing the solution from a local minimum. This is described hereafter.

Selecting the solution

We propose in this paragraph a criterion for determining, from two retrieved coefficient vectors, which one is the more likely solution. This condition uses the retrieved amplitudes a_i^r and involves the correlation product of the retrieved amplitudes a_i^r with the amplitudes a_i^0 of the initial vector, given by:

$$C = \sum_{i=0}^{N} a_i^0 \cdot a_i^r \qquad i=0, 1,...N \qquad (V.6)$$

where N is the highest mode order

Since we assumed that the initial vector amplitudes are quite close to the ones of the solutions, the correlation product C should be close to 1 when the retrieved coefficient vector is the solution, and lower in the case of a local minimum.

The application of this criterion supposes that both the solution and the close local minimum are retrieved. This can be achieved first by looking for a retrieved coefficient vector $\mathbf{A}^{r(1)}$, where the superscript 1 denotes the first retrieved coefficient vector. From this vector, a new initial vector $\mathbf{A}^0$ can be derived, by introducing small random variations to the mode coefficients. Feeding the MCR algorithm with this new initial vector leads to a second retrieved coefficient vector $\mathbf{A}^{r(2)}$. This iteration can be repeated until the Mth retrieved vector $\mathbf{A}^{r(M)}$ is different from $\mathbf{A}^{r(1)}$. Then, it can be reasonably expected that either $\mathbf{A}^{r(M)}$ or $\mathbf{A}^{r(1)}$ is the solution. Calculating the correlation product C of both retrieved vectors leads to the choice of one of them.

Testing the proposed criterion with simulated intensity distributions is obvious. Indeed, the correlation product C is equal to 1 when the solution is retrieved and lower when a local minimum is found. Therefore, the choice is unambiguous. The efficiency of this criterion can only be examined from experimental data.

Conclusions

Before concluding about local minima, we first discuss a question presenting some interest from a theoretical point of view. Namely, if $\mathbf{A}^g$ is a coefficient vector leading to the intensity distribution $S(x,\mathbf{A}^g)$, how many coefficient vectors $\mathbf{A}$ satisfy the equation $S(x,\mathbf{A})=S(x,\mathbf{A}^g)$. This question can be formulated differently. We defined in (IV.21) the squared error function $f(\mathbf{A})$ by:

$$f(\mathbf{A}) = \sum_{k=0}^{M} \left\{ S_{out}(x_k) - S(x_k, \mathbf{A}) \right\}^2 \qquad (V.7)$$

where $S_{out}(x_k)$ is the intensity observed at output point x_k
$S(x_k,A)$ is the intensity calculated from (IV.7) and
M is the number of sampling points

Now, setting:

$$S_{out}(x_k) = S(x_k, \mathbf{A}^g) \qquad (V.8)$$

we get: $f(\mathbf{A}^g)=0$. So, assuming equation (V.8) holds, the number of coefficient vectors $\mathbf{A}$ satisfying the equation $f(\mathbf{A})=0$ can be determined. We give hereafter arguments suggesting that the coefficient vector $\mathbf{A}^g$ is the unique solution, for any waveguiding structure.

When studying the local minima of directional couplers with random initial vectors, the MRC algorithm retrieved four distinct coefficient vectors: one was the solution, with $f^n(\mathbf{A})<10^{-7}$, and three were local minima, with $f^n(\mathbf{A})>10^{-7}$. Consequently, we may reasonably assume that directional couplers have a unique coefficient vector yielding $f(\mathbf{A})=0$. We believe that this feature is a result of the scalar wave equation, used as the fundamental hypothesis of our calculations. So, we expect that all waveguiding structures described by the scalar wave equation have only one coefficient vector satisfying $f(\mathbf{A})=0$. This is in particular the case of multimode waveguides. Accordingly, the retrieved coefficient vectors leading to $f^n(\mathbf{A})<10^{-7}$ in paragraph V.1.2 are only local minima.

From a practical point of view, whether a coefficient vector $\mathbf{A}\neq\mathbf{A}^g$ leads to $f(\mathbf{A})=0$ or to $f(\mathbf{A})\approx 0$ is not very important. In both cases, the ONIDA algorithm may retrieve coefficient vectors different from the desired solution. Moreover, the numerical accuracy will never enable to distinguish if the squared error sum $f(\mathbf{A})$ is strictly or approximately equal to zero.

Therefore, all coefficient vectors retrieved by the MRC algorithm, except the solution , will be considered as local minima.

We have seen in paragraph V.1.2 that the squared error sum f(**A**) have up to 3 local minima for directional couplers, in addition to the solution. This number increases up to 7 for multimode waveguides carrying 5 modes. Therefore, the number of local minima increases with the guided mode number. How is it possible to retrieve the solution in the presence of many local minima? We try now to answer this question.

For this purpose, we propose in the present paragraph some ways for, either promoting the convergence of the MRC algorithm to the solution, or for selecting the solution among several retrieved mode coefficient vectors. By the appropriate choice of the initial vector, the MRC algorithm safely converges to the solution when it is applied to directional couplers. It was not the case in multimode waveguides, for which the MRC algorithm led, either to the solution, or to a local minimum close to it. Therefore, we set in the present paragraph a criterion for distinguishing the solution from a local minimum.

So, we expect that the proposed method can successfully retrieve the phase differences accumulated by propagation in both directional couplers and few mode waveguides. Therefore, we will be able to reach the main goal of this work: determining the intermodal dispersion of multimode waveguiding structures.

V.1.3. Effects of errors in waveguide parameters

The optogeometrical parameters of the waveguides are supposed to be known for applying the MCR algorithm. Nevertheless, the experimental values are known with a limited accuracy. Therefore, we study in the present paragraph how optogeometrical parameter errors affect the retrieved coefficients. In particular, the width and the refractive index difference between waveguide and substrate will be examined. From this, we will deduce the expected error of the recovered amplitudes and phases, or, conversely, the required waveguide parameter accuracy.

For this analysis, we calculated an intensity distribution from a given coefficient vector $\mathbf{A}^g$ and given waveguide parameters. This distribution is then introduced in the MCR algorithm, but with modified waveguide parameters. Therefore, the eigenfields computed in the algorithm slightly differ from the ones used for calculating the given intensity distribution.

Three-branch directional coupler

For the three-branch directional coupler, the structure sketched in Fig. V.2 is used. In the following computations, the position of the input light source is x_0=1.95 μm, i.e. it is located in a side waveguide.

The **waveguide index** is first studied. In this case, the index is the same in all three branches of the coupler. The effect is depicted in Fig. V.7.

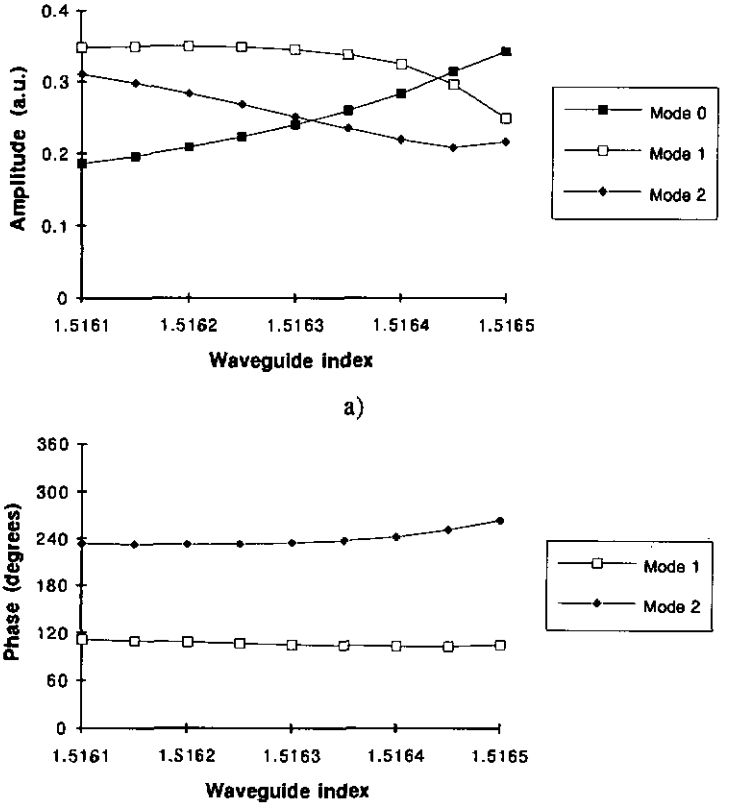

Fig. V.7 Amplitudes a) and phases b) retrieved by the MCR algorithm as a function of the waveguide index; three-branch coupler; input spot position: x_i=1.95 μm (side branch)

We deduce from Fig. V.7 that a $\pm 10^{-4}$ error of the refractive index yields a maximum phase error of ±8° and an amplitude error of about 16%. Injection in the central waveguide (x_i=10.95 µm) leads to similar values.

We next studied the effect of the **central branch width**. In this case, we deduced that the retrieved coefficients are only slightly affected by the waveguide width. With a ±0.2 µm width change, the relative accuracy of the amplitude is better than 6%, while the phase accuracy is still better than 6°. With the input spot position is located in the central branch (x_i=10.95 µm), the amplitude change reaches 8%, while the phase change is lower than 1°.

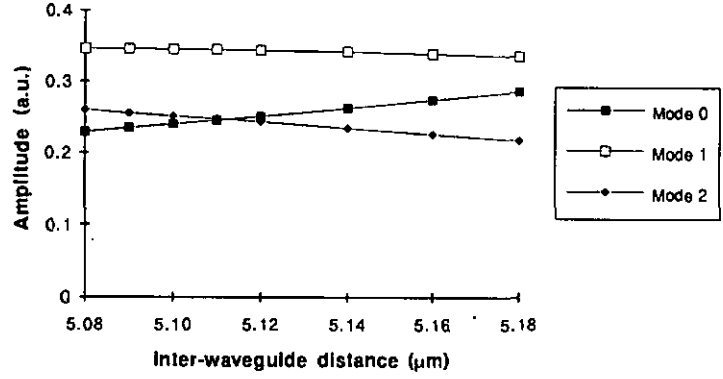

a)

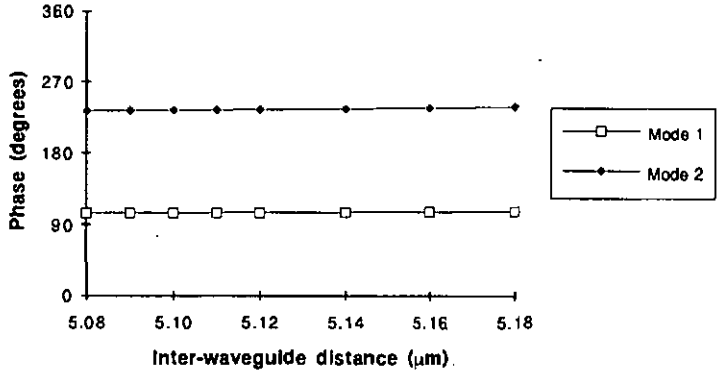

b)

Fig. V.8 Mode coefficient amplitudes a) and phases b), as a function of changes in the inter-waveguide distance d_c (see Fig. V.2); input spot position: x_i=1.95 µm (side branch)

The last geometrical parameter of interest is the **distance between waveguide axes**. Fig. V.8 shows the retrieved amplitudes and phases for a three-branch coupler.

In this case, a ±0.1 μm error of the distance between waveguide leads to a maximum amplitude error of 23% and less than 6° phase error. Injection in the central waveguide leads to similar results.

Note that other parameters have been studied, such as the index of the medium lying between waveguides. However, these effects were negligible and are not reported here.

The different contributions to the amplitude and phase errors are summarized in Table V.6 for the three-branch coupler of Fig. V.2.

	Relative amplitude error (%)	Phase error (degrees)
Waveguide width: ±0.2 μm	±6	±6
Waveguide index: $\pm 10^{-4}$	±16	±8
Distance between waveguides: ±0.1 μm	±23	±6

Table V.6 Maximum amplitude and phase errors for a three-branch coupler

As can be seen, the most important parameter is the waveguide index, which has a strong influence on the precision of both amplitudes and phases. Next the distance between waveguides and the waveguide width have similar effects on the amplitudes and phases.

Four-branch coupler

Some parameters of the four-branch directional coupler of Fig. V.3 have been similarly analysed by using simulated intensity distributions. In the examples below, the change of the amplitudes and phases are shown when the input light spot is located in one of the outer branches.

The **refractive index of the inner waveguides** is shown in Fig. V.9. Here, a $\pm 10^{-4}$ index change yields 29% of amplitude variation and about 11° phase change. When light is launched into the inner branch of the coupler, the sensitivity to index variations is lower for both amplitudes and phases.

We next studied the effect of both **outer waveguide widths**, with the light source position located in an outer branch (x_i=1.95 µm). We deduced that a ±0.2 µm variation of the outer waveguide width leads to a relative change of 11% for the amplitudes and less than 2° for the phases. When the input spot is located in an inner branch (x_i=7.05 µm), the sensitivity to the width is lower for both amplitudes and phases.

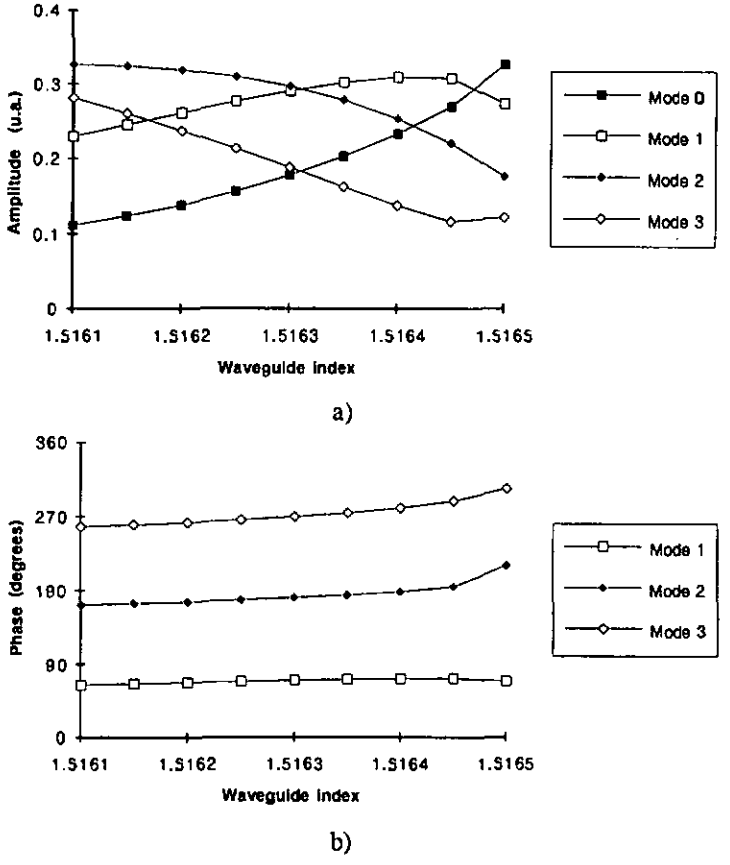

Fig. V.9 Amplitudes a) and phases b) retrieved by the MCR algorithm as a function of the waveguide index; four-branch coupler; source position: x_i=1.95 µm (outer branch)

The effect of the **distance between waveguides** d_c (see Fig. V.3) was also studied. We observed that a ±0.1 µm change of this distance leads to a 9%

change of the amplitudes and 3.5° of the phases, with the input spot position x_i=1.95 µm.

Table V.7 summarizes the errors observed for the studied parameters of the four-branch coupler. As in the three-branch coupler case, the waveguide index plays a major role in the retrieving accuracy of the algorithm. A fairly good approximation has to be found for proper operation of the ONIDA method.

	Relative amplitude error (%)	Phase error (degrees)
Waveguide width: ±0.2 µm	±11	±2
Waveguide index: $\pm 10^{-4}$	±29	±11
Distance between waveguides (d_e): ±0.1 µm	±9	±4

Table V.7 Maximum amplitude and phase errors for a four-branch coupler

Multimode waveguide.

Finally, we give some results obtained for the multimode waveguide sketched in Fig. V.5, carrying four modes.

When the **refractive index of the waveguide** changes, we observe the amplitudes and phases shown in Fig. V.10. The sudden change of the curves in Fig. V.10 is due to the fact that the MCR algorithm finds a local minimum for the waveguide index n_g=1.5165. Excluding this value for the sensitivity calculation, we find a maximum phase error of about 6° for a $\pm 10^{-4}$ index change, and a maximum amplitude error of 3%. At other input light spot positions, the situation is similar. It can be noted that the sensitivity of the multimode waveguide to the index change is lower than the one of directional couplers.

The phase and amplitude variations due to a ±0.1 µm change of the **waveguide width** are about 5° and 3% respectively, for the input light source position x_i=3 µm. For other input light spot positions, the variations

are usually lower. However, they may also dramatically increase in some particular conditions. This was the case for mode 2 with light injection at location x_i=5.45 μm: the amplitude change reaches 26% and the phase change 15°.

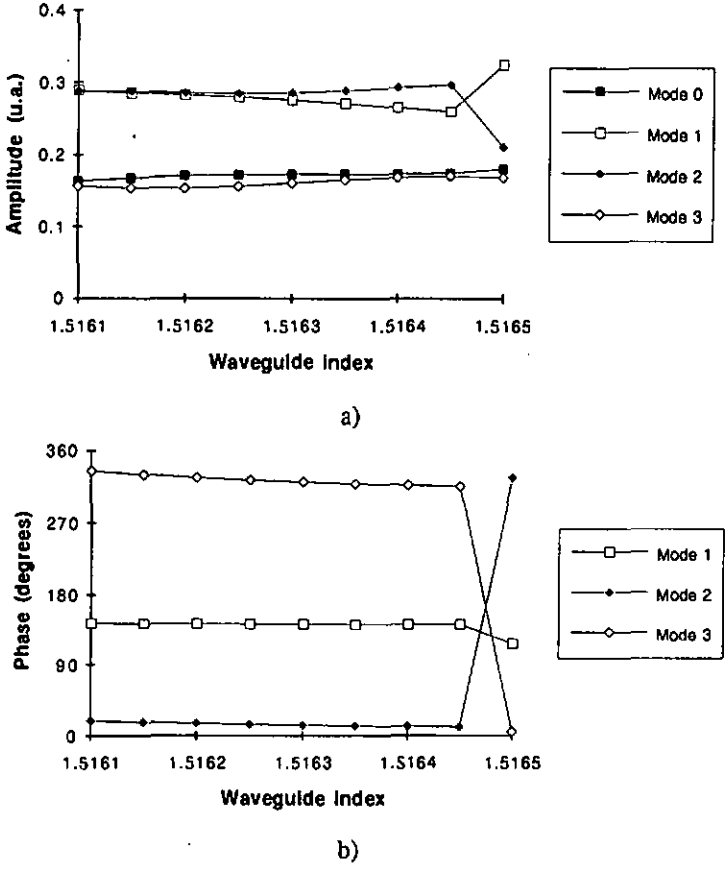

Fig. V.10 Amplitudes a) and phases b) retrieved by the MCR algorithm as a function of the waveguide index; multimode waveguide; light source position: x_0=3.0 μm

Table V.8 summarizes the contribution of optogeometrical parameter variations on the retrieved amplitude and phase accuracies, in the case of the multimode waveguide of Fig. V.5.

	Relative amplitude error (%)	Phase error (degrees)
Waveguide width: $\pm 0.2\ \mu m$	±6	±10
Waveguide index: $\pm 10^{-4}$	±3	±6

Table V.8 Maximum amplitude and phase errors for a multimode waveguide.

V.1.4. Effects of alignment errors

It was mentioned in paragraph IV.3.2 that the coordinate systems of the computed waveguide and of the actual structure should coincide. We evaluate now the magnitude of the coefficient errors due to the misalignment the x coordinate.

For this purpose, we calculated an intensity distribution $S(x_k)$ for a given set $\{x_k\}$. Then, this distribution was introduced in the algorithm with the set $\{x_k-\Delta x\}$ replacing $\{x_k\}$. Therefore, the algorithm estimated the residuals:

$$r_k(\mathbf{A}) = S_{out}(x_k) - S(x_k - \Delta x, \mathbf{A}) \qquad (V.9)$$

and computed the optimized mode coefficient vector **A** according to (V.9).

Three-branch coupler

The relative variation of the amplitude and the phase variations are plotted in Fig. V.11 for the three-branch coupler depicted in Fig. V.2.

In this case, the phase error due to a 0.05 µm misalignment is lower than 3°. The amplitude changes from about 10%. Locating the input spot into the central branch (i.e. x_i=10.95 µm), leads to similar results.

Four-branch coupler

The four-branch coupler used in this analysis has been sketched in Fig. V.3. The amplitude and phase errors versus the misalignment are shown in Fig. V.12.

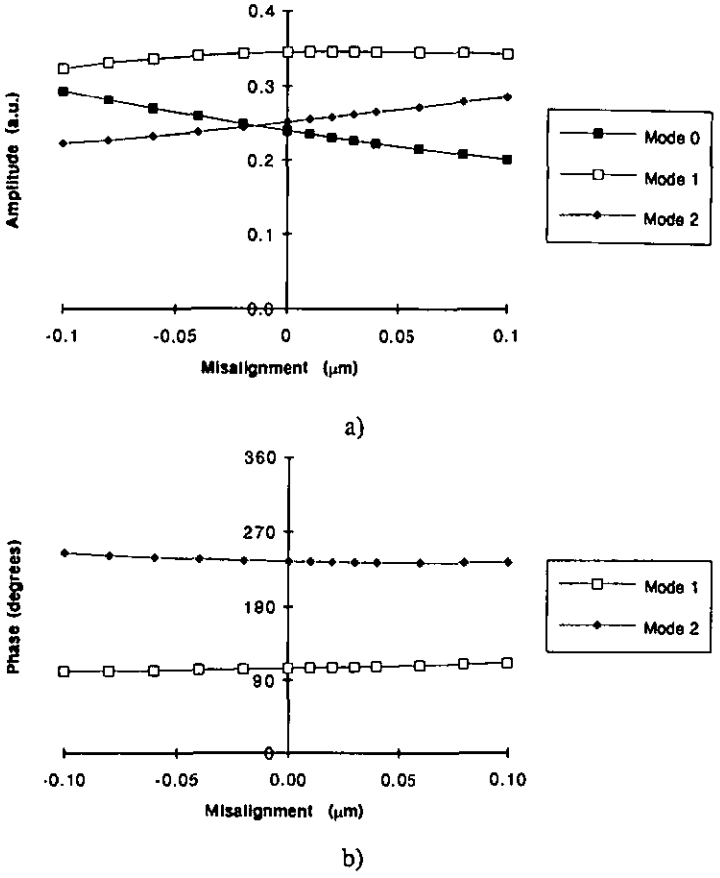

Fig. V.11 Amplitude (a) and phase (b) errors due to misalignment of the output coordinate systems, for three-branch coupler; input spot position: x_i=1.95 μm (side branch)

From Fig. V.12, the phase error in this case is lower than 7° for a misalignment variation of ±0.05 μm, and the amplitudes less than 3%. When the input spot is located in an inner waveguide, the errors are 6° and 4% for the phases and the amplitudes respectively.

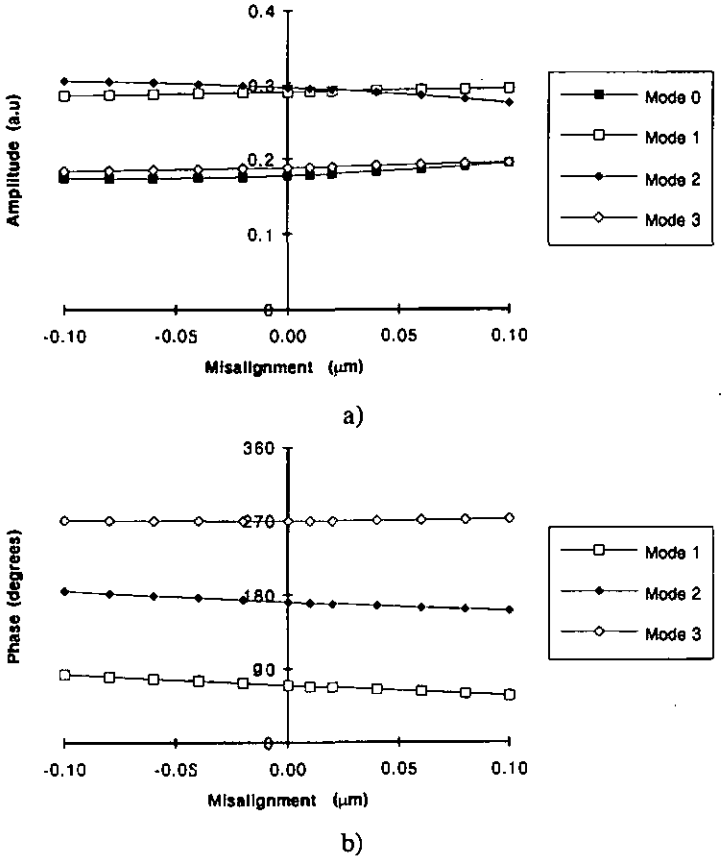

Fig. V.12 Amplitude (a) and phase (b) errors due to misalignment, for four-branch coupler; input spot position x_i=1.95 μm (outer branch)

Multimode waveguide

Finally, the sensitivity to misalignment of the calculation and the measurement coordinate systems is shown in Fig. V.13 for the multimode waveguide outlined in Fig. V.5.

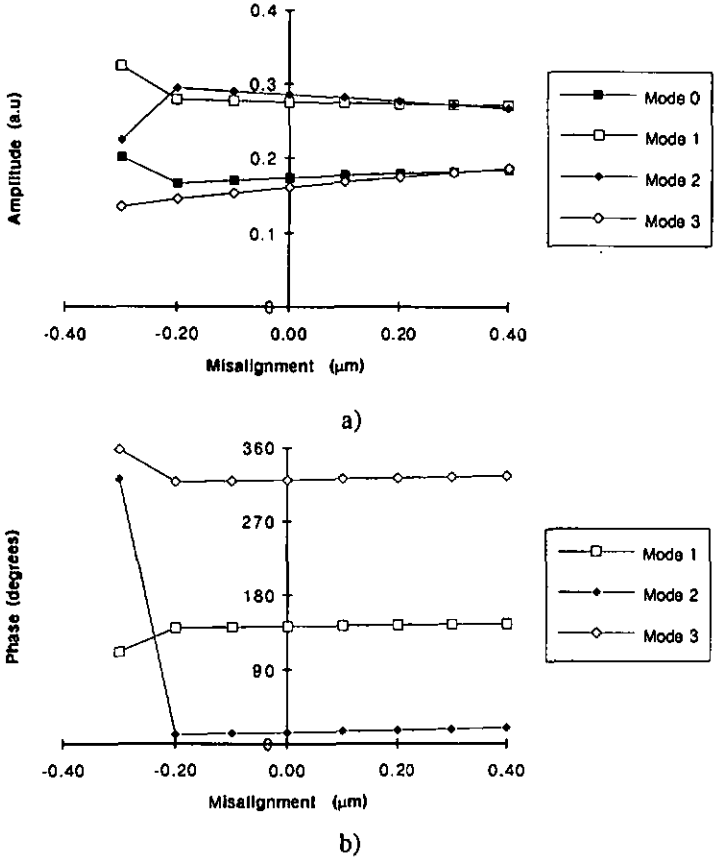

Fig. V.13 Amplitude (a) and phase (b) errors due to misalignment, for the multimode waveguide; input spot position x_i=3.0 μm

The sudden curve change for a -0.3 μm misalignment is explained by the convergence to a local minimum. Excluding this point, we deduce, for a ±0.05 μm misalignment, maximum errors of 1° and 2.5% for the phases and the amplitudes respectively. These sensitivities are similar for other input spot positions. It is interesting to note that the phase and amplitude errors increase up to 8° and 25%, respectively, for input spot position x_i=5.45 μm, i.e. the position for which the MCR algorithm converges to a local minimum.

V.1.5. Effects of intensity measurement errors

As pointed out in paragraph IV.3.2, the effect of intensity measurement errors leads to a change of the vector norm $|\mathbf{A}|$, if the mean value of the errors are different from zero. Nevertheless, even with a mean value equal to zero, errors may be responsible for the change of individual components of $\mathbf{A}$, both in amplitude and in phase. Our intention is now to estimate these variations for a few known structures.

For this purpose, we introduced a random error to the calculated intensities, according to:

$$S(x) = S(x, \mathbf{A}^g)(1 + \sigma R) \qquad (V.10)$$

where σ is a proportionality coefficient giving the relative error and

R is a random value uniformly distributed in the range -1 to 1

Ten intensity distributions S(x) were derived from the same unperturbed distribution $S(x,\mathbf{A}^g)$ and introduced into the MCR algorithm. The minimum and maximum amplitudes and phases retrieved by the MCR algorithm are reported in Fig. V.14 for the four-guide coupler depicted in Fig. V.3. In Fig. V.15, similar curves are given for the multimode waveguide outlined in Fig. V.5.

In Fig. V.14a, the curves observed for mode 2 and for mode 3 are not depicted: they are very similar to the ones obtained for mode I and for mode 0, respectively. In all cases, the maximum phase deviation reaches 22° with a 10% variation of the intensities. Variation of the amplitudes, in the same conditions, are lower than 30%. Assuming a 2% accuracy for the measurement of the intensities, the resulting accuracy of the MCR algorithm is about 3° for the phases and 5% for the amplitudes.

For the multimode waveguide, the results of Fig. V.15 lead to the following conclusion: in order to achieve a ±5° phase accuracy, the tolerable intensity variation is 5%. It is 3% only for a ±5% accuracy of the amplitudes.

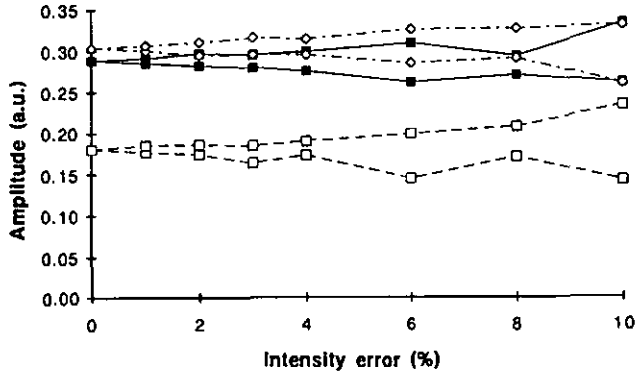

a)

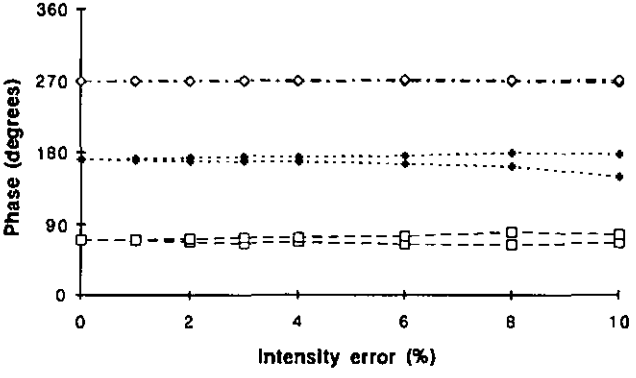

b)

Fig. V.14 Minimum and maximum amplitudes a) and phases b) reported over ten intensity distributions with intensity errors, in the case of a four-branch coupler; input spot position: x_i=1.95 μm (outer branch)
Continuous line: mode 0, dashed line: mode 1, dotted line: mode 2, dot-dashed line: mode 3; input spot location: x_i=3.0 μm

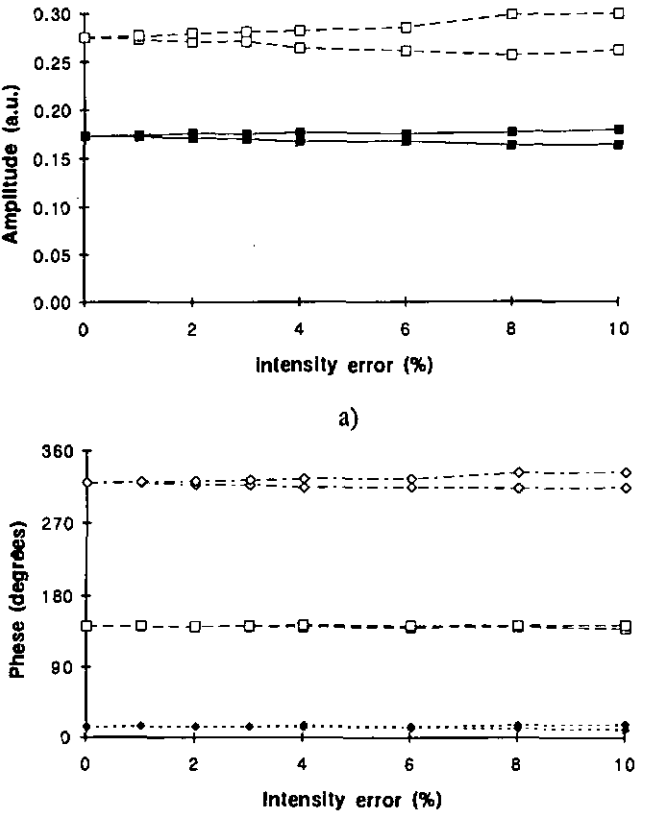

Fig. V.15 Minimum and maximum amplitudes a) and phases b) retrieved by the MCR algorithm for ten intensity distributions with intensity errors, in the case of the multimode waveguide of Fig. V.5.
Continuous line: mode 0, dashed line: mode 1, dotted line: mode 2, dot-dashed line: mode 3; input spot location: x_i=3.0 µm

In conclusion, the stability of the overall measurement system should be better than 2%. With this, the errors due to intensity variations will not exceed 5° and 5% for the retrieved phases and the amplitudes respectively. Some experiments will show the stability of the experimental set-up (see paragraph V.2.1).

V.1.6 Discussion of simulations

To conclude, Table V.9 summarizes the errors on the amplitudes a_i and phases φ_i reported in paragraphs V.1.3 to V.1.5. The studied parameters are the waveguide geometry and waveguide index, the alignment of the coordinate systems of the calculation and of the measurement, and, finally, of the intensity. These results are reported here for three- and four-branch couplers and for a multimode waveguide.

	3-branch coupler		4-branch coupler		Multimode waveguide	
	Amplitude (%)	Phase (degrees)	Amplitude (%)	Phase (degrees)	Amplitude (%)	Phase (degrees)
Wg width: ±0.2 µm	±6	±6	±11	±2	±6	±10
Wg index: $\pm 10^{-4}$	±16	±8	±29	±11	±3	±6
Distance: ±0.1 µm	±23	±6	±9	±4	-	-
Alignement: ±0.05 µm	±10	±3	±3	±7	±3	±1
Intensity: 2%	±5	±3	±5	±3	±5	±5

Table V.9 Comparison of the studied error sources, for the three- and four-branch couplers and for the multimode waveguide

Two of these parameters can reasonably reach the accuracy stated in Table V.9: the distance between branches of the directional couplers, and the intensity. The former is given experimentally by the photolithographic processes and reaches the assumed ±0.1 µm. On the other hand, the intensity error remains under the presumed 2% with up-to-date lock-in detection. Therefore, these parameters do not need a special attention.

The waveguide width and refractive indices are influenced experimentally by the photolithographic operations and by the ion-exchange conditions. The accuracy of both processes have been characterized, and, indeed, they lie inside the tolerances assumed in Table V.9. However, the MCR

algorithm works with an effective index approximation of the actual three-dimensional waveguiding structures. Furthermore a step index profile is assumed in the algorithm. Therefore, we have to deduce values for the waveguide width and refractive indices. This operation is based on experimental observations, but remains fundamentally arbitrary. Therefore, we cannot reasonably expect accuracies better than 0.3 µm for the waveguide widths, and $5 \cdot 10^{-4}$ for the waveguide indices. Such values lead to unsatisfactory amplitude and phase errors.

Regarding the alignment between the coordinate systems for the calculation and for the measurement, we estimate from the experimental observations that the accuracy is of the order of ±0.2 µm. This leads to unsatisfactory phase errors, reaching as much as 28°.

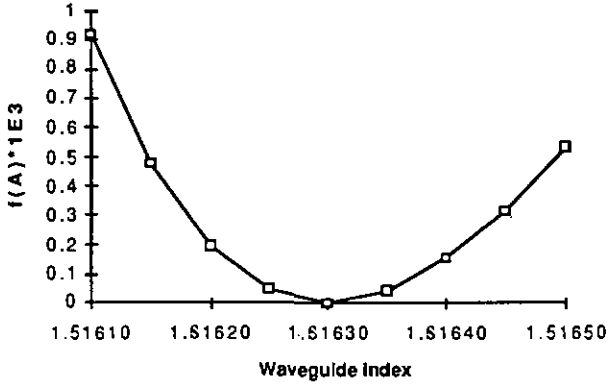

Fig. V.16 Normalized squared error sum $f^n(\mathbf{A})$ of the retrieved coefficient vector, as a function of the waveguide index; the same intensity distribution is introduced in the MCR algorithm for each index; three-branch coupler; input spot position: x_i=1.95 µm (outer branch)

As a result, the accuracy of the optogeometrical parameters of the waveguide and of the alignment have to be improved. For this purpose, we chose to use the MCR algorithm. This is made possible by the following observation: the minimum squared error sum $f^n(\mathbf{A})$, reported when the solution is retrieved, shows a nearly parabolic shape with a minimum, as a function of the waveguide parameters. As an example, Fig. V.16 depicts

the minimum normalized squared error sum $f^n(\mathbf{A})$, as a function of the refractive index of all three branches of a directional coupler.

A similar behaviour was observed with the waveguide width and the alignment error. So the MCR algorithm provides the means to tune the critical parameters of the experiment. For this purpose, we feed the MCR algorithm with a given intensity distribution, and we iteratively optimize the parameters for reducing the squared error sum $f^n(\mathbf{A})$ of the retrieved solution.

This procedure has been applied in the experimental demonstration of this work. All three waveguide structures were optimized by minimizing the normalized squared error sum $f^n(\mathbf{A})$. Experimentally, reduction of two to three orders of magnitude has been observed. This allowed to improve the accuracy of the waveguide index, of the waveguide width and the alignment, so that the values assumed in Table V.9 are reached, i.e. $\pm 10^{-4}$, ± 0.2 µm and ± 0.05 µm, respectively. We used these accuracy figures for estimating the precision expected from the MCR algorithm. This explains the accuracies assumed in Table V.9. From these values, the ONIDA method can measure the effective index differences with the required resolution of 10^{-5}, provided the length of the studied structure reaches about 3000 times the operating wavelength. Therefore, we conclude that the ONIDA method shows the potential for characterizing the intermodal dispersion of few mode integrated optic structures. So, we can test now this technique experimentally, with the help of some typical waveguiding structures, used for commonly used integrated optic devices. This demonstration is reported in the next Section.

V.2. EXPERIMENTAL RESULTS

V.2.1. Establishing the measuring set-up

Measuring bench

The measuring set-up is sketched in Fig. V.17. It consists of an injection system, a waveguide holder and an imaging system. A lock-in detection system completes the set-up, driven by a computer. Fig. V.18 shows a photograph of the measuring bench.

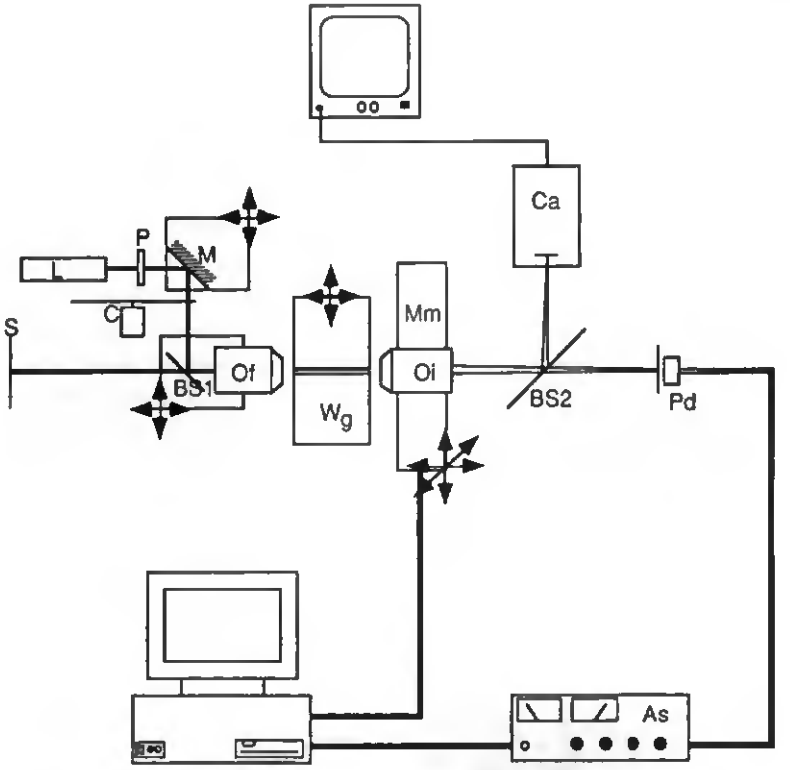

Fig. V.17 Sketch of the experimental set-up

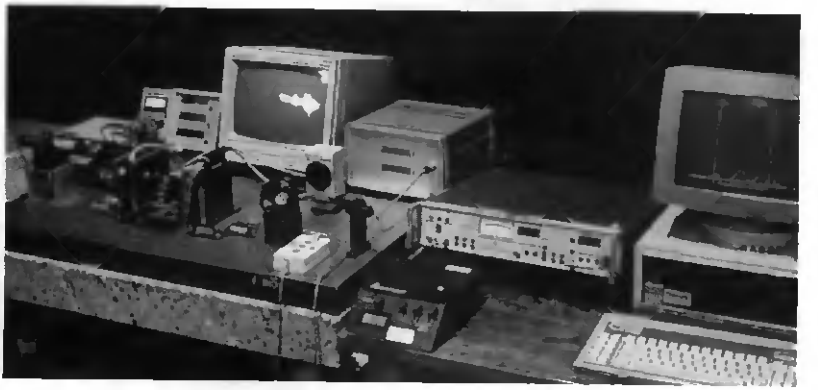

Fig. V.18 Photograph of the complete measuring bench

The **injection system** enables the scanning of the focused laser beam along the waveguide. To do so, a 1.2mm wide beam, emitted by a HeNe laser (L), first goes through a polarisor (P). Its intensity is then modulated by a chopper (C). Next a mirror (M) deflects the beam parallel to the scanning direction. Finally, the laser beam directed parallel to the waveguide axis by a beamsplitter (BS1). Then, it is focused at the waveguide input through a microscope objective (Of), with a 0.4 numerical aperture and a 4.34 mm focal length. At the focus point, the beam has a calculated radius of about 1.5 µm, thus satisfies the condition imposed by the calculation of the excitation mode coefficients (see paragraph IV.1). This light spot is laterally scanned by moving the focusing objective (Of) parallel to the waveguide end-face. However, it was important to scan the input light spot without affecting its shape. This is achieved thanks to two conditions: 1) the focusing objective (Of) and the beamsplitter (BS1) move together (they are mounted on the same microactuator), and 2) the beam incident on beam splitter (BS1) is parallel to the scanning direction. Thanks to these conditions, the beam reaches the focusing objective (Of) with a constant angle and a constant position, for any location of the microactuator along the x axis. Fig. V.19 shows a closed view of the injection system.

Fig. V.19 Picture of the injection system

In order to control the focus of the incident beam on the waveguide end-face, we use its Fresnel reflection on the substrate edge. The reflected beam goes back through beamsplitter (BS1) and is imaged on a screen (S)

located at some distance, typically 2 m. The image of the Fresnel reflection on the screen is focused with the help of a translator (T2). When this is achieved, the incident beam is considered to be focused on the waveguide input. Ideally, the screen should be located at infinity. However the error caused by the finite distance is quite negligible, taking the focal length of the microscope objective into account (f=4.34 mm).

The **sample holder** (Wg) enables movements along the x and y axes and rotations around three axes. So, the waveguide sample can be adjusted with a high precision.

The **detection system** is made of a microscope objective (Oi) imaging the waveguide output on the image plane, located about 400 mm away from the objective (NA=0.4, f=4.34 mm). This leads to a magnification factor of about 90. The waveguide end-face is scanned by moving the microscope objective mounted onto a motorized microtranslator (Mm). The movements of this stage are controlled along the x and y axes with a resolution of 0.02 µm, and driven by a microcomputer. A beamsplitter (BS2) forms a second image onto a camera (Ca), for an easy adjustment of the measurement set-up. The output intensity is captured by a ø50 µm fibre, leading to a resolution of 0.56 µm in the object plane, i.e. the plane of the waveguide output. The signals are detected by a pig-tailed photodiode (Pd) and amplified by a lock-in amplifier (As), also driven by the PC.

The intensity distribution observed at the waveguide output is a function of two coordinates, i.e. S(x,y). Since the effective index method is assumed in our implementation of the ONIDA method, S(x) must be introduced in the algorithm. The conversion from S(x,y) to S(x) can be performed in two ways. First, the intensity distribution can be measured at a fixed location y_0, yielding $S(x,y_0)$. In such a case, the coordinate system of the scanning jig must be parallel to the substrate edges, for maintaining the microscope objective at a constant level with respect to the substrate edge. We preferred a more tolerant method, consisting in integrating the intensity distribution along the y-axis, i.e. calculating:

$$\mathcal{P}(x) = \int_a^b S(x,y)dy \qquad \text{(V.11)}$$

If we choose the limits a and b on both sides of the distribution, in regions where the intensity is small, then the integral is insensitive to small

variations of the limits a and b. Experimentally, we approximated the integral (V.11) by a summation: 7 sampling points are scanned along the y-axis, with a 1 μm step, and the intensities summed up. We expect from this a reduced sensitivity to the parallelism of the scanning jig with respect to the waveguide axes.

Software

The software package is composed of two separate parts. The first one is dedicated to the control of the measuring bench and to the output intensity distribution measurement. The second part implements the ONIDA method itself, which runs independently on a faster computer.

The **measuring software** request the measured sample data from the user: sample characteristics and optogeometrical parameters of the waveguide structure. Then the main features of the measurement are introduced: operating wavelength, scanning range, number of sampled points, etc. Next, the program drives the user through the alignment procedures of the input light spot and output intensity distributions. Finally, up to nine output intensity distributions can be measured and stored, each with a different position of the input light spot. The speed of the measuring software is limited by the motorized microtranslator (Mm). Therefore, the use of a computer running with a 8086 processor is sufficient. The measurement of an intensity distribution lasts approximately 5 min.

The **analysing software** recovers the stored intensity distributions and applies the ONIDA method to these data. The waveguide parameters can be modified, as well as the alignment of the output reference systems. This software also helps the user for calculating the effective index differences from the retrieved phases. The Mode Coefficient Retrieving (MCR) algorithm used for the calculation of the mode coefficients (see paragraph IV.3.3) requires a great amount of computation. Therefore, using a 386 microprocessor is quite advantageous. In such conditions, retrieving the coefficients from an intensity distribution lasts less than 30 sec.

Alignment procedures

Before starting the intensity distribution measurement, a few alignment procedures must be carried out. Because the position of the input light source must be known for calculating the excitation coefficients, a

reference has to be found for the input coordinate system. Then, the input beam incidence angle has to be adjusted, in particular when multimode waveguides are measured. Finally, the coordinate system of the output intensity distribution must also be referenced. We describe now these procedures.

In the measurement, we first set the **reference of the injection system.** This is achieved differently, depending on the measured waveguide structure. Indeed, the reference of a directional coupler is easily found by observing the maximum coupling efficiency in one of the branches. However, this is more difficult to achieve in a multimode waveguide. Two procedures have been applied in this work, both leading to similar accuracies. The easiest method begins by locating the excitation light spot near the edge of the waveguide and taking note of the position of the microtranslator. In that case, the highest order modes are mainly excited. This situation is shown in Fig. V.20. Next, the input spot is moved to the other waveguide side, in such a way that a reversed intensity distribution is observed (see Fig. V.20). Then, the position of the waveguide center is given by the mean value of both positions.

The second procedure consists in adjusting the input light spot at the centre of the waveguide. Indeed, at this position, only even modes are excited, leading to a symmetrical output intensity distribution, for any propagation length (see Fig. V.21).

a) b)

Fig. V.20 Photograph of the waveguide output, with the input spot located near the right side of the waveguide (a), and near the left side (b).
Multimode waveguide width: 18 µm

In the case of directional couplers, the coordinate system is referenced with an accuracy given by the microtranslator resolution: ±0.25 µm. In multimode waveguides, we estimate the accuracy of ±0.5 µm when

searching for the center of the waveguide. By excitation of highest order modes, the precision reaches approximately ±0.75 μm.

For achieving the symmetrical intensity distribution in a multimode waveguide, as observed in Fig. V.21, the focused beam must arrive on the waveguide input face at normal incidence. The adjustment of the **input beam angle** to normal incidence is carried out by observing the output intensity distribution. First, the input light source is located at the centre of the waveguide input. Then, the incident beam angle is adjusted by moving mirror M1 until the output intensity distribution shows a symmetric shape. This case is illustrated by the photograph of Fig. V.21

Fig. V.21 Photograph of the waveguide output, with the input spot located at the waveguide centre, with a symmetric output intensity distribution, denoting the correct adjustment of the input beam incidence angle
Multimode waveguide width: 18 μm

An better alternative is to choose a position of the input light spot near the waveguide centre, for which a clearly recognisable output intensity distribution is observed, as shown for instance in Fig. V.22. Next the light spot is moved to the position symmetric with respect to the waveguide centre. At this second position, the output intensity distribution must show a symmetric shape with respect to the previous input spot position, unless the input beam is not adjusted to normal incidence.

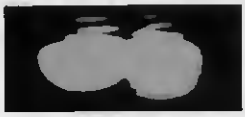

Fig. V.22 Photograph of the waveguide output, with the input spot located at 3 μm apart of the waveguide centre, providing an easily recognizable output intensity distribution
Multimode waveguide width: 18 μm

Therefore, moving the input light source from one location to the other and tuning the incident angle until a symmetric shape is obtained for both input positions leads to a correct incidence beam angle. The achievable accuracy reaches about 0.7°.

Aligning the **output coordinate** systems of the measurement and of the calculation at the waveguide output is performed in two steps. First, we measure the output intensity distribution. An appropriate situation for this purpose is obtained with the input light spot located near the waveguide side, namely with the highest order modes mainly excited. Then, the measured distribution is displayed on the computer screen together with the calculated highest order eigenfield. The position of the imaging system is corrected according to this observation. Usually, we repeat this operation until no visible misalignment remains. The estimated accuracy is of the order of 0.2 μm. With that precision, the simulation of the MCR algorithm shows a phase error reaching 30°, as demonstrated by simulations. As a consequence, the alignment accuracy must be improved.

This is achieved after the intensity distributions have been measured, directly using the MRC algorithm implemented in the analysing software. The alignment is corrected with the help of the software, in order to reduce the normalized squared error sum $f^n(\mathbf{A})$ at the end of the algorithm (see paragraph V.1.6). This method is applied to all measurements presented below. The accuracy of this alignment method is estimated to about 0.1 μm.

Parameter optimization

By applying the MRC algorithm of the analysing software, we also optimize the optogeometrical parameters, choosing the waveguide widths and refractive indices leading to the minimum value of the normalized function $f^n(\mathbf{A})$. It is possible to reduce $f^n(\mathbf{A})$ by two to three orders of magnitude. Usually, we compute the optimal parameters of a given waveguide, using three to four output intensity distributions, each obtained with a different input spot position. Then, we take the mean values of the optimized parameters for analysing the modal propagation. The estimated accuracies reach 10^{-4} for the indices and 0.1 μm for the waveguide widths.

Stability of the measuring set-up

As pointed out in paragraph V.2.1., the measurement of nine intensity distributions takes about one hour. In such conditions, the stability of the set-up is an important factor of the measurement accuracy. Accordingly we analysed this particular feature. For this purpose, we used the three-branch coupler and measured ten intensity distributions, one every 8 minutes, keeping exactly the same measurement conditions. Next, the alignment of the measurement and calculation coordinate systems was corrected with the MRC algorithm and the amplitudes and phases were retrieved.

We first applied this procedure with the input light spot located in the central branch of a three-branch directional coupler. Using a mean optimized alignment for all ten intensity distributions, the standard deviation computed for the amplitudes is lower than 1% for modes 0 and 2. Mode 1, which was weakly excited in this case, showed a 2% standard deviation. For the phases, the standard deviation is lower than 1° for both mode 1 and mode 2. Surprisingly, when the alignment is individually optimized for each intensity distribution, the standard deviations are slightly higher: it reaches for instance 2.5% for the amplitude of mode 1. When injecting in the side branch of the coupler, the standard deviations of the amplitudes are lower than 4% for all three guided modes. For the phases, the standard deviation reaches 2.5°.

In conclusion, the stability of the measuring set-up is not an important error source, as compared to the waveguide parameters, such as the waveguide refractive index. Therefore the measuring set-up used in the present work can be considered as satisfactory.

V.2.2. Experimental data

The waveguide structures used in these experiments have been realized by ion-exchange in glass. The optogeometrical parameters used for calculating the eigenfields were optimized by minimizing the squared error sum, as described in Section V.1.6.

Three-branch directional coupler

For the three-branch directional coupler, we found the following optimimum parameters:

n_s=1.5151	substrate index
n_g=1.51627	waveguide indices
w_e=3.91 µm	outer waveguide width
w_i=3.87 µm	inner waveguide width
d_e=5.11 µm	distance between branch axis

We also optimized separately the refractive indices of the central branch and of the side ones. This did not lead to noticeable improvement. Similarly, changing the refractive index of the medium lying between the coupler branches did not produce significant effects.

Using these optimized parameters, we studied a 4.58 mm long three-branch coupler. Nine different output intensity distributions have been measured, with the input spot located: in the right branch for the first three measurements (x_1 to x_3), in the central branch for the next three (x_4 to x_6) and in the left branch for the last three (x_7 to x_9). The mode coefficient phases and amplitudes are plotted in Fig. V.23.

For mode 1, the phases vary in a ±13° range if we exclude the measurements made with input spot positions x_4 to x_6. For these positions, the mode amplitude is small (see Fig.V23a), therefore the measurement is not significant. For mode 2, the phases lie in a range of ±20°. If we weight the phases by their corresponding amplitude and take the mean values, we get: φ_1=174° for mode 1 and φ_2=267° for mode 2, leading to the following effective index differences: $\Delta n_{01}=n_0-n_1=6.7\cdot10^{-5}$ and $\Delta n_{02}=n_0-n_2=10.3\cdot10^{-5}$. This can be compared to the phases calculated theoretically for this structure: φ_1=119° and φ_2=284° [49], corresponding to the effective index differences $\Delta n_{01}=4.57\cdot10^{-5}$ and $\Delta n_{02}=10.9\cdot10^{-5}$. The phase variations predicted by simulations of parameter errors led to a phase accuracy better than ±25°. This corresponds fairly well with the experiment, which shows a variation of ±20°, leading to a variation of $\pm0.75\cdot10^{-5}$ for the index differences. Furthermore, we can note that the amplitudes observed for mode 1, when the input spot is located in the central branch, are close to zero. This was expected from the injection conditions.

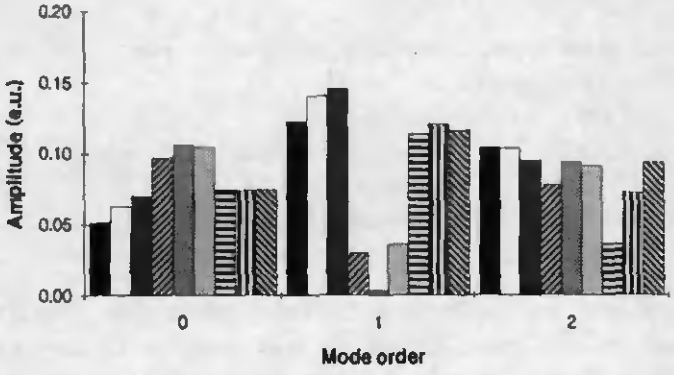

a)

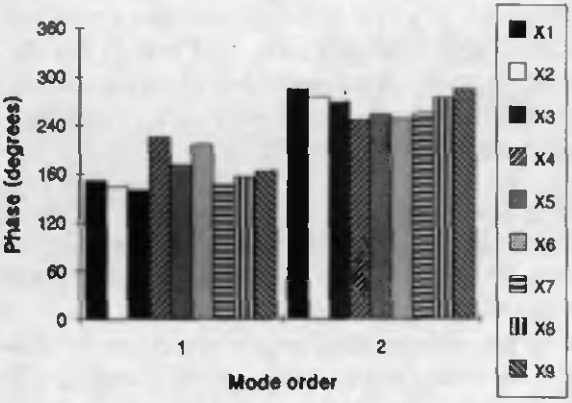

b)

Fig. V.23 Amplitudes a) and phases b) retrieved for a three-branch coupler, for different positions of the input light spot (x_1 to x_3 are located in the right branch, x_4 to x_6 in the central one and x_7 to x_9 in the left one)

As an example, Fig. V.24 below shows the agreement obtained between the measured and calculated intensity distributions for the input position x_2 located in the right branch of the coupler.

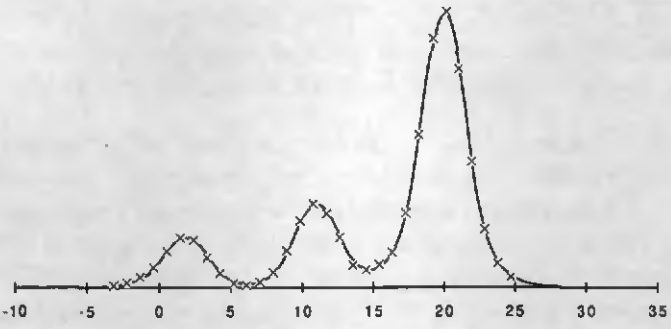

Fig. V.24 Measured (crosses) and calculated intensity distributions (solid line), for a three-branch directional coupler; input spot position: x_2 (right branch)

In Fig. V.25, we show the pictures of the intensity distributions observed for the input spot located in the central and in a side branch of the coupler.

Fig. V.25 Picture of the output intensity distribution, a) with the input spot located in the central branch and, b) located in a side branch of the three-branch coupler

A weakly coupled structure was also analysed with the ONIDA method. In this case, the distance between waveguide center was 13 µm. The retrieved phases lay in a very large range, confirming the description of paragraph IV.3.2. It was stated that sampling points chosen in the waveguides lead to only three orthogonal equations. All other sampling points yield equations close to one of these three, except in the intervals between waveguide. We deduced that such structures cannot be analysed correctly by the ONIDA method. The experiment verified this deduction.

Similarly, we studied an asymmetrical three-branch coupler: the central branch was about I µm wider than the outer ones. In this case, the power

exchange between waveguides is not complete. This is explained by the shape of the eigenfields: for a given mode, most of the energy is concentrated in the central or in the outer waveguides [46]. In this case again, the coefficients retrieved by the MCR algorithm were disappointing.

The positive results obtained with the three-branch are attributed to two reasons: first, the structure is simple and can be easily and accurately described by the effective index and the step-index profile approximations. Second, the injection conditions, mainly the incidence angle of the input spot source, are not critical parameters, as was shown by experimental observations. Therefore, the MCR algorithm can be conveniently applied to this type of structure, provided the waveguides are not weakly coupled and the branches do not present a strong asymmetry.

Four-branch directional coupler

The ion-exchanged four-branch coupler was optimized keeping the same refractive index in all four branchs and the same width for the inner and outer branchs respectively. The optimized parameters are:

n_s=1.5151	substrate index
n_g=1.51638	waveguide index
w_e=3.78 μm	outer waveguide width
w_i=3.64 μm	inner waveguide width
d_e=7.12 μm	gap between outer waveguide and inner waveguides
d_i=7.36 μm	gap between inner waveguides

The propagation length is 4.58 mm. The input source is located: in the right outer branch (x_1 and x_2), in the right inner branch (x_3 to x_5), in the left inner branch (x_6 to x_8) and in the left outer branch (x_9).

Fig. V.26 shows the phases retrieved by the MCR algorithm, before the usual corrections for the eigenfield sign, periodicity and complex conjugation. This case clearly shows where the eigenfield sign correction has to be applied: for the input spot positions x_5 to x_9 for mode 1, measurements x_3 to x_8 for mode 2, and measurements x_3 to x_5 and x_9 for the highest order mode.

The phases due to propagation are shown in Fig. V.27. They are obtained from the retrieved phases shown in Fig. V.26, after corrections for

eigenfield sign, but without periodicity correction nor complex conjugation correction.

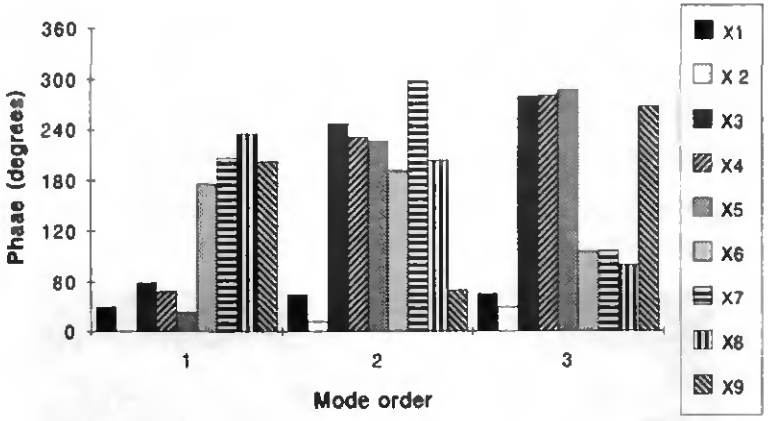

Fig. V.26 Phases retrieved by the MCR algorithm, before the corrections for the eigenfield sign at the waveguide input, periodicity and complex conjugation; input spot positions: x_1, x_2: right outer branch, x_3 to x_5: right inner branch, x_6 to x_8: left inner branch, x_9: left outer branch

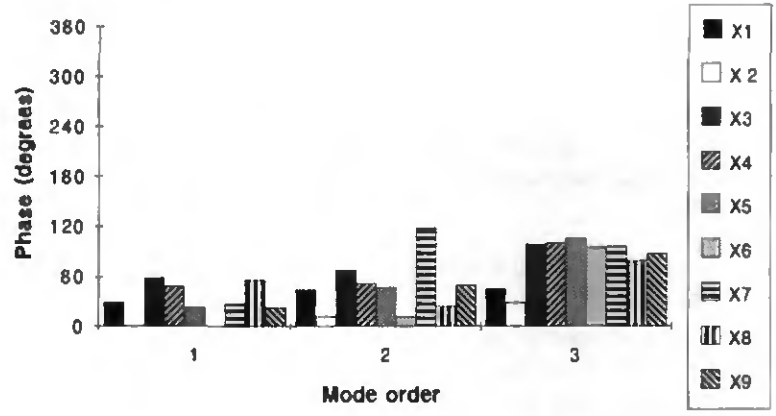

Fig. V.27 Phases retrieved by the MCR algorithm, after the correction for the eigenfield sign at the waveguide input; input spot positions: same as in Fig. V.26

Taking the mean value of the retrieved phases, weighted by their corresponding amplitude, we obtain: φ_1=27°, φ_2=37° and φ_3=85°. The phases calculated from the computed effective indices are: φ_1=14°, φ_2=78° and φ_3=138°, leading to effective index differences of $\Delta n_{01}=1.04\cdot10^{-5}$, $\Delta n_{02}=1.42\cdot10^{-5}$ and $\Delta n_{03}=3.26\cdot10^{-5}$ respectively. After the eigenfield sign correction, the retrieved phases vary in ranges of ±32° for mode 1, ±28° for mode 2 and ±39° for mode 3, which corresponds to effective index variations of $\pm1.22\cdot10^{-5}$, $\pm1.07\cdot10^{-5}$ and $\pm1.49\cdot10^{-5}$ respectively.

In Fig. V.28, the intensity distributions observed with injection in the inner and outer branchs of the four-branch coupler are shown.

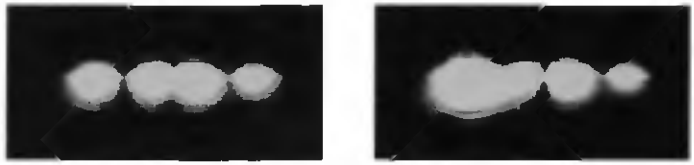

a) b)

Fig. V.28 Picture of the output intensity distribution, a) with the input spot located in an inner branch and, b) located in an outer branch of the four-branch coupler

From this experiment, we first note that the ONIDA method does not lead to practical conclusions when the phase differences between low order eigenmodes are as small as 14° or 27°, as it is the case in this example. Indeed, the phase errors expected for this type of structure reach ±29° (see paragraph V.1.6), which is higher than the phase differences to be measured. In this particular case, a 40 mm propagation length, giving a phase difference between mode 0 and mode 1 of about 120° would be more convenient.

The simulations predicted maximum variations of ±29°. The discrepancy with the observed variations of ±39° is due to the fact that this waveguiding structure is more complicated than the three-branch coupler. Therefore, it involves more optogeometrical parameters and, so, is more difficult to be described with the effective index and step-index profile approximations. This results in a too large difference between calculated and experimental eigenfields, thus to large variations of the retrieved phases.

Multimode waveguide

As an example of a multimode waveguide, we show in Fig. V.29 the propagation phases for a 17.2 μm wide waveguide. In this figure, the correction for eigenfield sign has already been introduced. Furthermore, we applied the correction for complex conjugation in order to arrange the mode 1 phase.

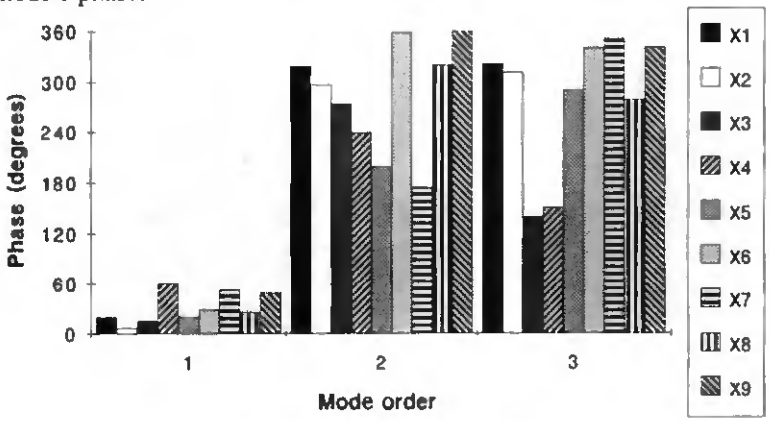

Fig. V.29 Phase retrieved by the MCR algorithm for a multimode waveguide; waveguide width: 17.2 μm, substrate index: 1.5151, waveguide index: 1.5167; x_1=0 μm; x_2=2 μm; x_3=4 μm; x_4=6 μm; x_5=8 μm; x_6=10 μm; x_7=12 μm; x_8=14 μm; x_9=16 μm;

The amplitudes corresponding to these measurements are presented as a function of the input spot position in Fig. V.30 for the first three modes. Except for the measurement with the input spot position x_i=16 μm, the general shape of the eigenfields is recognizable: mode 0 has a single bump; mode 1 has a depression in the waveguide centre, and mode 2 has two depressions. The shape of the last guided mode (mode 3) is not so clearly apparent, probably because the input spot locations, with a 2 μm interval, are unable to correctly sample the eigenfield shape.

The good agreement of the measured and calculated intensity distributions for two input spot positions x_i shows that the algorithm reconstructs correctly the distributions (see Fig. V.31).

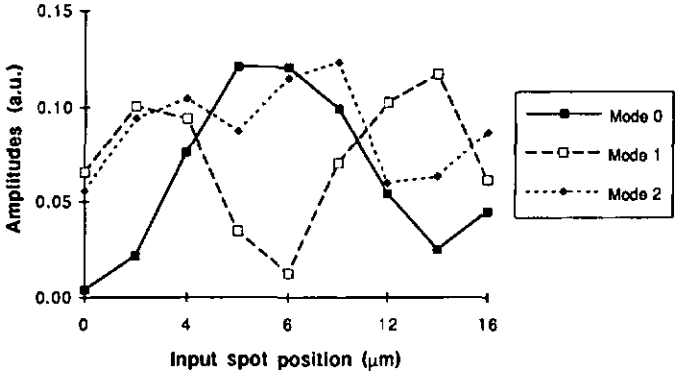

Fig. V.30 Amplitudes retrieved by the MCR algorithm for a multimode waveguide; waveguide width: 17.2 μm, substrate index: 1.5151, waveguide index: 1.5167

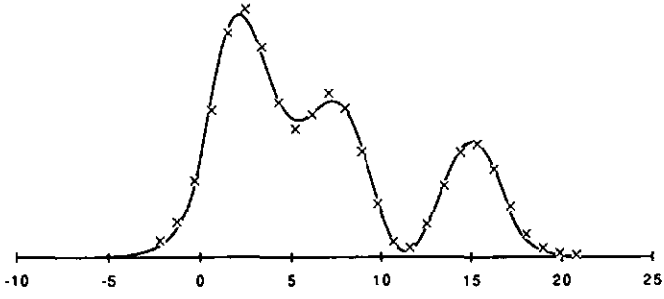

a)

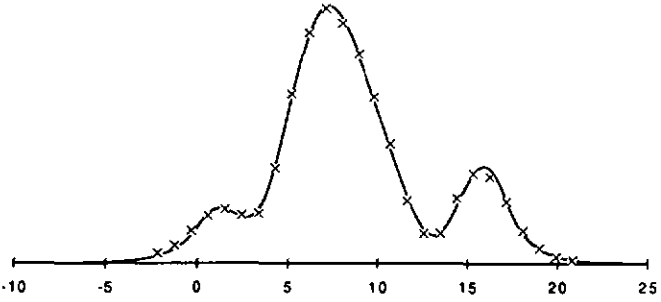

b)

Fig. V.31 Measured (crosses) and calculated (solid line) intensity distribution; input spot position: a) 4 μm, b) 6 μm

It appears from Fig. V.29 that the experimentally retrieved phases, in particular the one of mode 3, lie on a large range. The main reason comes from the injection conditions. As explained in Section IV.2, the actual excitation mode coefficients are not real values if the incidence angle of the Gaussian beam is not normal to the input end-face. Therefore, we conclude that the alignment procedure used in the experiments does not lead to the required accuracy: thus it is not convenient to adjust the angle of the input beam, located at the waveguide centre, until reaching a symmetrical output intensity distribution.

An unexpected effect can be observed in Fig. V.30: the amplitude of the fundamental mode increases when the input spot approaches the waveguide side. Namely, the amplitude of mode 0 is higher with the input spot located at the position x_i=16 µm than at x_i=14 µm. This effect is attributed to the convergence of the MCR algorithm to a local minimum, confirming the observations made in paragraph V.1.2 with the help of simulated intensity distributions.

V.2.3. Discussion of results

These experiments evidence the difficulties encountered with the ONIDA algorithm. In the present section, we review each of them and propose some solutions.

Influence of injection conditions

Calculations carried out in Section IV.I showed the effect of the input beam incidence angle on the excitation mode coefficients of a multimode waveguide. This effect was confirmed by the experiments. By contrast, directional couplers present no visible dependence of the output intensity distribution on the beam incidence angle. Therefore, the present method is well adapted for the characterization of this type of devices. So, the above discussion only concerns multimode waveguides.

As shown in Section IV.1, a focused Gaussian beam leads to complex excitation mode coefficients when the incidence is not normal to the waveguide input face, while real coefficients are assumed in the calculation of the propagation phase differences. In the experiments, we tried to obtain real excitation coefficients by adjusting the incidence angle of the Gaussian beam, as described in paragraph V.2.1. Unfortunately, the results obtained

with multimode waveguides show that the required accuracy is not achieved by the used alignment scheme.

Some improvement can be brought in two ways for the multimode waveguide characterization. First, one can note that narrower Gaussian beams lead to excitation coefficients closer to 0 or π (see Section IV.1). Experimentally, this can be achieved by using an expanded laser beam focused on the waveguide input face, so that the diffraction limit is reached. However, preliminary experiments, carried out with a 5 mm wide 670 nm semiconductor laser beam, did not show significant improvement. Therefore, the most promising way to obtain well controlled injection conditions is to use a single-mode waveguide integrated together with the multimode section, as sketched in Fig. V.34.

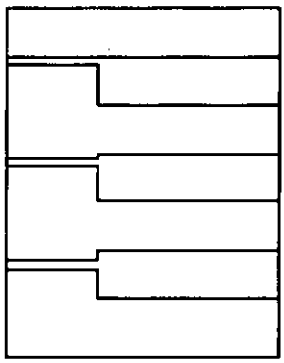

Fig. V.34 Multimode waveguides, integrated together with single-mode waveguides, providing a well-controlled input light source

Calculated and actual eigenfields

The second problem encountered in the present work concerns the effective index and the step-index profile assumed for computing the eigenfields of the three-dimensional ion-exchanged waveguides. Because of the discrepancy between the hypotheses and the actual structures, the computed eigenfields are slightly different from the actual ones, leading to errors of the retrieved mode coefficients. In order to maintain these errors to an acceptable level, a fairly good matching has to be guaranteed between the calculated and experimental eigenfields, as shown from simulated intensity distributions. For that reason, we optimized the most critical

parameters, i.e. waveguide indices, waveguide widths and alignment between the calculation and the experimental coordinate systems, in such a way that the squared error sum $f^n(\mathbf{A})$ is as small as possible (see paragraph V.1.6). Thanks to this procedure, we managed to retrieve meaningful mode coefficients for the three-branch coupler. However, more complicated structures, such as the four-branch coupler studied in paragraph V.2.2, present too many variables for applying efficiently the parameter optimization.

The matching of the actual eigenfields and of the ones used in the ONIDA algorithm can be improved in two ways for ion-exchanged waveguides. First, the effective index and the step-index assumptions can be both removed. Consequently, the three-dimensional structures must be computed numerically, typically using a finite element method [32]. However, such numerical methods need a great amount of computation. This results in the requirement of more powerful PC computers and in longer analysis time. Before going to this extreme, it would be worth keeping the effective index hypothesis and approximate the gradient profile by a multilayer structure, such as described in paragraph II.3.1. A significant improvement can be expected, specially for the directional couplers: because they present two gradient profiles for each branch, they are more sensitive to the step-index assumption than the multimode waveguides. This is confirmed by the optimization of the optogeometrical parameters with the ONIDA method, which led to a refractive index of 1.5163 for the waveguides of directional couplers, whereas we observed an index of 1.5168 for the multimode waveguides. These values can be compared to the equivalent refractive index computed from the effective index method: n=1.5169.

The second possibility for improving the eigenfield precision is of course to measure the actual eigenfields. For this purpose, only a single eigenmode must be transmitted to the waveguide output. This can be achieved by realizing a waveguide Fabry-Perot resonator, through which a given eigenmode is transmitted only if it fulfils a resonance condition. However, a high finesse is required for a good selectivity, in particular when the modes have close propagation constants and propagate over short distances, typical cases of integrated optic structures. This finesse can hardly be achieved in our lossy ion-exchanged waveguides.

Local minima

It was mentioned in paragraph V.1.2 that the MCR algorithm does not converge to local minima when simulated intensity distributions of directional couplers are used. For the experimental three-branch coupler, the meaningful results of paragraph V.2.2 show that the MCR algorithm retrieved the solutions, not local minima. We draw the same conclusion for the four-branch coupler, i.e. no local minima are retrieved. Therefore, we conclude that the local minima do not perturb the MCR algorithm in the case of directional couplers.

However, Section V.1.2 also showed that a local minimum close to the solution can be retrieved by the MCR algorithm in the case of multimode waveguides. Consequently, a criterion was proposed for distinguishing the solution from the local minimum. Namely, the idea was to correlate the amplitudes of the retrieved coefficient vectors with the amplitudes of the initial vector, supposed to be closed to the solution. Because of uncertain results obtained in the case of multimode waveguides, applying the procedure proposed for distinguishing the solution from a local minimum would not be significant. Therefore, this test was not implemented. We can nevertheless conclude that the selection criterion given in paragraph V.1.2 requires a minimum accuracy for an appropriate use, which is not provided in the case of ion-exchanged multimode waveguides.

Experimental conditions

For the four-branch coupler, the propagation length was chosen in such a way that the phase differences of all guided modes are smaller than 2π (condition IV.79). The advantage we expected from this choice is that no correction for periodicity is necessary. Furthermore, the convergence to the complex conjugate of the solution can be easily detected. However, the dispersion of the retrieved phases is quite high in this case, so that the significance of this measurement is not demonstrated. Therefore, we conclude that a mode 1 phase difference lying in the range 0 to π is more convenient experimentally. This corresponds to condition (IV.84) of paragraph IV.4.2. We expect from this condition a choice of corrections almost as easy as with the more restrictive condition (IV.79), but with more significant phase differences.

CHAPTER VI

CONCLUSION

The method proposed in this work analyses the intensity distribution observed at a waveguide output in order to determine the intermodal dispersion of integrated optic waveguide structures. This is achieved by choosing appropriate injection conditions, leading to known excitation mode coefficients (Section IV.2), and by computing the complex mode coefficients from the measured output intensity distribution (Section IV.4). Our goal in this first investigation of the proposed method was to demonstrate the possibility to measure the intermodal dispersion of complex waveguide structures, using simple mathematical models. To this aim, we have chosen the scalar wave equation for describing the modal propagation in the ion-exchanged waveguides used in experiments, and calculated the eigenfields of the structures, using the Effective Index Method and a step-index approximation in the lateral dimension. This approach also means that we have neglected the propagation loss in our study.

The effectiveness of this Ouput Near-field Intensity Distribution Analysis (ONIDA) method was first demonstrated using simulated intensity distributions of three typical waveguiding structures. The accuracy of this method was also studied by taking small variations of the opto-geometrical parameters of the waveguide structures into account. From this study, the range of variation in waveguide parameters leading to a reasonable accuracy of the proposed method was established. For a 10° maximum error in the calculation of optical phase differences, the required accuracies in the waveguide parameters are 0.2 μm for the width and 10^{-4} for the refractive index. The input beam must be coupled in with an angular precision of 0.5° with respect to the axis of normal incidence, while the intensity must be measured within 2%. Computationally, the origins of the theoretical intensity distribution on the one hand, and of the experimental curve on the other hand, must be made to match within 0.1 μm along the substrate surface. This apparent restriction is well resolved by the the

alignment procedure provided by the proposed Mode Coefficient Retrieving (MCR) algorithm. From the foregoing it is possible to state that the ONIDA method is viable and offers a potential tool for characterizing the propagation properties of few-mode waveguiding structures.

The experimental demonstration was carried out using ion-exchanged waveguides, single-mode in depth. In this type of structures, the measurements made with a strongly coupled three-branch coupler, consisting of three single-mode waveguides, provided meaningful results: the Mode Coefficient Retrieving (MCR) algorithm reached a repeatability of better than ±15° for the mode coefficient phase differences. This led to a 10^{-5} resolution of the effective index differences in the case of a 4.58 mm long waveguide used at 633 nm wavelength. In the case of this three-branch coupler, the correction of 0 or π for the injection conditions was applied without ambiguity; the algorithm never diverged to the complex conjugate of the solution. The ONIDA method, however, is not appropriate for characterizing weakly coupled waveguides, nor asymmetric couplers. These results were expected from theoretical considerations. In the case of a four-branch coupler, made up of strictly single-mode waveguides, the ONIDA algorithm did not retrieve relevant mode coefficients. This is attributed to the applicability of the effective index and the step index assumptions for this type of ion-exchanged waveguide structure. For a four-mode waveguide, single section in width, we met increased difficulties in controlling the injection conditions, and did not obtain successful measurements of the intermodal dispersion.

This first investigation of the ONIDA method pointed out some difficulties linked to this technique: (i) the applicability of the Effective Index Method and the step-index approximation for ion-exchange waveguides; (ii) the increased difficulty in controlling the injection conditions as the cross-section of the waveguide becomes larger; (iii) the increase of the number of local minima as the number of modes in the structure increases. To tackle each of the above difficulties, the following solutions are proposed.

The effective index and the step index assumptions, as applied here for ion-exchanged waveguides in glass, lead to a mismatch between the computed and actual eigenfields, inducing an error of the retrieved mode coefficients. Since the ONIDA method successfully charaterized three-branch couplers using the above assumptions, it is believed that significant

improvement can be obtained, by keeping the effective index assumption and approximating the lateral index profile by a multilayer structure, made of a series of thin layers, each with a constant refractive index. In such a structure, the eigenfields can be easily computed by the Transfer Matrix Method. With this new approach, some improvement of the ONIDA algorithm is expected, in particular when it is applied to the ion-exchanged four-branch coupler used in this work. This improvement also concerns other types of waveguides, such as titanium diffused lithium niobate waveguides, whose index profiles are known to be graded.

The deleterious effects of the above assumptions are, however, very small in the case of waveguides exhibiting a step-index profile, commonly obtained by layer deposition techniques. Typical examples are semiconductor waveguides, which are of great interest in the development of opto-electronic devices [50,51]. In these cases, we expect the ONIDA method to provide a useful tool for the design of guided-wave devices, such as directional couplers, star couplers and multimode interference sections (MMI).

As shown in paragraph V.2.3, the **injection conditions** must insure that the mode coefficients at the waveguide input are purely real. Experimental results showed that this condition was closely reached with directional couplers, but not with lightly multimode waveguides. In this latter case, a method for aligning the incident beam onto the waveguide input face was proposed and tested. The experiments indicated that this procedure does not provide the necessary accuracy. In order to improve the results obtained by the ONIDA method for multimode waveguide sections, it is proposed to fabricate a waveguide structure integrating a single-mode waveguide, butt-coupled to the input of the multimode sections to be analysed. This arrangement will provide well defined and stable injection conditions. The drawback is that scanning the input light source is no longer possible. However, this problem can be overcome by integrating several similar multimode sections, each with a different position with reference to the input single-mode waveguide.

The last problem of the ONIDA algorithm is the **presence of local minima** in the function to be optimized. To overcome this problem, it is proposed, first, to properly choose the initial coefficient vector used at the beginning of the iteration process, and, second, to begin the iteration by optimizing

the phases only in the ONIDA algorithm. With these conditions, we showed that the algorithm converges safely to the solution when analysing directional couplers, and excludes all local minima in multimode waveguide sections, except one, close to the solution. Therefore, retrieving a local minimum cannot be totally excluded when analysing multimode waveguide sections. For this reason, a method for distinguishing the solution from a local minima is proposed. The method is based on the correlation product of the amplitudes of the retrieved mode coefficients with the amplitudes of the calculated excitation coefficients.

The design of useful devices, which makes use of the multimode interference (MMI) principle in large waveguide sections, to realize optical phase demodulators [21, 43] or power splitters [51], requires an accurate knowledge of the propagation properties of actual waveguide sections. The need of a method providing this information has been furthered by the recent regain of interest for MMI structures [50, 51], since they were first reported in 1975 [20]. For this particular type of integrated optic devices, the analysis by the ONIDA algorithm offers two further advantages: (i) it analyses the conditions that give rise to the manifold image formation in MMI sections, i.e. the interferences of eigenmodes; (ii) its implementation does not require special preparation of the samples to be studied. Furthermore, it is fast and simple to use, and only requires standard laboratory apparatus.

Although not all experimental results carried out in ion-exchanged waveguide structures are fully conclusive, it is expected that the proposed improvements in the ONIDA method will render this technique an interesting candidate for characterizing modal propagation in few-mode waveguides. This is, for instance, the case of optical waveguides made by layer deposition, such as silica-on-silicon structures. However, it is believed that improving the ONIDA method will also allow to determine the intermodal dispersion of graded-index waveguides, carrying up to 6 or 8 modes. In particular, this new technique should be able to satisfy our initial motivation in this work, namely, to explain the unexpected behavior of our optical phase demodulator, based on the fourfold image formation, where the observed power phase shifts appeared in a wrong sequence.

A.1 Calculating the gradient of the squared error sum

The squared error sum is given by (IV.21):

$$f(\mathbf{A}) = \sum_{k=0}^{M} \left\{ S_k - S(y_k, \mathbf{A}) \right\}^2 \tag{A1.1}$$

The partial derivative of $f(\mathbf{A})$ with respect to the phase φ_p is given by:

$$\frac{\partial f}{\partial \varphi_p} = -2 \sum_{k=0}^{M} \left\{ S_k - S(y_k, \mathbf{A}) \right\} \frac{\partial S(y_k, \mathbf{A})}{\partial \varphi_p} \tag{A1.2}$$

where

$$\frac{\partial S(y_k, \mathbf{A})}{\partial \varphi_p} = \frac{\partial}{\partial \varphi_p} \left\{ -(EH^* + E^*H) \right\} \tag{A1.3}$$

With $E = \sum_{i=0}^{N} \mathbf{A}_i E_i$ and $H = \sum_{i=0}^{N} \mathbf{A}_i H_i$, one gets:

$$\frac{\partial S(y_k, \mathbf{A})}{\partial \varphi_p} = -j \left[\mathbf{A}_p (E_p H^* - H_p E^*) - \mathbf{A}_p^* (H_p E + E_p H) \right] \tag{A1.4}$$

where we chose the eigenmodes E_i and H_i real.

Similarly, we have for the partial derivative of f(**A**) with respect to the amplitude a_p :

$$\frac{\partial f}{\partial a_p} = -2\sum_{k=0}^{M}\left\{S_k - S(y_k, \mathbf{A})\right\}\frac{\partial S(y_k, \mathbf{A})}{\partial a_p} \qquad \text{(A1.5)}$$

and

$$\frac{\partial S(y_k, \mathbf{A})}{\partial a_p} = -\left[\frac{A_p}{|A_p|}(E_p H^* - H_p E^*) + \frac{A_p^*}{|A_p|}(H_p E + E_p H)\right] \qquad \text{(A1.6)}$$

A.2 Implementation of the BFGS algorithm in this work

In paragraph IV.3.3., we stated that the optimization has to be performed first with the phases, keeping the amplitudes constant. This can be merely achieved by a proper choice of the initial matrix $\mathbf{H}^{(0)}$. Assume the component Φ_m of the parameter vector $\Phi^T = (\varphi_1 \cdots \varphi_N \,|\, a_0 \cdots a_N)$ must be kept constant. We have to prove that $\Phi_m^{(k)}$ is kept constant at each iteration k, i.e. $\Phi_i^{(k+1)} = \Phi_i^{(k)}$ $\forall k$, when the mth row of the initial matrix $\mathbf{H}^{(0)}$ is made of zeros: $H_{mi}^{(0)} = 0$ $\forall i = 0, 1, \ldots, 2N$.

Suppose we have $H_{im}^{(k)} = 0$, for any k. This is true by choice for k=0. Then, equation (IV.49) implies that, for any $\mathbf{g}^{(k)}$:

$$s_m^{(k)} = -\sum_{i=0}^{N} H_{mi}^{(k)} g_i^{(k)} = 0 \qquad \text{(A.2.1)}$$

Thus we deduce easily from (IV.52) and (A.2.1):

$$\Phi_m^{(k+1)} = \Phi_m^{(k)} \qquad \text{(A.2.2)}$$

We must prove now that (A.2.2) also holds for the next iteration step. This is achieved if the updated matrix $\mathbf{H}^{(k+1)}$ also shows the property: $H_{mi}^{(k+1)} = 0$ $\forall i = 0, 1, \ldots, 2N$. So, let us examine the

update $\mathbf{H}^{(k+1)}$ term by term. The first term in the rigth side of (IV.51) is, by supposition:

$$H_{mi}^{(k)} = 0 \tag{A.2.3}$$

The second term gives:

$$\left(\delta\delta^T\right)_{mi} = \delta_m\delta_i = 0 \;\forall i = 0, 1, \ldots, 2N \tag{A.2.4}$$

The third term have the contribution:

$$\left(\delta\gamma^T\mathbf{H} + \mathbf{H}\gamma\delta^T\right)_{mi} = \delta_m \sum_{j=0}^{N} H_{ji}\,\gamma_j + \delta_i \sum_{j=0}^{N} H_{mj}\,\gamma_j = 0 \tag{A.2.5}$$

So the update $\mathbf{H}^{(k+1)}$ also exhibits the property:

$$H_{mi}^{(k+1)} = 0 \;\forall i = 0, 1, \ldots, 2N. \tag{A.2.6}$$

Using (IV.52) and (A.2.1) again, we have: $\Phi_m^{(k+2)} = \Phi_m^{(k+1)} = \Phi_m^{(k)}$, which demonstrates that:

$$\Phi_m^{(k+1)} = \Phi_m^{(k)} \;\forall k \tag{A.2.7}$$

REFERENCES

[1] H. Osterberg and L.W. Smith, "Transmission of optical energy along surfaces: Parts I and II", *J. Opt. Soc. Amer.*, Vol. 54, 1964, pp. 1073-1084

[2] S.E. Miller, "Integrated Optics: An introduction", *Bell Syst. Tech. J.*, Vol. 48, 1969, pp. 2059-2069

[3] H. Nishihara, M. Haruna, and T. Suhara, *Optical integrated circuits*, MacGraw-Hill, New-York, 1989

[4] E.R. Schineller, R.P. Flam, and D.W. Wilmot, "Optical waveguides formed by proton irradiation of fused silica", *J. Opt. Soc. Amer.*, Vol. 58, 1968, pp. 1073-1084

[5] I.P. Kaminov, J.R. Carruthers, E.H. Turner, and L.W. Stulz, "Thin-film $LiNbO_3$ electro-optic light modulator", *Appl. Phys. Lett.*, Vol. 22, 1973, pp. 540-542

[6] W.L. Bond, B.G. Cohen, R.C.C. Leite, and A. Yariv, "Observation of the dielectric-waveguide mode of light propagation in p-n junctions", *Appl. Phys. Lett.*, Vol. 2, 1963, p. 57-59

[7] J.W. Burgess, P.J. Williams, P.M. Charles, A.J. Moseley, J.P. Hall, G. Phillpott, and A. Markatos, "OIECs for Local Access Applications", Procs 6th Eur. Conf. on Integrated Optics, ECIO'93, Neuchâtel, Switzerland, April 18-22, 1993, pp. 2-8 - 2-9

[8] I.P. Kaminov, H.P. Weber, and E.A Chandross, "A poly-(methyl methacrylate) dye laser with international diffraction grating resonator", *Appl. Phys. Lett.*, Vol. 18, 1971, pp. 497-499

[9] A. Beguin, T. Dumas, N. Nissim, and R. Jansen, "Fabrication and performance of low-loss optical components made by ion exchange in glass", Procs OFC'88, 1988, paper THJ5

[10] E.A.J. Marcatili, "Optical subpicosecond gate", *Appl. Opt.*, Vol. 19, 1980, pp. 1468-1476

[11] G.H.B. Thompson, *Physics of semiconductor laser devices*, John Wiley & Sons, Chichester, 1980

[12] H. Heidrich, "Progress and prospects towards coherent receiver frontend OIECs - Issues, challenges an perspectives", Procs. 6th Eur. Conf. on Integrated Optics, ECIO'93, Neuchâtel, Switzerland, April 18-22, 1993, pp. 2-17 - 2-19

[13] C.S. Tsai, "Guided-wave acoustooptic Bragg modulators for wide-band integrated-optic communications and signal processing", *IEEE Trans. Circuits Syst.*, Vol. CAS-26, 1979, pp. 1072-1098

[14] F.J. Leonberger, C.E. Woodward, and R.A. Becker, "4-bit 828-megasample/s electro-optic guided-wave analog-to-digital converter", *Appl. Phys. Lett.*, Vol. 40, 1982, pp. 565-568

[15] T. Suhara, S. Ura, H. Nishihara, and J. Koyama, "An integrated-optic disk pickup device", Procs. Int. Conf. Integrated Opt. and Opt. Fiber Commun., Venezia, Italy, Oct. 1-4, 1985, pp. 117-120

[16] C. Wulf-Mathies, "Integrierte Optik für Faseroptische Sensoren", *Laser und Optoelektronik*, Vol. 21, 1989, pp. 57-63

[17] G. Voirin, L. Falco, O. Boillat, O. Zogmal, P. Regnault, and O. Parriaux, "Monolithic double interferometer displacement sensor with wavelength stabilization", Procs. 6th Eur. Conf. on Integrated Optics, ECIO'93, Neuchâtel, Switzerland, April 18-22, 1993, pp. 12-28 - 12-29

[18] Y. Okamura, S. Yoshinaka, and S. Yamamoto, "Measuring mode propagation losses of integrated optical waveguides: a simple method", *Appl. Opt.*, Vol. 22, 1983, pp. 3892-3894

[19] D. Jestel and E. Voges, "Refracted Near-Field characterization of ion exchanged glass waveguides and device simulation", Procs. 5th Eur. Conf. on Integrated Optics, ECIO'89, Paris, April 26-28, 1989, SPIE Vol. 1141, pp. 185-190

[20] R. Ulrich, "Image formation by phase coincidences in optical waveguides", *Opt. Commun.*, Vol, 13, 1975, pp. 259-264

[21] Th. Niemeyer and R. Ulrich, "Quadrature outputs from fiber interferometer with 4x4 coupler", *Opt. Lett.*, Vol. 11, 1986, pp. 677-679

[22] P. Roth, "Passive integrated optic mixer providing quadrature outputs", Procs. 5th Eur. Conf. on Integrated Optics, ECIO'89, April 26-28, 1989, Paris, SPIE Vol. 1141, pp. 169-173

[23] P.K. Tien, R. Ulrich, and R.J. Martin, "Modes of propagating light waves in thin deposited semiconductor films", *Appl. Phys. Lett.*, Vol. 14, 1969, pp. 291-294

[24] W.S.C. Chang, "Periodic structures and their application in integrated optics", *IEEE Trans. Microwave Theory and Techn.*, Vol. MTT-21, 1973, pp. 775-785

[25] F. Maystre, *Optical fiber sensors using birefringent resonators*, PhD thesis, University of Neuchâtel, Switzerland, 1990

[26] R. Eckhardt and R. Ulrich, "Mode-beating spectroscopy in few-mode optical guide", *Appl. Phys. Lett.*, Vol. 63, 1993, pp. 284-286

[27] A.W. Snyder and J.D. Love, *Optical Waveguide Theory*, Chapman and Hall, London, 1983

[28] H. Kogelnik, Theory of Optical Waveguides, in *Guided-Wave Optoelectronics*, T. Tamir Ed., Springer Verlag, Berlin, 1988

[29] C. Pask, "On the neglect of refracting rays in optical power calculations", *Opt. Quant. Elect.*, Vol. 7, 1975, pp. 428-429

[30] B. Jonsson and S.T. Eng, "Solving the Schrödinger equation in arbitrary quantum-well potential profiles using the Transfer Matrix Method", *IEEE J Quant. Electron.*, Vol. 26, 1990, pp. 2025-2035

[31] E.A.J. Marcatili, "Dielectric rectangular waveguide and directional coupler for integrated optics", *Bell Syst. Tech. J.*, Vol. 48, 1969, pp. 2071-2102

[32] G.W. Slade and K.J. Webb, "A vectorial Finite Element analysis for integrated waveguide", *IEEE Trans. Magn.*, Vol. 25, 1989, pp. 3052-3054

[33] R.M. Knox and P.P. Toulios, "Integrated circuits for the millimeter through optical frequency range", Procs. MRI Symp. Submillimeter Waves, Polytechnic Press, Brooklyn, 1970, pp. 497-516

[34] G.B. Hocker and W.K. Burns, "Mode dispersion in diffused channel waveguides by the effective index method", *Appl. Opt.*, Vol. 16, 1977, pp. 113-118

[35] J. Albert, "Ion Exchange from Salt Melts", in *Introduction to Glass Integrated Optics*, S.I. Najafi Ed., Artech House, Norwood, 1992

[36] T. Izawa and H. Nakagome, "Optical waveguide formed by electrically induced migration of ions in glass plates", *Appl. Phys. Lett.*, Vol. 21, 1972, pp. 584-586

[37] V. Neuman, O. Parriaux, and L.M. Walpita, "Double-alcali effect: influence on index profile of ion-exchanged waveguides", *Electron. Lett.*, Vol. 15, 1979, pp. 704-706

[38] G.H. Chartier, P. Jaussaud, A.D. de Oliveira, and O. Parriaux, "Optical waveguides fabricated by electric-field controlled ion-exchange in glass", *Electron. Lett.*, Vol. 14, 1978, pp. 132-143

[39] J.E. Gortych and D.G. Hall, "Fabrication of planar optical waveguides by K^+-ion exchange in BK7 and Pyrex glass", *IEEE J. Quantum Electron.*, Vol. QE-22, 1986, pp. 892-895

[40] A. Brandenburg, "Stress in ion-exchanged glass waveguides", *J. Lightwave Technol.*, Vol. LT-4, 1986, pp. 1580-1593

[41] C. Visconti, *Etude de la biréfringence dans des guides optiques fabriqués par échange d'ions sur substrat de verre: séparateur de polarisation*, PhD thesis, Institut National Polytechnique de Grenoble, 1990

[42] Y. Okamura, S. Sato, and S. Yamamoto, "Simple method of measuring propagation properties of integrated optical waveguides: an improvement", *Appl. Opt.*, Vol. 24, 1985, pp. 57-60

[43] P. Roth and G. Voirin, "Integrated optic mixer for interferometric applications", Procs. Int. Congress on Optical Science & Engineering, September 19-23, Hamburg, SPIE Vol. 1014, 1988

[44] P. Roth and O. Parriaux, "Integrated interferometer with phase diversity", Technical Digest IOOC'89, July 18-21, Kobe, Japan, 1989, pp. 120-121

[45] R. Cairoli, *Algèbre linéaire*, Presses polytechniques et universitaires romandes, Lausanne, 1991

[46] W.K. Burns and A.F. Milton, "3x2 channel waveguide gyroscope couplers: Theory", *IEEE J. Quant. Electron.*, Vol. QE-18, 1982, pp. 1790-1796

[47] A. Angot, *Compléments de Mathématiques à l'usage des ingénieurs de l'électrotechnique et des télécommunications*, Masson, Paris, 1982

[48] R. Fletcher, *Practical methods of Optimization, Vol. 1: Unconstrained optimization*, John Wiley & Sons Ltd, London, 1980

[49] P. Roth, "Amplitudes and relative phases calculated from the output intensity distribution in a waveguiding structure", Procs 6th Eur. Conf. on Integrated Optics, ECIO'93, Neuchâtel, April 18-22, 1993, pp. 14-38 - 14-39

[50] M.K. Smit, *Integrated optics in silicon-based aluminium oxide*, Ph.D. thesis, ISBN 90-9004261-X, Delft University of technology, Delft, the Netherlands, 1991

[51] L.B. Soldano, M. Bachmann, P.-A. Besse, M.K. Smit, and H. Melchior, "Large optical bandwidth of InGaAsP/InP multi-mode interference 3 dB couplers", Procs 6th Eur. Conf. on Integrated Optics, ECIO'93, April 18-22, Neuchâtel, Switzerland, 1993, pp. 14-10 - 14-11